Reduced temperature crystallization of bismuth substituted iron garnet films using oxygen plasma annealing

Rohit Sharda

THE UNIVERSITY OF
WESTERN AUSTRALIA

This thesis is presented for the degree of Master of Engineering science (Research)
at The University of Western Australia

Microelectronics Research Group

School of Electrical, Electronic and Computer Engineering

September 2013

Professor John Dell, Dean

Faculty of Engineering, Computing, and Mathematics

The University of Western Australia

35 Stirling Highway

Nedlands, WA, 6009

Dear Professor John Dell,

It is with great satisfaction that I present this thesis in fulfilment for the degree of Master of Engineering Science (Research), entitled

Reduced temperature crystallization of bismuth substituted iron garnet films using oxygen plasma annealing.

This work was performed under the guidance of Professor Mariusz Martyniuk, Professor Lorenzo Faraone, Professor John Dell, within the School of Electrical, Electronic and Computer Engineering; and Professor Robert Woodward within School of Physics; and Dr. Roger Jeffery from Panorama Synergy Limited.

Yours Sincerely

Rohit Sharda

Abstract

In this thesis, we are attempting to reduce the thermal budget required to crystallize garnet films ($Bi_2Dy_1Fe_4Ga_1O_{12}$) by using plasma annealing. in order to make this material more compatible with industrial CMOS processing. We have optimized the plasma parameters to obtain the optimal crystallization conditions and optimal magneto-optical characteristics. In addition, the effects of plasma annealing on crystallization and magneto-optical parameters are examined by comparing the plasma annealed garnet samples with traditional rapid thermal and oven annealed garnet samples.

The thermal budget required to crystallize $Bi_2Dy_1Fe_4Ga_1O_{12}$ thin films have successfully been reduced to a temperature as low as 515 °C by exposing the films to radio frequency (13.56 MHz) oxygen plasma. The crystallization was achieved at temperature more than 100 °C below the temperatures required for the crystallization via conventional rapid thermal and oven annealing.

A conductor (gold foil) attached in thermal contact with the backside of the sample was found to increase the sample temperature and improve garnet crystallization. Optical emission spectroscopy confirmed the presence of substantial quantities of both atomic oxygen (O) and singly ionised atomic oxygen (O^+) under the process conditions (rf power: 500-800 Watts, pressure 2-5 Torr) used to achieve crystallization. It was found that the sample temperature was linearly dependent upon the summation of the logs of the magnitude of emission lines of both O^+ and O within the plasma, suggesting that heating of the sample was related to free energy of reactions involving these species.

Acknowledgements

Foremost, I have to thank, above all others, my parents for their wisdom and guidance. I am grateful for the endless love and support that you have provided over the years. There are not too many occasions when someone gets to publicly thank their parents and siblings, and in a way, this is one of those occasions.

I would like to thank the Microelectronics Research Group (MRG), headed by Prof. Lorenzo Faraone, for the opportunity to work on this interesting and rewarding project.

I would like to express my sincere gratitude to Dr. Roger Jeffery, Prof. Mariusz Martyniuk and Prof. Robert Woodward for their continuous support during my Master's study and research, for their patience, motivation, and immense knowledge. They deserve great thanks for their guidance, suggestions and feedback throughout my candidature, and especially during the traditionally harrowing writing-up process. All of you have spent much of your own time reviewing the many iterations of this document to allow its completion within my tight schedule, and I thank you all especially for that.

I would also like to extend my thanks to Sabine Betts, secretary of MRG, for making sure that everything run smoothly in MRG. I am indebted to the other members of the laboratory in CMCA especially Prof. Martin Saunders and David Adams who have taken time to teach me various experimental methods and helped me collect data. Of course, I cannot forget all the wonderful friends I have made in past two years. I have enjoyed working with you all, and I look forward to keeping in touch with you all both professionally and as friends.

Thank you, Lord, for always being there for me.

Thank you everyone for the lessons and memories!!!!

Rohit Sharda

Contents

Abstract i

Acknowledgements iii

Contents v

Introduction 1

1.1 CMOS integration 1

1.2 Plasma annealing – annealing with a reduced thermal budget 4

1.3 Thesis objective 9

1.4 Thesis organization 10

Plasma physics and heating mechanisms 13

2.1 General background 14

2.2 Ionization and recombination reactions in O_2 plasma 16

2.3 Physical description of a capacitively coupled plasma 18

2.4 Thickness of sheath 22

2.5 Local and non-local electron heating 26

2.6 Electron energy distribution function 28

2.7 Summary 31

Material and characterization methods 33

3.1 Bismuth dysprosium gallium iron oxide 34

3.1.1 Garnet sample description 36

3.2 Plasma barrel asher 36

3.3 Thermal imaging 38

3.3.1 Calibration of thermal imager 42

3.3.2 Test sample calibration 43

3.4 Optical emission spectroscopy 45

3.4.1 OES experimental configuration 46

3.5 Langmuir probes 47

3.5.1 Langmuir probe experimental configuration 48

3.6 Post-deposition heat treatment 50

3.7 X-ray diffraction 50

3.8 Faraday rotation and optical transmission 52

3.8.1 Set-up for magneto-optical measurements 53

3.9 Atomic force microscopy 54

3.10 Transmission electron microscopy 55

3.11 Electron probe micro analysis 57

3.12 X-ray photoelectron spectroscopy 59

3.13 Summary 59

Plasma characterization 61

4.1 Sample temperature characterization 62

4.1.1 Test sample temperature variations 62

4.1.2 Effects of conductor on thermal variations 65

4.1.3 Temperature dependence on conductor geometry 67

4.1.4 Temperature variations due to different conductors ... 72

4.2 Optical emission characterization ... 73

4.2.1 Variations in atomic oxygen emission line ... 76

4.2.2 Variations in singly ionised atomic oxygen emission line ... 77

4.2.3 Langmuir probe measurements ... 78

4.2.4 Comparison of O^+ and O emissions (with and without gold) ... 79

4.2.5 Sample temperature as a function of emission magnitudes of O^+ and O ... 80

4.3 Ionization and diffusion as a function of rf power and pressure ... 81

4.4 Sample heating mechanisms ... 85

4.5 Effects of conductor on optical emissions and sample temperature. ... 86

4.5.1 Inductive heating and skin effects ... 88

4.6 Reactions involved in the oxygen plasma ... 91

4.7 Sample temperature as a function of reaction quotient ... 94

4.8 Summary ... 96

Material characterization ... 99

5.1 Characterization of $(BiDy)_3(FeGa)_5O_{12}$ films ... 100

5.1.1 Crystallinity (X-ray diffraction) ... 103

5.1.2 Faraday rotation and optical transmission ... 104

5.1.3 Surface and Microstructure analysis ... 110

5.1.3.1 Atomic force microscopy ... 110

5.1.3.2 Transmission electron microscopy ... 113

5.1.4 Compositional analysis ... 115

5.1.4.1 Electron probe micro analysis ... 115

5.1.4.2 X-ray photoelectron spectroscopy ... 116

5.2 Discussion 120

5.2.1 Plasma Annealing 120

5.2.2 Comparison of plasma annealing with other techniques 121

5.2.3 Effects on magneto-optical properties 122

5.2.4 Surface effects 123

5.2.5 Effects on composition 124

5.3 Summary 125

Conclusions and further work 127

6.1 Summary 128

6.2 Conclusions 131

6.3 Further work 133

Appendix I 137

Appendix II 139

Bibliography 143

In an instant, illumination can be achieved. It is as easy as turning on a light; the problem is finding the switch in the dark.

1 Introduction

In recent years, significant improvements have been achieved in the area of thin film materials synthesis for various emerging optical applications and technologies. Rare-earth garnet materials are very promising materials for optical applications due to their magneto-optical properties. Different types of materials containing rare-earth atoms have been investigated in detail and are used for various applications.

Bi-substituted rare-earth iron garnet materials have excellent magneto-optical properties that can potentially have a wide range of applications in recording and imaging [1, 2], ultrafast switching [3], magnetic-field sensing [4, 5], and optical modulation in the visible spectrum for displays [6, 7]. These materials also have prospects in the area of integrated photonics [8] which may find applications in on-chip communications. A description of $Bi_2Dy_1Fe_4Ga_1O_{12}$ material and its properties are presented in Chapter 3 (see Section 3).

1.1 CMOS integration

Although widely used, integration of these magneto-optical garnet materials onto semiconductor-based integrated circuits is restricted because of challenges in both device design and materials integration. On the device side, large footprints of the

devices with length scales from millimeters to centimeters limits the feasibility of large-scale and low-cost integration [9, 10]. On the materials side, there are three ways of integrating the garnets on semiconductor substrates. One option is to deposit garnets epitaxially on the lattice-matched (12 A°) $Gd_3Ga_5O_{12}$ (GGG) substrates followed by epitaxial lift-off and wafer bonding. In the epitaxial lift-off process, the epitaxially grown film is physically separated from the substrate. Following this, the materials are integrated to Si or SOI (silicon on insulator) with the help of wafer bonding. Wafer bonding refers to the technique whereby wafers of almost any material are connected without any kind of adhesives [11].

Since wafer bonding is an expensive fabrication process from a monetary cost standpoint, some attempts have also been made to use a MgO buffer layer between the garnet and the semiconductor substrate more simpler fabrication methods such as metal-organic chemical vapor deposition or reactive radio frequency sputtering [12-14]. However, it was shown that the in-situ crystallization needs to be below 650°C to avoid damage to the semiconductor substrate [15].

The third way is to grow garnets directly on Si or SOI. This would allow the use of the highly refined silicon infrastructure, based on complementary metal oxide semiconductor (CMOS) technology. However, the problem with the direct integration of the garnet material is the high thermal processing required for the crystallization of the garnet materials [16, 17]. The high temperature processing would result in the inter-diffusion of implanted dopant species, thus degrading or destroying the device performance [18].

In this thesis, the aim is to reduce the thermal budget for the crystallization of the $Bi_2Dy_1Fe_4Ga_1O_{12}$ films. The term (thermal budget) defines the total amount of thermal energy transferred to the wafer during processing. The crystallization of a typical iron garnet material of composition $Bi_2Dy_1Fe_4Ga_1O_{12}$ (BiDyGa:IG) on a Si/SOI substrates requires a minimum annealing temperature of 620 °C by rapid thermal annealing [19], or around 650 °C by furnance annealing [20].

At the highest level, the CMOS fabrication process is divided into two halves, the front and back ends. The field effect transistors (FETs), diodes and all other semiconductor devices are fabricated during the front end and metal interconnects are fabricated during the back-end. Since the photonic materials are formed after the metal-interconnect process, it is important that any subsequent processing temperature does not go above a certain critical temperature, as this can potentially affect device performance. Typically, aluminum may be used as a metal for CMOS interconnections. The eutectic point of aluminum and silicon is 577 °C. Therefore, it is an absolute necessity that the processing temperature should not go above 577 °C, as beyond this temperature the aluminum and silicon bond together (eutectic bonding), which would destroy the integrity of the entire chip. Hence, if garnet material is to be incorporated with CMOS technology, it is essential that the garnet crystallization needs to be undertaken at temperatures below 577 °C.

1.2 Plasma annealing – annealing with a reduced thermal budget

To achieve this goal, this thesis investigates a novel annealing method known as plasma annealing, which promises to crystallize the oxide films at temperatures lower than the temperatures required by conventional rapid thermal annealing (RTA) and furnance annealing. Plasma annealing has already been shown to effectively reduce the thermal budget for the crystallization of TiO_2, ITO and Lanthanum oxide (La_2O_3) films [21-26].

In 2008-09, Ohsaki *et al.* [22-26] reported the crystallization of as-deposited amorphous TiO_2 and indium titanium oxide (ITO) films (at a temperature lower than 150 °C) via exposure to a radio-frequency (13.56 MHz) plasma in a barrel-type quartz chamber with a pair of electrodes each covering half of the cylindrical wall. Ohsaki *et al.* [22-26] used a solid state rf power generator (Huettinger Elektronik GmbH + Co. KG, QINTO 3013) to supply 13.56 MHz rf power to the quartz chamber through an auto impedance matcher (RF VII, Inc.). The temperature of the films during the plasma treatment was measured via a radiation thermometer (IT-540 N, Horiba Ltd). This is a dual beam infrared thermometer, which works in the temperature range of -50°C--500°C with a reproducibility of ± 4°C. Using the radiation thermometer, they observed that the sample temperature did not rise above 250 °C (for oxygen plasma) across the experimental range (rf power: 300-1000 Watts, Pressure: 10-10000 Pa [0.07-7.5 Torr]) [25]. The temperature profile observed by Ohsaki is shown in Fig. 1.2.1.

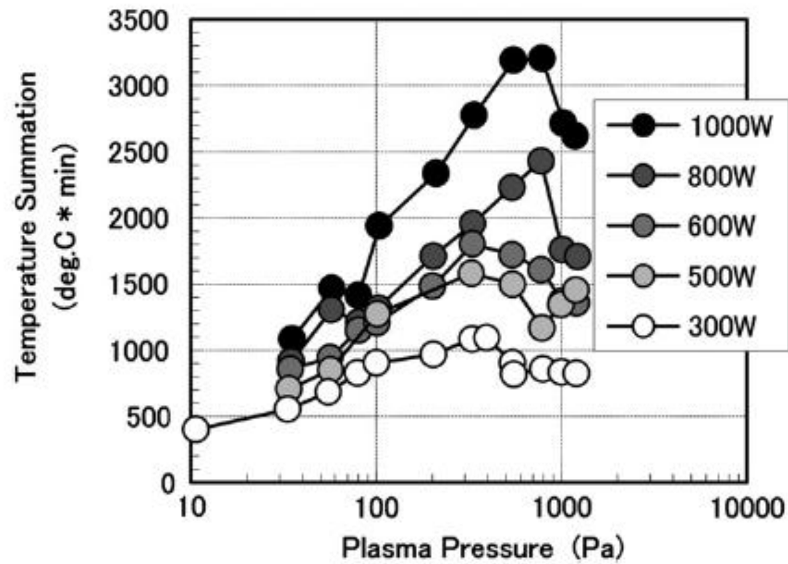

Fig. 1.2.1: Summation of temperature during O_2 plasma treatment for 15 minutes [22].

The TiO_2 and ITO films were exposed to different power and pressure conditions and it was observed that the crystallization process was dependent upon the appropriate gas pressure (see Fig. 1.2.2). The pressure of 330 Pa (2.4 Torr) for O_2 was found to be the most effective pressure to crystallize the ITO films.

It can be observed from the plot that the ITO films are crystallized at some pressures and not at others. In addition, it was observed that an argon based plasma also showed a gas pressure dependence, but with the peak in crystallization shifted to different pressures. However, Ohsaki reports two different optimum pressures for ITO crystallization in Ar plasma, one at ~ 100Pa in [22] and one at 1000Pa in [25].

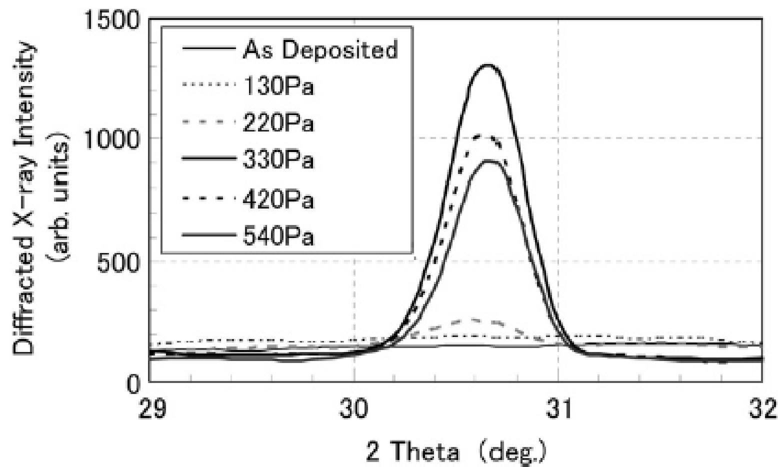

Fig. 1.2.2: XRD profiles of ITO films with O_2 plasma treatment at various pressures [25].

Ohsaki used the results of Monte Carlo simulation (via SRIM program) from Ref. [27] to conclude that under his experimental conditions, the positive Ar, O or O_2 ions should only cause effects at the surface of the films as they cannot penetrate deep into the films. To check this hypothesis, he deposited a film of TiO_2 on the ITO film and the thickness of TiO_2 was kept large enough to protect the ITO from the bombardment of plasma species. The resultant stacked film with a layer construction of 100 nm TiO_2/100 nm ITO/20 nm SiO_2/Glass was treated with O_2 plasma with 330 Pa gas pressure for 10 min whereby the ITO film was crystallized but the TiO_2 was not. Based on these results it was concluded that plasma (via ion bombardment) itself does not crystallize the films.

To understand the low-temperature crystallization process via plasma exposure, he used the concept of ponderomotive force in microwave sintering, which says that under the effect of oscillating electromagnetic fields, ponderomotive force helps in the movement of free ions in the areas where the dielectric constant is changing. Using this concept, he proposed that the plasma acts as a three-dimensional electric circuit with complex dielectric constant, which changes with the applied pressure. Therefore, he

proposed that an appropriate pressure is required to realize the three-dimensional electric circuit to increase the electromagnetic field at the film surface. Based on this hypothesis, he suggested that the rf electromagnetic waves remain the only mechanism for the transporting of energy to the film, so as to overcome the free energy barrier for the change from the amorphous to the crystalline state.

Further, during his experiments, he noticed that the condition window of plasma crystallization of TiO_2 was narrower than that of ITO. He noticed that the sputtered TiO_2 films were relatively difficult to crystallize with simple plasma crystallization. This behavior is very similar to the crystallization process via thermal processing, where the TiO_2 films need higher temperatures (about 500°C [25]) to crystallize in comparison to ITO filma (> 400 °C for air [28]).

Therefore, in order to better crystallize the TiO_2 films and understand the effects of electromagnetic waves on crystallization, he introduced a Cu sheet behind (ungrounded) and in contact with the sputtered TiO_2 films. He observed that the effectiveness of the crystallization was enhanced (see Fig. 1.2.3).

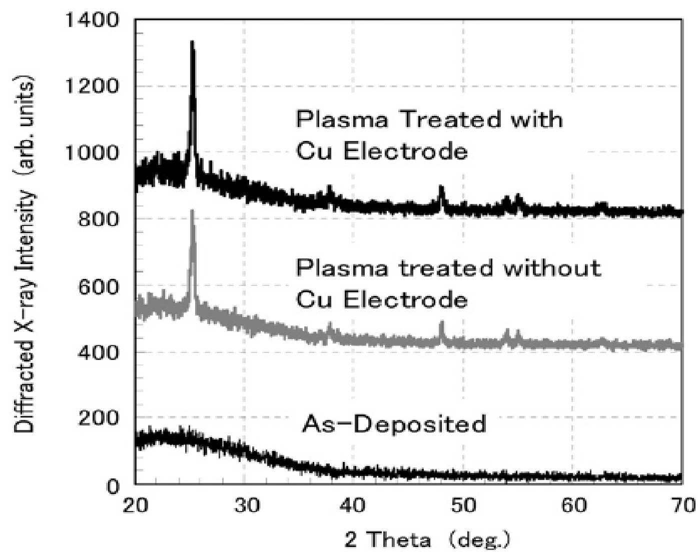

Fig. 1.2.3: XRD profiles of sputtered TiO_2 films at a pressure of 330Pa in O_2 plasma adopting and not adopting Cu at backside along with as-deposited TiO_2 sample [25].

The reason for the increase in the effectiveness of crystallization was attributed to a change in the electric field intensity. They presented the hypothesis that the conductor acts like a dipole antenna. This increases the electric field intensity around the sample, which provides more energy to the film and enhances crystallization from the amorphous state. However, the exact explanation for different crystallization behavior was not provided.

In summary, plasma exposure has been shown to crystallize TiO_2 and ITO films at temperatures significantly lower than the temperature required with traditional RTA and furnance annealing. In addition, it was shown that the crystallization process via plasma depends upon the gas pressure and that the optimum gas pressure depends upon the plasma gas species. The presence of a floating backside conductor was shown to enhance the plasma crystallization performance. Based on his temperature measurements, Ohsaki proposed a theory whereby the activation process for the low temperature crystallization may be due to the rf electromagnetic fields.

Nevertheless, the reduction in the thermal budget of the crystallization of TiO_2, ITO and Lanthanum oxide (La_2O_3) films [21-26] makes plasma annealing a potential technique to crystallize the complex oxide films such as $Bi_2Dy_1Fe_4Ga_1O_{12}$ at low temperatures. In addition to the low temperature crystallization, plasma annealing has also been shown to improve the electrical & optical properties of the aluminum doped zinc oxide (AZO) and ITO films [29, 30], and hall mobility & work function of ITO films [31]. Some early experiments conducted at UWA prior to my work indicated that more complex oxides such as iron garnets could also be crystallized in a plasma [32].

1.3 Thesis objective

The aim of the work presented in this thesis is to examine the crystallization [33] process via plasma exposure. In order to investigate the plasma annealing mechanism, the work is divided into two sections:

- Since the crystallization conditions were shown to depend upon the process conditions, it is therefore important to understand the plasma characteristics with varying process conditions. In addition, lowering the thermal budget is an essential requirement in order to integrate this material with the silicon industry. Therefore, the first section of this thesis will concentrate on the accurate measurements of sample temperature during exposure to a plasma. Further, to better understand the process conditions in the plasma, we will also investigate the plasma species and ways to measure and characterize the processes within a plasma.

- The second section of this thesis will investigate the plasma crystallization process as a function of rf power and pressure, and compare the plasma treated garnet thin films with RTA and furnance annealed films.

1.4 Thesis organization

This thesis has been organized to systematically discuss plasma annealing, from providing a basic understanding of plasma physics to the characterization of plasma parameter space and annealing of $Bi_2Dy_1Fe_4Ga_1O_{12}$ (BiDyGa:IG) films.

Chapter 2 will discuss the basics of plasma physics involved in capacitively coupled plasmas. It will also discuss ionization and recombination processes in an oxygen plasma as a function of process parameters (rf power and pressure). These processes will be used in characterizing plasma species in subsequent chapters.

Chapter 3 will provide the general background of the BiDyGa:IG films. In addition, this chapter will present the experimental methods for characterizing BiDyGa:IG films used in this thesis.

In Chapter 4, infrared thermometry will be used to measure the sample temperature during plasma exposure. Furthermore, the dependence of oxygen plasma species (ions, and neutrals) with respect to process parameters, such as rf power (500-800 Watts) and pressure (2-5 Torr) will be discussed with the help of optical emission spectroscopy and Langmuir probe measurements. Further, it has been shown by Ohsaki *et al.* [25] that placing a floating conductor in thermal contact with sample increases the effectiveness of the crystallization. Hence, we will investigate the effects of a backside conductor on sample temperature, plasma species and ultimately on crystallization conditions.

In Chapter 5, BiDyGa:IG films will be treated under different oxygen plasma conditions to identify the optimum crystallization conditions. Additionally, in order to understand how the plasma annealing differs from RTA and furnance annealing, we will compare properties such as crystallinity, Faraday rotation, optical transmission, surface roughness, and chemical composition of plasma-annealed films with RTA and furnance annealed films.

This thesis will conclude with Chapter 6, where a summary, conclusions and recommendations for future work are presented.

2

Plasma physics and heating mechanisms

This chapter is dedicated to providing an overview of plasma physics with particular reference to capacitively coupled plasmas in a cylindrical chamber. It begins with a basic introduction to plasmas and the reactions that may be involved in the generation and recombination of oxygen plasma species. It then provides a detailed explanation of different plasma regions and the heating mechanisms involved in producing energetic electrons to create the ionization. The last section discusses the energy distribution of electrons in the system and its variations with rf power and pressure.

2.1 General background

Plasmas are one of the four fundamental states of matter (the others being solid, liquid, and gas). A plasma is basically a collection of neutral and charged species (such as positive and negative ions) and electrons, which are generated by the ionization of gases. Ionization can either be induced by heating a gas or by applying strong electromagnetic fields with a laser or radio frequency (rf) power supply that ionize molecules or atoms in the gas, thus turning it into a plasma.

There are strong interactions between particles in the plasma because of the presence of electrically charged particles. These charged species also mean that plasmas can conduct electric current, which a gas cannot do, and that they interact strongly wih electric and magnetic fields. In order to sustain the ionization state some form of energy must be continually supplied to the plasma. The energy can be applied in the form of rf power to the system. The plasma generations relies on inductive or capacitive rf power transfer to the gas, and are generally termed as inductively coupled plasmas (ICP) or capacitively coupled plasmas (CCP), respectively.

In order to generate an inductively coupled plasma, an rf voltage is applied to the coil, resulting in an rf current that induces a magnetic field in the reactor. The time-varying axial magnetic flux density induces an electric field. The electric field accelerates electrons, which absorb energy. Through collisions, these electrons further ionize the gas. Fig. 2.1.1 shows a typical diagram of an ICP.

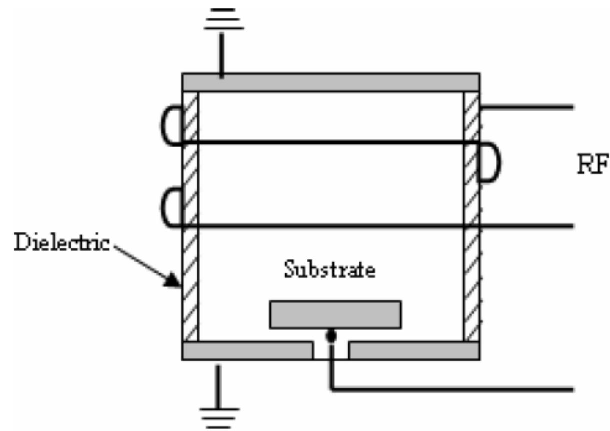

Fig. 2.1.1: Inductively coupled plasma set-up

The set-up for capacitively coupled rf discharges consists of two parallel electrodes separated by a gap into which the plasma gas is introduced (see Fig. 2.1.2). In general, one electrode is kept at ground potential while the other is connected to a high frequency (usually 13.56 MHz) power generator.

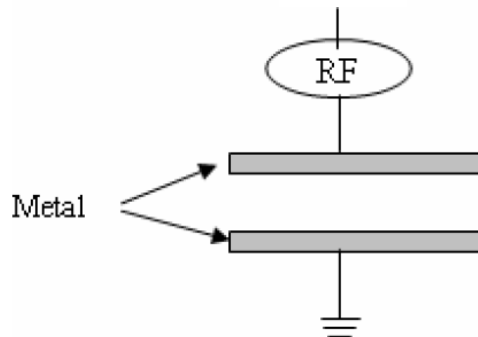

Fig. 2.1.2: Capacitively coupled plasma set-up

In capacitive plasmas, the electron temperature T_e, generally exceeds the ion and neutral gas temperatures T_i and T_g. For that reason, these discharges are usually denoted as "*cold*" plasmas in reference to the low temperature of the heavy particles. The density and the temperature of ions are higher in the case of inductively coupled plasmas as compared to capacitively coupled plasmas. Hence, they are known as "*hot*" plasmas. Both inductively and capacitively coupled plasmas are widely used in

semiconductor processes such as etching, deposition of oxides, nitrides, and other films, cleaning chambers, and plasma chemical synthesis [34-37].

The research in this thesis aims to lower the temperature required for crystallization of the bismuth substituted iron garnet thin films in comparison to temperatures required in conventional furnance and rapid thermal annealing. A capacitively coupled plasma has been demonstrated to crystallize films like TiO_2 and ITO at low temperatures, that are claimed to be as low as 150 °C [22-26]. This previously reported work was conducted using a capacitively coupled plasma at 13.56 MHz and we will use similar equipment and conditions in this thesis. Hence, this chapter will focus predominantly on capacitively coupled plasmas.

2.2 Ionization and recombination reactions in O_2 plasma

In this work, crystallization is achieved using an oxygen plasma [1]; hence, this discussion is limited to O_2 plasma species. Table 2.2.1 shows the reactions that occur between neutral and charged species in an oxygen based plasma as reproduced from ref [38, 39]. ϵ_T represents the threshold energy required to achieve the ionization and dissociation through electron collisions. These reactions include the following species:

- 4 neutral species: Ground state oxygen (O_2), meta-stable oxygen (O_2 ($a^1\Delta g$)), ground state atomic oxygen (O^3P) and metastable atomic oxygen (O^1D).
- 5 charged particles: O_2^+, O^+, O_2^-, O^- and electrons.

[1] Some work was conducted using a nitrogen plasma and these results are outlined in Appendix II.

Table 2.2.1: Reactions of each particle assumed to occur in O_2 discharge

No.	Reactions	ϵ_T(eV)	Type of Reaction
	Electron Collisions		
1.	$O_2^+ + e^- \rightarrow O(^3P) + O(^3P)$	0.01	Recombination
2.	$O_2 + e^- \rightarrow O_2(a^1\Delta_g) + e^-$	0.98	Excitation
3.	$O^- + e^- \rightarrow O(^3P) + 2e^-$	1.46	Dissociation
4.	$O_2(a^1\Delta_g) + e^- \rightarrow O(^3P) + O^-$	3.64	Dissociative attachment
5.	$O_2 + e^- \rightarrow O(^3P) + O^-$	4.20	Dissociative attachment
6.	$O_2(a^1\Delta_g) + e^- \rightarrow 2O(^3P) + e^-$	5.02	Dissociation
7.	$O_2 + e^- \rightarrow 2O(^3P) + e^-$	6.00	Dissociation
8.	$O_2(a^1\Delta_g) + e^- \rightarrow O(^3P) + O(^1D) + e$	7.42	Dissociation
9.	$O_2 + e^- \rightarrow O(^3P) + O(^1D) + e^-$	8.40	Dissociation
10.	$O_2 + e^- \rightarrow O(^3P) + O(^1D) + e^-$	9.97	Dissociation
11.	$O(^1D) + e^- \rightarrow O^+ + 2e^-$	11.60	Ionization
12.	$O_2 + e^- \rightarrow O_2^+ + 2e^-$	12.06	Ionization
13.	$O(^3P) + e^- \rightarrow O^+ + 2e^-$	13.60	Ionization
14.	$O_2 + e^- \rightarrow O^+ + O(^3P) + 2e^-$	16.81	Ionization
15.	$O_2 + e^- \rightarrow O^+ + O^- + e^-$	17.00	Ion-Pair formation
	Ion-neutral and ion-ion		
16.	$O + O^- \rightarrow O_2 + e^-$		Charge transfer
17.	$O^- + O_2 \rightarrow O_2^- + O$		Charge transfer
18.	$O^+ + O_2 \rightarrow O_2^+ + O$		Charge transfer
19.	$O^- + O_2^+ \rightarrow O + O_2$		Recombination
20.	$O_2^- + O_2^+ \rightarrow 2O_2$		Recombination
21.	$O^- + O_2(a^1\Delta_g) \rightarrow O_2 + e^-$		Associative detachment
22.	$O_2^- + O_2(a^1\Delta_g) \rightarrow 2O_2 + e^-$		Associative detachment
	Neutral-neutral		
23.	$2O + O_2 \rightarrow 2O_2$		Recombination
24.	$O + O \rightarrow O_2$		Recombination
25.	$O_2(a^1\Delta_g) \rightarrow O_2$		De-excitation

Table 2.2.1 illustrates that, in addition to electron collisions, ionization and dissociation can also be achieved by the ion-neutral reactions through charge transfer (reactions 17 &18); however, it is achieved primarily through the electron collisions (3-

15). The dissociative attachment (4 & 5) and charge transfer (17 & 18) reactions result in the generation of both ion and atomic oxygen, while ion-pair formation reaction generates both positive and negative ions (reaction-15).

Recombination, on the other hand, can be achieved by ion-neutral/ion-ion, neutral-neutral and low energy electron reactions. The associative detachment (21 & 22) reactions are also known as the recombination reactions. It can also be seen that when the electron energy is low, the electron collisions can also result in recombination (reaction-1).

2.3 Physical description of a capacitively coupled plasma

Describing a plasma precisely and in detail is difficult, as it involves many reactions that depend heavily on the external parameters (power and pressure) [39-43]. Hence, it is helpful to try to obtain an approximate description of real plasmas using simple physical reasoning and then explain the variations with power and pressure.

To begin with, the plasma can basically be divided into two sections namely: “sheath” and “bulk”. When a sufficiently high voltage is applied between the electrodes, ionization of the gas occurs and generates a collection of charged particles (ions and electrons) and neutral particles. The region where these reactions occur is known as the “bulk” plasma.

There are various species that can be formed in the plasma as we have seen in Table 2.2.1 above. Therefore, when an rf voltage is applied to the electrode, different particles respond differently to the rf cycle. The particles of interest are negatively and positively charged species, as they are crucial in creating different plasma regions. An important

parameter, especially relating to particle dynamics in plasma is the angular frequency, which describes the collective response of particles in radio frequency plasma. The angular frequency defines the rapid oscillations of the electron density or ion density in conducting media, such as plasmas. These oscillations are dependent upon the mass of charge carriers, their density and the dielectric strength of the conducting medium. Equation 2.3.1 shows that the angular frequency for both electrons and ions is inversely proportional to the square root of mass and is directly proportional to the square root of number density of the particles. In addition, the ion angular frequencyis proportional to the average charge state (Z), which is defined as the ratio of electron density to the ion density (n_e/n_i).

$$\omega_{pe} = \sqrt{\frac{n_e e^2}{m_e \varepsilon_0}} \omega_{pi} = \sqrt{\frac{n_i e^2 Z^2}{m_i \varepsilon_0}} \qquad \textbf{2.3.1}$$

where,

ω_{pe}	=	angular frequency of electrons
ω_{pi}	=	angular frequency of ions
m_e	=	mass of electron
m_i	=	mass of ion
Z	=	average charge state
n_e	=	number density of electrons
n_i	=	number density of ions
e	=	elementary charge

The values of angular frequency for positive ion (O^{2+}), negative ion (O^-) and electron and their densities at parameters close to our experimental power and pressure range are taken from ref. [39] and shown in Table 2.3.1.

Table 2.3.1:Angular frequency of electrons, O_2^+ and O^-.

Particle	m (kg)	n (m^{-3})	$Z = \left(\frac{n_e}{n_i}\right)$	ω (rad/sec)
e	9.1×10^{-31}	10^{15}	---	1.78×10^{9}
O_2^+	5.31×10^{-26}	10^{16}	0.1	2.36×10^{6}
O^-	2.66×10^{-26}	10^{16}	0.1	3.3×10^{6}

It can be seen from the Table 2.3.1 that the electrons have greater mobility than both positive and negative ions.. Further, the angular frequency of the applied voltage of capacitively coupled plasma equipment in our experiments is 85.2×10^{6} rad/sec (for 13.56 MHz), which is well below the angular frequency of electrons and well above the angular frequency of the ions. Therefore, the electrons can almost instantaneously follow the variation in the rf field, whereas the ions cannot. This difference in response of electrons and ions creates different regions inside the plasma under the applied rf power.

During the positive rf cycle, electrons get attracted to biased electrode. This creates a thin layer of negative charges on the electrode (chamber wall nearest to the electrode). This negative charge layer (NCL) then starts repelling other electrons away from the electrode and at the same time starts attracting positive ions. The positive ions come closer to the NCL until the attractive forces from NCL and repulsive forces from the electrode balance out. When the equilibrium is reached, the positive ions create a belt close to the NCL separated by a small distance. This belt of positively charged ions is known as the “Sheath”, thickness of which is defined as the distance from negative

charge layer to the sheath-bulk boundry. Fig. 2.3.1 shows the plasma regions in a capacitively coupled plasma chamber under positive bias.

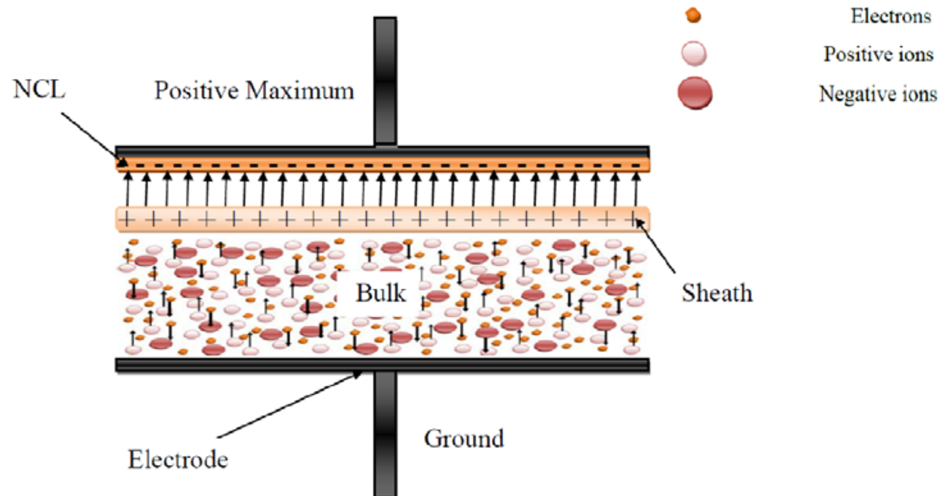

Fig. 2.3.1: Capacitively coupled rfdischarge under positive voltage.

It can be seen that the positive ions and NCL are separated by a distance. This space is created as a result of the balance of attractive forces between the NCL and the positive ions and the repulsive force between electrode and the positive ions. The positive charges in the sheath are the starting point for the electric field lines that end at the NCL. The presence of two layers of opposite charges creates an electrostatic potential between them (NCL and sheath). The NCL pushes the electrons towards the bulk and attracts the positive ions towards electrodes. Only the electrons that have sufficient energy to cross the electrostatic potential barrier will be able to reach the electrode. Electrons with low energy are repelled by the NCL and pushed back to the bulk plasma, which results in an increased electron concentration in the bulk plasma. The high concentration of electrons turns the bulk plasma into a weak conductor. The electrostatic potential also attracts the positive charges towards electrodes, but as can be seen from Table 2.3.1 the positive ions are heavier and slower than the electrons and

hence it is impossible for them to follow the rf cycle. So these ions tend to stay in the bulk after their generation (except at low pressures, when the mean free path is high).

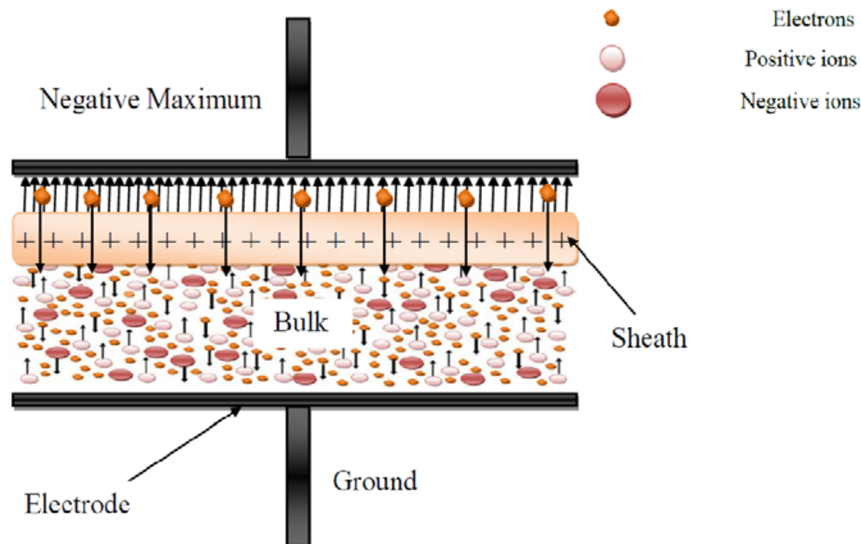

Fig. 2.3.2:Capacitively coupled rf discharge under negative voltage

During the negative part of the rf cycle, shown in Fig. 2.3.2, electrons are repelled away from the electrode and the positive ions move slowly towards the electrode. More positive ions are added to the sheath under the effect of negative potential on the electrode. This results in an increased electric field between the electrode and sheath. The electroderepelsthe electrons through this increased electric field created between the electrode and the sheath, and they are accelerated towards the bulk. In this way, the energetic electrons are accelerated towards the bulk to create further ionization.

2.4 Thickness of sheath

The rf cycle results in the repetitive expansion and compression of sheath. The sheath thickness must be known for our experiments, as we believe that the conditions need are best achieved in bulk region rather than the sheath. It is therefore necessary to understand the sheath thickness and its variations with rf cycle so that the samples can

be accurately placed in bulk. Sheath behaves differently in different pressure conditions and the sheath thickness can be defined by three formulas depending on pressure:

- For low pressures (P < 0.1 Torr) the sheath thickness is given by Child Langmuir law [44] as:

$$d = 1.5\sqrt{\varepsilon_0}\left(\frac{2eV_s^3}{m_i\,J_i^2}\right)^{1/4} \qquad \textbf{2.4.1}$$

where,			
	d	=	sheath thickness
	m_i	=	mass of ions
	J_i	=	ion current density at the plasma-sheath boundary
	V_s	=	voltage across the sheath (~ cathode voltage)
	ε_o	=	dielectric constant
	e	=	elementary electric charge

Equation 2.4.1 shows that the sheath thickness is related to the voltage applied ($V_s^{3/4}$), current density ($J_i^{1/2}$) and mass of the positive ions ($m_i^{1/4}$). It can be seen that at low pressures (<0.1 Torr), the sheath thickness is independent of the pressure.

- For intermediatepressures (0.1 < P < 1 Torr), the equation for the sheath thickness changes to [45]:

$$d = 1.23\left(\frac{2em_i\,\varepsilon_0^2\,V_s^3}{\lambda_i\,J_i^2}\right)^{\frac{1}{5}} \qquad \textbf{2.4.2}$$

where,	λ_i	=	mean free path of ions.

Equation 2.4.2 shows that at intermediate pressure the sheath thickness dependences on theion mass, ion density and applied voltage have been reduced from a factor of 1/4 to 1/5. In addition, it becomes a function of mean free path ($\lambda_i^{-1/5}$). The mean free path is directly proportional to pressure. Therefore, under constant voltage and ion density, sheath thickness becomes inversely proportional to $P^{1/5}$.Regardless, the magnitude of change of sheath thickness with changing pressure is relatively small due to the exponential dependence.

- For higher pressures (P > 1 Torr), the sheath thickness is determined by ionization effects [46], and is given by:

$$P_d = \frac{1}{(\alpha/P)} ln\left(\frac{1+\gamma}{\gamma}\right) \qquad \textbf{2.4.3}$$

where, γ = Secondary electron emission coefficient of the cathode electrode material

α/P = First ionization coefficient divided by pressure

P_d = Pressure and sheath thickness product.

Under this high-pressure conditions, the product of sheath thickness and pressure, P_d, becomes constant; that is, the sheath thickness becomes inversely proportional to the pressure. The sheath thickness starts falling linearly with increase in pressure above 1 Torr. Ward has calculated the value of P_d for different noble gasses (shown in Fig. 2.4.1) as a function of atomic mass [47].

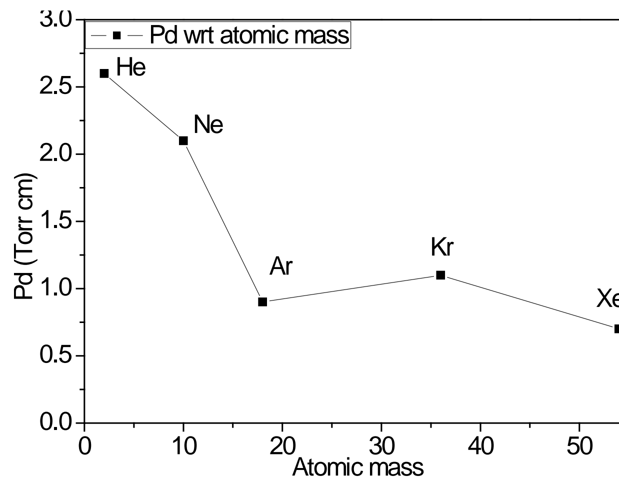

Fig. 2.4.1: Pd (Torr-cm) as a function of atomic mass.

It can be seen from the plot that the P_d value generally decreases with increase in the mass. Further, the value of P_d for nitrogen was shown to be between 0.31-0.42 Torr-cm [47]**.** Since the atomic mass of the oxygen is comparable to nitrogen, the P_d value for oxygen is expected to be comparable to nitrogen's P_d value. For oxygen, Sommerer and Kushner [48] measured the sheath thickness to be approximately equal to 0.11 cm at a pressure of 2 Torr [P_d = 0.23 Torr-cm]. This supports our notion of choosing Equation2.4.3 for the measurement of sheath thickness for our experiments between 2-5 Torr, which results in a sheath thickness between 0.11-0.04 cm. For rf discharges, a sinusoidal variation of the sheath thickness (d)between 0 (approximately) and 2d was observed in the pressure range of 1-40 Torr **[49].** This means that we can expect a maximum sheath thicknessof 0.22 mm (2 Torr) during our experiments. As we keep our samples at least 10.5 cm from the biased electrode, we can be relatively certain that our samples are placed in the bulk region of the plasma.

2.5 Local and non-local electron heating

To maintain the plasma, the ionizationrate must be greater than the recombination rate. As discussed earlier in section2.3, the ionization and dissociation is primarily achieved by electron collisions with molecules and neutral species. It can be seen from reactions 1-14 in Table 2.2.1 that the resultant products change with threshold energy. It is therefore important to understand the process via which the electrons gain energy in the plasma, as this will also provide the information of the resultant products in our experimental range. In plasmas, the energy of electrons is defined in terms of the kinetic energy that is gained by moving an electron by a distance without collisions (mean free path). This energy is represented as electron temperature. It is measured inelectron volts and is an indirect measure of the thermal kinetic energy per particle. The degree of ionization therefore is proportional to the electron temperature in plasma.

If the angular frequency of the electron is much larger than the frequency of the rf signal in the plasma chamber then the average electron energy (ϵ_e) an electron acquires will be relatedto its mean free path (λ_{ie}) and electric field E.

$$\epsilon_e \;=\; eE\lambda_{ie} \qquad \textbf{2.5.1}$$

The mean free path is (usually) inversely proportional to the number of neutral particles in the plasma. Therefore, the mean free path varies as 1/N, where N is the concentration of neutral particles. As the concentration of neutral particle increases, the number of collisions increases and the electron loses some of its energy. This means that the mean free path multiplied by E is proportional to E/N; so the average electron energy is consequently expected to depend on E/N instead of just E.

In plasmas, the electron temperature can be increased by two methods that are generally referred to as non-local heating and local heating. As discussed in section 2.3, the sheath expands and contracts with oscillating rf power, and the electrons during the negative part of the voltage cycle are accelerated away from the electrode gaining energy from the applied potential and the electric field due to the sheath. These high-energy electrons enter the bulk plasma and induce ionization. This process of generating energetic electrons is known as non-local heating as the electrons achieve this energy while travelling across the sheath region and were not localized in the bulk.

The second heating mechanism is local heating, where the majority of the energetic electrons are produced in the bulk region. This type of heating can only happen if the electric field strength in the bulk is strong enough to produce electrons with sufficient energy to generate ionization reactions.

The dominance of one region over the other can be determined by the E/N ratio of the bulk. A high E/N ratio favors local heating while a low E/N ratio favors non-local heating. The mathematical equation for E/N ratio taken from [50] is

$$\frac{E}{N} = \omega_{rf}\sqrt{\left(\frac{0.1\varepsilon_0 V_s}{2\,n_m e}\right)} \qquad \textbf{2.5.2}$$

where,

where,	E	=	electric field in bulk
	ω_{rf}	=	$2\pi\upsilon_{rf}$, υ_{rf} = rf frequency (13.56 MHz)
	N	=	concentration of neutral particles
	V_s	=	root mean square voltage

n_m = ion density in the bulk plasma

ε_o = dielectric constant

e = elementary electric charge

Equation 2.5.2 shows that the E/N ratio is proportional to the rms voltage and inversely proportional to the bulk ion density. The conclusion from this is that if n_m increases with the applied power by more than the V_s itself, then the E/N ratio decreases and the majority of electrons will then receive the majority of their energy via a non-local heating mechanism. On the other hand, if V_s increases at a greater rate than the bulk ion density, the E/N ratio will be higher and the electrons will gain the energy to induce ionization mainly via local heating mechanisms.

2.6 Electron energy distribution function

It was shown in Table 2.2.1 that most of the ionization and dissociation processes involve electron collisions (reactions 3-14). Further, the generation of various plasma species (due to ionization and dissociation) via electron collisions depends on the energy carried (threshold energy) by the electrons. It can be seen that the ionization is achieved only after the electrons have energies more than 11.6 eV, while the dissociation starts at energies as low as 1.46 eV. From reaction-1, it is clear that if the electrons have very low energy then the collisions can result in recombination. Therefore, the electron energy is an important parameter in predicting the species present in the plasma.

An electron in a plasma can theoretically have any energy; however, some of the energies are more probable than others. The electron energy distribution function (EEDF), sometimes referred to as the electron energy probability function, which is the statistical probability that a particle will have a certain energy. The EEDF has been shown to be dependent upon both rf power and pressure [51-53]. Fig. 2.6.1 shows typical variations in the electron energy probability function with respect to electron energy for rf power increasing from 0 to 100 Watts.

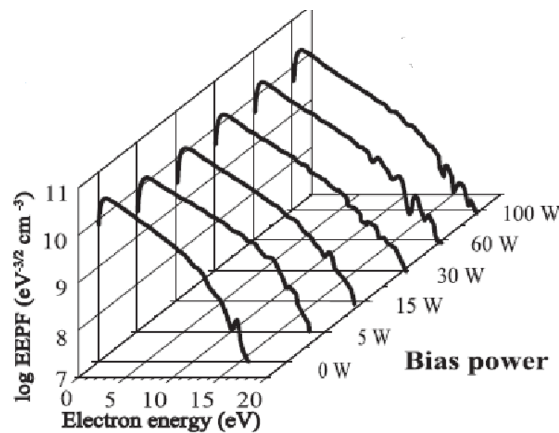

Fig. 2.6.1: EEPF as a function of electron energy for rf power between 0 and 100 Watts [52].

It can be seen from Fig. 2.6.1 that the density of electrons in the high electron energy spectrum (15-20 eV) increases with increasing power. Table 2.2.1 lists the dissociation and ionization processes, and the minimum or threshold energy (ϵ_T) needed for these reactions to occur. The reactions can only proceed once enough energy is provided. From Fig. 2.6.1, it can be observed that the electron density in the high-energy tail increases with increasing power. As this density increases with power, we may say that power favors ionization. In this thesis, we are using rf power in the range of 500-800 Watts, and hence the distribution function and the resultant species for our

experiments will be different from Lee *et al.* [52]. However, the trend of increasing ionization with increasing power should still be evident.

An increase in the pressure, on the other hand, increases the number of gas particles per unit volume, which results in an increase in the number of collisions and a decrease in the mean free path. Electrons lose some energy with every collision and consequently the average energy carried by the electrons decreases with increasing pressure. Fig. 2.6.2 shows typical variations in the electron probability function as a function of pressure.

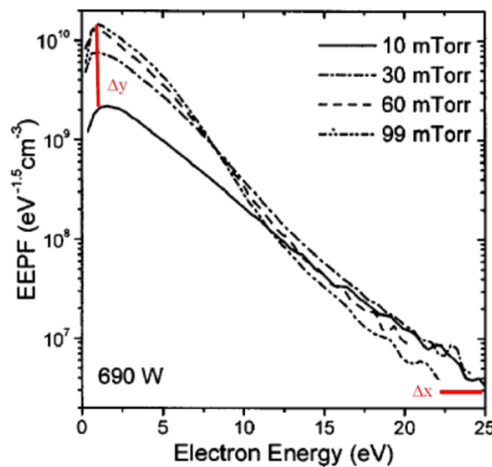

Fig. 2.6.2: EEPF as a function of electron energy with pressure as parameter [53].

It can be seen from Fig. 2.6.2 that the maximum energy of electrons has decreased by a factor of Δx (25 to 22.5 eV) with an increase in pressure from 10 to 99 mTorr. Additionally, the electron density in the lower energy spectrum has increased by a factor of Δy (10^{09} to ~10^{10} cm^{-3}) with increase in pressure. As an increase in pressure shifts the distribution function to the left causing the high-energy electron density to decrease, we may say that the probability of ionization decreases as the pressure increases. Therefore, it can be said that increasing pressure favors recombination.

2.7 Summary

In this chapter, we have developed a basic understanding of plasma regions, and the reasons for differentiating the regions into the “sheath” and the “bulk”. We have also discussed two heating processes for the electrons namely “non-local” and “local” heating, which were shown to be related to the sheath and bulk regions of the plasma. Finally, we discussed the electron energy distribution function, which was shown to be dependent upon the applied rf power and pressure. Based on that, we obtain an understanding that increasing rf power increases the probability of ionization, while an increase in pressure increases the probability of recombination.

3

Material and characterization methods

This chapter provides background on the materials and characterization methods used to examine both the plasma and the thin film material (before and after annealing). The chapter begins with a general background of the bismuth substituted iron garnet ($Bi_2Dy_1Fe_4Ga_1O_{12}$) film. In the next section, plasma characterization methods such as optical emission spectroscopy, Langmuir probe, and infrared thermometry will be discussed. The last section will discuss material characterization techniques such as X-ray diffraction (XRD), atomic force microscopy (AFM), transmission electron microscopy (TEM), electron probe micro analysis (EPMA), and X-ray photoelectron spectroscopy (XPS).

3.1 Bismuth dysprosium gallium iron oxide

Magnetic garnets are cubic crystals having 160 ions per cubic unit cell. The garnets are ionic crystals with the general composition of

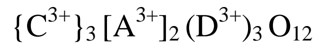

$$\{C^{3+}\}_3\,[A^{3+}]_2\,(D^{3+})_3\,O_{12}$$

There are three different sets of lattices that are occupied by the cations in the crystal: namely, dodecahedral, octahedral, and tetrahedral sites The dodecahedral sites {C} are occupied by the larger cations like Bi^{3+}, Ce^{3+}, Y^{3+}, or La^{3+} ions. The octahedral [A] and tetrahedral (D) are occupied by smaller sized ions such as iron. The cubic unit cell is shown in Fig. 3.1.1.

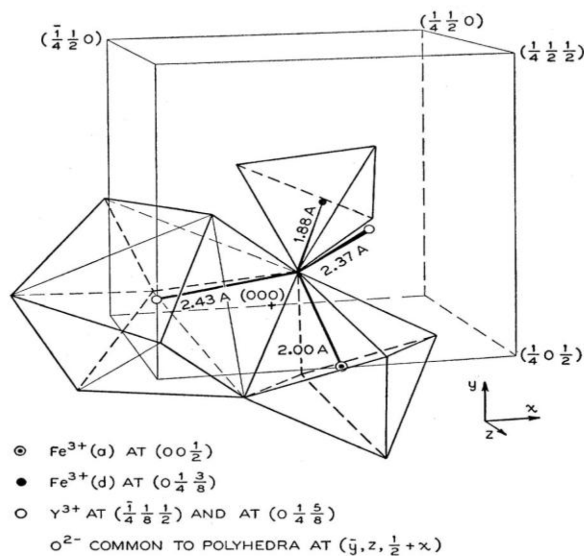

Fig. 3.1.1: Unit cell of Yttrium Iron Garnet (YIG) with the different sites for cations and their oxygen environment [54].

The [A] and (D) sublattices are coupled anti-ferromagnetically which yields a ferrimagnetic crystal. When the dodecahedral lattice is not occupied by the paramagnetic ions the saturation magnetization of the crystal is the vectorial sum of the [A] and (D) sublattice magnetizations. Without the substitution of Fe^{3+} ions by ions like

Ga^{3+} or Al^{3+}, the magnetization of the (D) tetrahedral sublattice dominates. Ga^{3+} and Al^{3+} are initially incorporated on tetrahedral sites so that an increased substitution level of these ions will lead to the magnetic dominance of the octahedral sublattice. At a certain substitution level, both sublattices are equivalent and the magnetizations of the two sublattice compensate each other and the crystal becomes antiferrimagnetic [55].

The simplest form of the bismuth iron garnet is $Bi_3Fe_5O_{12}$, where Bi^{3+} ions are distributed over the dodecahedral coordinated (24c) sites, while two Fe^{3+} occupy octahedral [16a] sites, and three Fe^{3+} occupytetrahedral (24d) sites. Two Fe^{3+} ions at tetrahedral site cancel two Fe^{3+} ions at octahedral site, leaving one Fe^{3+} ion at tetrahedral site. The Fe^{3+} ions absorb light much more strongly than the rare-earth ions at energies corresponding to visible and ultraviolet light of the electromagnetic spectrum [56]. This optical absorption gives rise to electric dipole transitions that result in the rotation of the polarized light by some angle when passed through the garnet sample. This rotation of polarized light is known as the Faraday rotation. With Bi^{3+}a very strong Faraday rotation is obtained in the visible range, as Bi^{3+} ions at dodecahedral site enhances iron ion transitions to increase the Faraday rotation of the garnet samples [57].

The magnetic and optical properties of $Bi_3Fe_5O_{12}$ can further be modified by adding different metals like Dysprosium and Gallium[3, 58]**.** The $Bi_3Fe_5O_{12}$lacks uni-axial anisotropy, which is crucial factor in many applications. Therefore, to solve this problem, Dysprosium is added to the compound, as it provides large magneto-striction constants and their sign leads to positive uni-axial anisotropy.

Second problem is the low optical transmission at wavelength shorter than 550 nm.Scott[59] explained that the transmittance depends upon split energy levels at both octahedral and tetrahedral sites. Gallium lowers thenumber of iron ions at tetrahedral sites, thus reducing the effects of Fe^{3+} ion transitions. This reduces the Faraday rotation but increases the optical transmissions in the visible region, as gallium absorbs less than iron. It was reported that with the addition of Gallium ions optical transmission was increased at wavelength of 532nm [3].

3.1.1 Garnet sample description

Films with the general chemical formula $M_3Fe_{5-x}Z_xO_{12}$ (where M is a combination of Bi, Dy, Ce, Y and/or Eu and Z is Al or Ga) can be deposited amorphously via methods like pulsed laser deposition (PLD), liquid phase epitaxy (LPE) ,ion beam sputtering (IBS), reactive ion beam sputtering (RIBS), sol-gel process, and rf magnetron sputtering, and subsequently annealed to form the garnet phase. Generally, the rf sputtering is used to deposit amorphous films as it provides good uniformity over the large area. The garnet samples we are trying to crystallize are 300 nm thick and are deposited on fused quartz substrates (diameter: 2.5 cm) via rf-sputtering by Plasma Quest Ltd, UK [60]. All the deposited samples are amorphous prior to annealing with a nominal composition of $Bi_2Dy_1Fe_4Ga_1O_{12}$.

3.2 Plasma barrel asher

Capacitively coupled plasmas (CCP) are one of the most common types of industrial plasma systems. They essentially consist of two metal electrodes separated by a distance. For our experiments, the CCP system is driven by a single radio frequency

(rf) power supply operating at a frequency of 13.56 MHz. The rf generator, RF-10S by Advanced Energy has a maximum power of 1000 Watts, is used to generate the rf power in the range of 500-800 Watts for our experiments. The power is fed to the barrel asher, with a characteristic load of 50 ohms. This impedance is kept constant with varying pressure and power via a closed loop, power regulation mode (1% into 50 ohms), in the power supply.

The plasma barrel asher PM-600 (see Fig. 3.2.1), from March Instruments, is used for the generation of an oxygen plasma.It is equivalent to the plasma barrel asher used by Oshaki *et al*. [25]. It has a diameter of 25 cm and a length of 30.5 cm. The upper electrode is connected to the rf source, and the lower electrode is grounded. This configuration is similar in principle to a capacitor in an electric circuit, and hence the plasma formed in this configuration is called a capacitively coupled plasma.

Fig. 3.2.1 Shows the cylindrical March barrel asher

The plasma chamber's front window/cover has been modified to allow a removable port to which either a ZnSe or quartz window is attached. The thermal measurements

that were performed with an IR imaging camera were taken with ZnSe window on the asher, while fused quartz window was used for the optical emission measurements. The sample was placed vertically in the middle of the chamber for optical emission measurements, temperature measurements and annealing purposes. A custom designed sample holder (as shown in Fig. 3.2.2) was used for this purpose. It can be seen from Fig. 3.2.2 that sample holder does not place the sample exactly in the middle of the chamber. It places the sample's top edge at a distance of 10.5 cm from the upper electrode and the bottom edge at a distance of 12 cm from the bottom electrode.

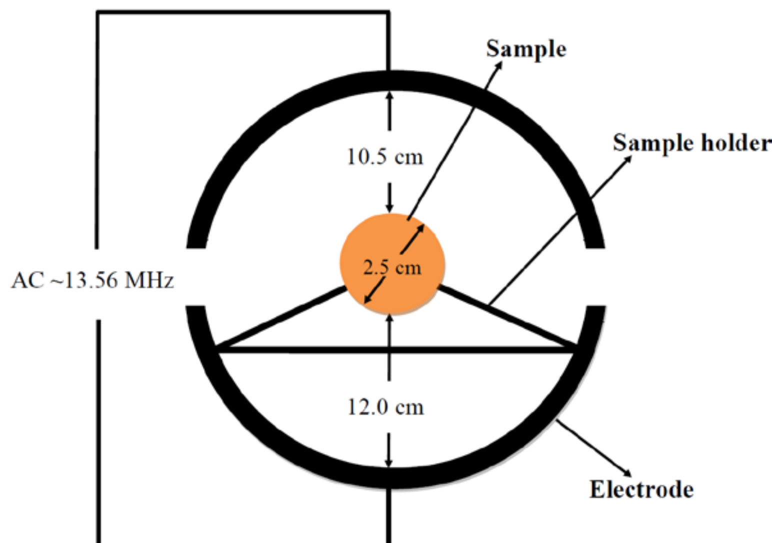

Fig. 3.2.2Schematic of plasma barrelasher with sample inside.

3.3 Thermal imaging

We needed the temperature measurements to be non-invasive so that precluded methods such as a thermo-couple which may disturb the conditions within plasma. We tried some measurements with the same optical probe technique that Ohsaki reported (IT-540 N, Horiba Ltd) [25], however we were not satisfied that we could adequately localize the temperature measurements to the sample. Hence, a thermal imager was used to measure the sample temperature non-invasively within plasma.

Any object at a temperature above absolute zero emits radiation in the form of electromagnetic waves. The thermal motion of charge particles, such as protons and electrons, and their interactions result in charged acceleration and dipole oscillation which result in the emission of photons from the material. This results in the generation of coupled electric and magnetic fields, resulting in the emission of photons, radiating energy away from the body through its surface boundary. The characteristics of thermal radiation depend on the surface it is emanating from, its temperature, and spectral emissive power. When radiative power is incident on an object, a fraction of the power is reflected, another portion of power is absorbed, and the final fraction is transmitted through the object. Hence, the total energy of the object is a combination of absorbed, transmitted and reflected energy.

$$\gamma_a + \gamma_{\mathrm{t}} + \gamma_r = 1 \qquad \textbf{3.3.1}$$

where, γ_{a} = absorbed energy.

γ_{t} = transmitted energy.

γ_{r} = reflected energy.

When a thermal imager is used to measure the temperature, it receives the energy in the form of radiance, which is defined as the quantity of radiation received within a given solid angle from a specified direction. The total radiance reaching the thermal sensor is described in Fig. 3.3.1.

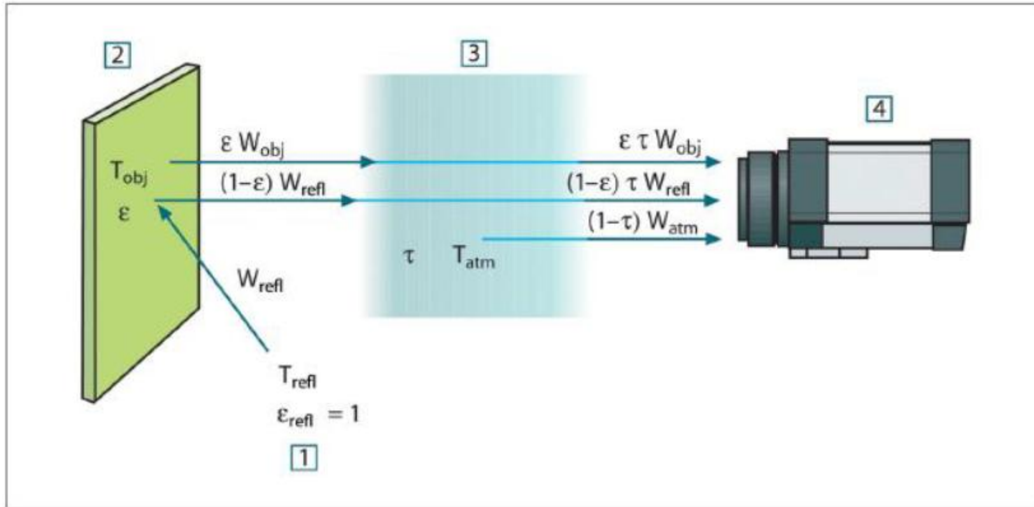

Fig. 3.3.1: Total radiance received by thermal sensor.

It can be seen that the total radiance received is a combination of emitted, reflected and absorbed radiance. The theoretical formula that describes the radiance reaching the sensor of the thermal imager is shown in Equation 3.3.2.

$$W = \varepsilon W_{obj} + (1-\varepsilon)\tau W_{ref} + (1-\tau)W_{atm} \qquad \textbf{3.3.2}$$

where,

W	=	received radiance [W/m^{2}sr].
$W_{obj.}$	=	sample radiance [W/m^{2}sr] .
W_{ref}	=	reflected radiance [W/m^{2}sr].
W_{atm}	=	absorbed radiance by atmosphere [W/m^{2}sr].
ε	=	emissivity of the sample.
τ	=	transmittance of the atmosphere.

It can be seen from Equation 3.3.2 that the total radiance received by the thermal imager is affected by reflected and transmitted radiance. The radiance of the object provides the true temperature measurements, and therefore W_{obj} needs to be measured. The total radiation is also affected by atmospheric absorption. The radiance received by the thermal imager from the object is also a function of emissivity, which is defined as the ability of a material to emit thermal radiation that it has absorbed. The maximum achievable value of the emissivity is unity. When the emissivity of the material becomes unity, the material becomes a perfect emitter (zero reflection). A material with unity emissivity is called a black body source.

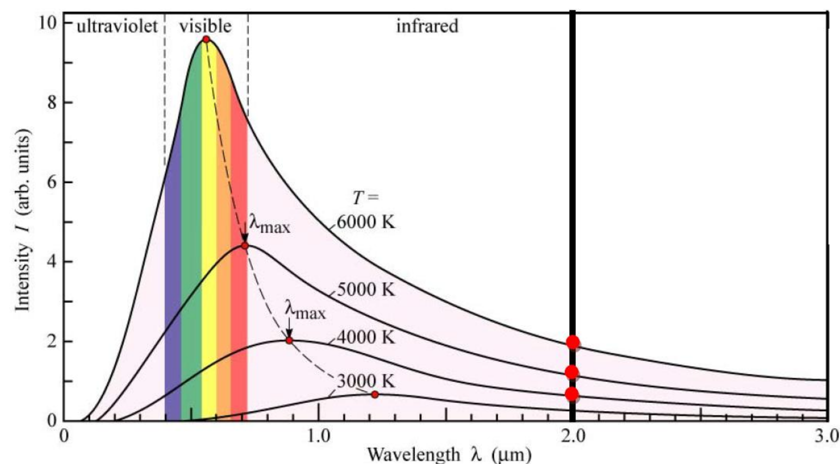

Fig. 3.3.2: Spectral energy as a function of wavelength.

A thermal imager makes use of Plank's law to measure the total radiance and integrate it with respect to wavelength to find the peak of the emission curve. When the camera detects a particular intensity of radiation, say one of the points circled in red in see Fig. 3.3.2, it associates that intensity with a particular temperature curve. If the camera detects an intensity of 2.0 (in arbitrary units displayed on the graph), and if the source is a black body, then the camera will match the curve to the 6000 K curve and

will report a temperature of 6000 K (roughly 5727° C). However, if the sample is not a black body, the camera will try to match the curve in accordance with the inputted emissivity value and generate the temperature value from the inbuilt look-up table. The thermal imager receives the radiance in the 8-14 μm spectral range, integrates the radiance, matches the curve and provides the measured temperature.

3.3.1 Calibration of thermal imager

The temperature measurements were taken using a thermal imager (*Testo-885*: spectral range of 8-14 μm) and its associated data acquisition software. The accuracy of the thermal imager is specified as ± 2% of measured values and the reproducibility is specified as ± 1% of measured value. The thermal imager is placed on a tripod to place the imager on the axis of the sample, and at a distance of about half a metre from the sample. The infrared radiation from the sample is received by the imager through a ZnSe window fitted to the barrel asher. The ZnSe window has a specified transmission efficiency *(T)* of about 70% in the 1-16 μm range, which covers the measurement range of the thermal imager (8-14μm.). Similar to the emission and Langmuir probe measurements, the temperature of the samples was measured after the sample reached a steady state in the plasma, at least 3 minutes after any change in conditions.

A black body source OL-480 (Optronic Laboratories) with an emissivity of 0.99 $\pm$ 0.01 was used to quantify the effects of the ZnSe window and to calibrate the thermal imager. The temperature of the black body source can be set independently and can be controlled in the range of 50-1200°C. The thermal imager was calibrated by measuring the temperature of the black body source and adjusting the value of emissivity to read

the same temperature as the black body source. With the emissivity value of 0.99 set in the thermal imager, maximum temperature variation between the thermal imager and the black body source was 2°C over the range of 300-800°C. Subsequently, the temperature of the black body source was measured through the ZnSe window to quantify its effect on thermal measurements. The emissivity value had to be reduced by 0.3 (that is, to 0.69) to read a true temperature of the black body source. This confirms that the ZnSe window has a transmission of 70% for thermal radiation as per the manufacturer's specifications.

3.3.2 Test sample calibration

The temperature errors due to transmission and reflection can be reduced by using a sample with high emissivity. We have used a coating liquid "Quartz Coat 845" (QC 845) to coat our fused quartz samples to achieve high emissivity. As per the manufacture's recommendations, the quartz coat was applied on the surface of the fused quartz and left tor air-dry for about 10 minutes. After 10 minutes, the test sample is further dried by placing it on a heating stage for 10 minutes at a temperature of 90 °C, followed by heating the sample to a temperature of 325 °C for 5 minutes. Fig. 3.3.3 shows the fused quartz sample before and after the application of *QC 845*.

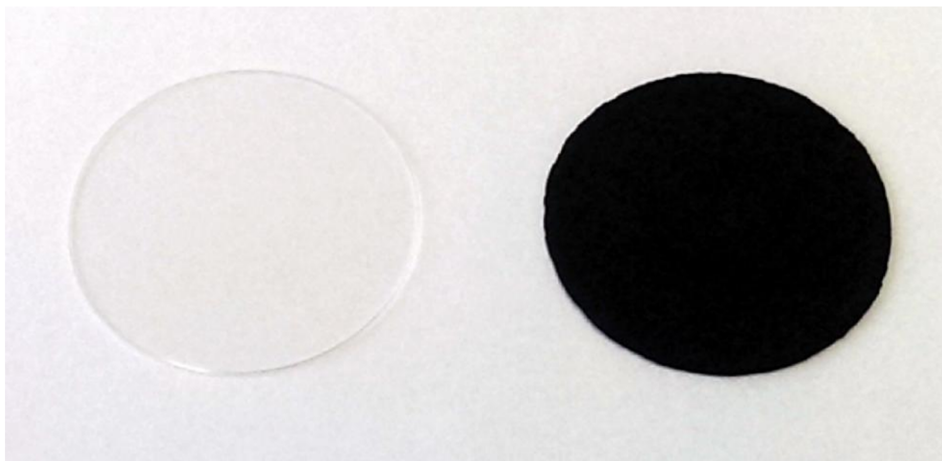

Fig. 3.3.3 Fused quartz sample (left) and QC845 coated fused quartz (right)

The conductivity of the QC 845 coated quartz sample was measured using a four-point probe resistance measurement. The QC845 coated quartz was found to be non-conducting. The emissivity of the coated sample was characterized by putting the sample in an furnance and measuring the sample temperature simultaneously using a thermocouple, and through the thermal imager and ZnSe window. The emissivity values in the imager were varied to read the same temperature as that given by the thermocouple. The temperature as measured using the thermal imager was found to be within 5 °C of the thermocouple measurement using an emissivity value of 0.69 (through the ZnSe window) in the temperature range of 300-800 °C. This indicates that the emissivity of the coating is ~0.99. Such a near ideal value implies that errors in temperature measurements due to reflections from the sample and transmission can be neglected.

We also examined the effect of absorption of radiation by the plasma on the temperature determined by the thermal imager. This was undertaken by placing the sample at different distances from the ZnSe window (and thermal imager) and measuring the sample temperature. Varying the distance from the ZnSe window (and

thermal imager) did not introduce variations in the values of the measured temperature determined by the thermal imager. We also observed the temperature change at the instant that the plasma was extinguished, and found no step change in the temperature measurement, which implies that the plasma itself does not contribute to significant absorption in the 8-14 μm spectral range.

Therefore, by using a high emissivity coating on our sample, we ensure that both the background reflections from the plasma and transmission through the plasma do not significantly contribute to errors in our temperature measurements. Further, we also ensured that the absorption of radiation by the plasma between the sample and the imager does not affect the thermal measurements.

3.4 Optical emission spectroscopy

A capacitively coupled plasma is generated between two electrodes, whereby the ionized atoms are brought to a high-energy state within so-called “discharge plasma”. These excited atoms and ions in the discharge plasma create a unique optical emission spectrum specific to the reactions involving the different species in the plasma (see Table 2.2.1 in Chapter 2). Thus, a single species can generate numerous characteristic emission spectral lines. The light emitted from the plasma contains information about the presence of various species in the plasma. The intensity of each emission spectrum is correlated to the relative concentration of the corresponding species in the plasma. An optical spectrum analyzer is used to capture the optical emissions from the plasma. We have measured the oxygen plasma emission spectra under different chamber conditions within the optical wavelength range from 200 nm to 800 nm.

3.4.1 OES experimental configuration

The optical emission measurements are captured by a Verity Instruments spectrometer (SD1024DF) with a wavelength resolution of 5nm across the range of 200nm to 800nm. The spectrometer is connected to a computer where the data is processed by using the SpectraView software. The set-up used for the measurements of optical emissions is shown in Fig. 3.4.1.

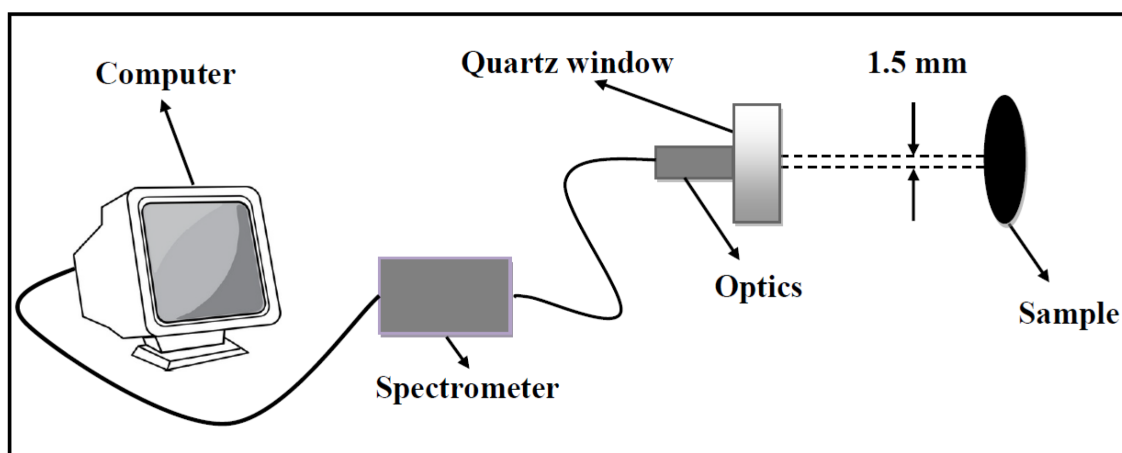

Fig. 3.4.1: Set-up for the optical emission measurements.

The plasma chamber has a removable port to which a high purity quartz window was attached to view the plasma. The quartz window is uniformly transparent across the 200nm to 800nm wavelength range. On the outside of the quartz window, collimating optics (also with uniform attenuation over the spectral range of interest) was used to collect light from a narrow field of view (1.5mm) at various points of interest on the sample. The collimating optics focuses the light onto a 0.2mm low loss uv enhanced optical fibre connected to the optical spectrum analyzer. A visible light source connected to the fibre was used to position the emission sampling point.

The emission measurements were taken 3 minutes after changing the conditions (power and pressure), as from observation it was noted that the magnitude of emissions reach a steady state within 3 minutes. All emission measurements were taken with the sample inside the plasma barrel asher.

3.5 Langmuir probes

The Langmuir probe, named after Nobel Prize winning physicist Irving Langmuir, is a metallic probe immersed in the plasma that can be used to determine the electron temperature, electron density, and electric potential of a plasma. In particular, the electron temperature can be determined via a single Langmuir probe by measuring the open circuit voltage due to the plasma. This voltage is also known as the floating voltage. The floating potential (V_f) is given by Equation 3.5.1 [61].

$$V_f = \frac{-kT_e}{e} ln \sqrt{\left(\frac{m_i}{4\pi m_e}\right)} \quad \textbf{3.5.1}$$

where,	m_i	=	mass of the ion
	m_e	=	mass of the electron
	$\frac{kT_e}{e}$	=	electron temperature (eV)
with,	k	=	Boltzmann constant
	T_e	=	electron temperature (Kelvin)
	e	=	elementary electric charge

Plasma temperature is commonly measured in electron volts and is indirectly a measure of the average thermal kinetic energy per particle. kT_e/e in Equation 3.5.1 represents the temperature (eV) of the electrons in the plasma and hence is a measure of the energy carried by electrons in the plasma.

3.5.1 Langmuir probe experimental configuration

The design of accurate Langmuir probes is non-trivial [62], and in our case it is complicated by the limited available physical access into the plasma chamber. In our set-up, the probe is introduced into the chamber through a gas inlet line. The gas inlet line is located at the top of the chamber and near to the top driven electrode. The probe wire is inserted into a 0.7mm hollow ceramic tube, which is shielded by a 1mm stainless steel hypodermic tube. The shield extends approximately 2cm into the gas feed line and away from the rf field due to the chamber electrodes. Inside the chamber, the shielded probe has two right angle bends on the chamber side of the gas feedline so that the probe end is extended along the central axis of the chamber. The active part of the probe extends 1cm beyond the shield in accordance with Ref. [62]. The schematic and image of the Langmuir probe is presented in Fig. 3.5.1.

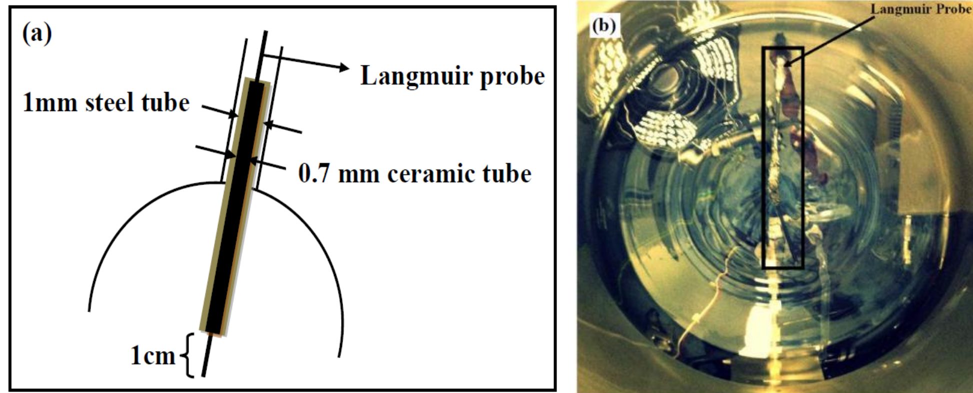

Fig. 3.5.1: (a) A schematic and (b) an image of Langmuir probe coming through the gas inlet and extending to the centre of the chamber.

The voltage on the probe is measured using an oscilloscope with a 1MΩ input impedance. The oscilloscope measurements indicate an rf component at 13.5MHz and since the magnitude of this rf component is not directly proportional to the rf power, we can conclude that unwanted capacitive coupling to the probe is negligible. However, interpretation of the Langmuir probe voltage where the rf is included is non-trivial [62], and the results are used as a guide only to the conditions inside the plasma. Note that the rf could be filtered using an active circuit, but is beyond the scope of this work. Similar to optical emission measurements, the Langmuir measurements were also taken in the steady state. The minimum of the 13.56 MHz voltage cycle was taken as the floating potential for our measurements. Using equation 3.5.1, and the mass of the O^+ ion, the electron temperature (eV) is related to the floating voltage (V_f) via:

$$\frac{kT_e}{e} = \frac{-V_f}{3.87} \quad \textbf{3.5.2}$$

3.6 Post-deposition heat treatment

The purpose of annealing amorphous garnet films of nominal composition $Bi_2Dy_1Fe_4Ga_1O_{12}$ is to crystallize them in order to develop appropriate magneto-optic properties. In addition to the plasma annealing, we have crystallized the films using both RTA and furnance. For furnance annealing, we used an in-house furnace with a quartz tube in an oxygen atmosphere. A barrel asher (PM-600, March Instruments) as described in Section 3.2 was used for plasma annealing. An AnnealSys As-one rapid thermal annealer (shown in Fig. 3.6.1) was also used in this study. The rapid thermal annealer uses an infrared source to generate rapid heating of the garnet sample and reduce the annealing time required for crystallization compared to furnance annealing.

Fig. 3.6.1: Rapid Thermal annealer (AnnealSys As-one).

3.7 X-ray diffraction

X-ray diffraction is based on observing the scattering intensity of an X-ray beam from a sample as a function of incident and scattered angle. In principle, any wave impinging on a regular array of scatterering sources produce diffraction. However, to

produce significant diffraction, the spacing between the scatterering sources and the wavelength of the impinging wave should be similar in size. X-rays are used to produce the diffraction pattern as their wavelength (1–100 angstroms) is typically similar to the spacing between atomic planes in the crystal. A diffraction pattern is basically obtained by measuring the intensity of diffracted waves from the sample as a function of scattering angle.

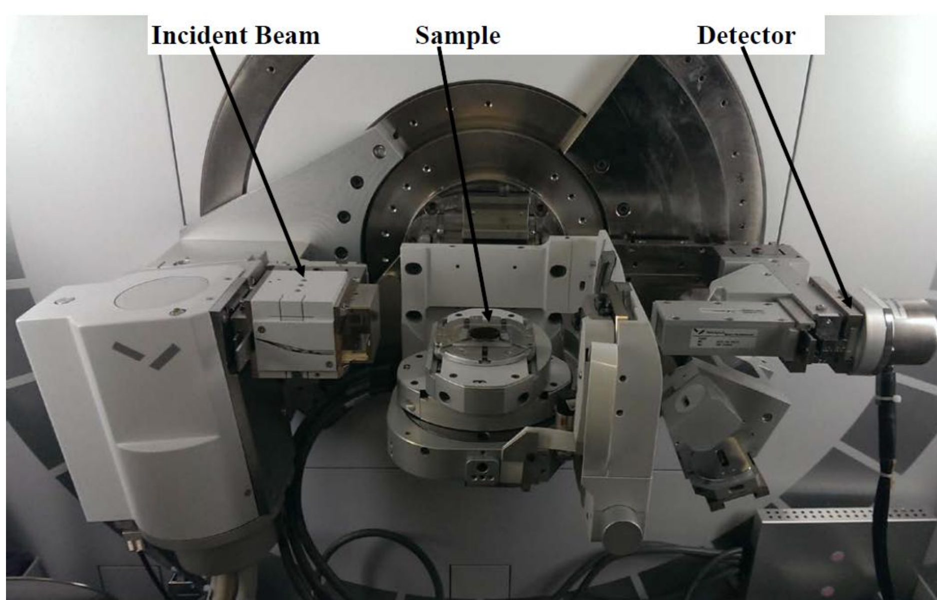

Fig. 3.7.1: Set-up for the X-ray diffraction.

The crystallization of the annealed films was determined using a Panalytical Empyrean XRD system (shown in Fig. 3.7.1) in the Centre for Microscopy, Characterization and Analysis (CMCA) at UWA. The XRD is equipped with a five axis sample stage (capable of moving in five directions). The instrument uses the Cu-Kα radiation with the wavelength of λ = 1.54056 A° for the kα1 line. The X-rays from the incident beam fall on the sample, get diffracted and are measured by the detector. The crystalline structure of the samples was evaluated by grazing incidence XRD with a fixed angle of 0.6 degrees between the X-ray incident beam and the film surface.

3.8 Faraday rotation and optical transmission

The Faraday effect or Faraday rotation is a magneto-optical phenomenon based on an interaction between light and the magnetic field in a dielectric or non-conducting medium. A magnetic field induces a rotation of the atomic magnetic dipoles in the dielectric, making it dielectrically polarized. This causes a beam of electromagnetic radiation entering the material to split into two beams due to the effect of double refraction, or circular birefringence. These beams propagate through the material at different speeds so that upon emerging from the material, they recombine with a phase shift that is expressed as a rotation in the polarization angle of the beam.

The Faraday effect in its most simple description is as follows: The polarization plane of linearly polarized light is rotated by an angle Θ when the light passes through a sample of thickness d, that is magnetized parallel to the direction of light propagation.

The angle of rotation can be expressed as:

$$\Theta = V*d*M \quad \textbf{3.8.1}$$

where,			
	Θ	=	angle of rotation (Degree)
	d	=	length of path (sample thickness: µm)
	V		Verdet’s constant
	M	=	magnetization (Tesla)

The Verdet’s constant is material specific and is a function of wavelength and temperature. The Faraday rotation in magnetic materials is defined by the saturation

magnetization (M), which for a garnet material is given by the vectorial sum of dodecahedral, octahedral, and tetrahedral sublattices. Therefore, the cations present on different sublattices affect the total saturation magnetization, which further affects the Faraday rotation.

3.8.1 Set-up for magneto-optical measurements

To analyze the magneto-optical properties, such as Faraday rotation and optical transmission, we have used an in-house magneto-optical spectrometer as schematically shown in Fig. 3.8.1.

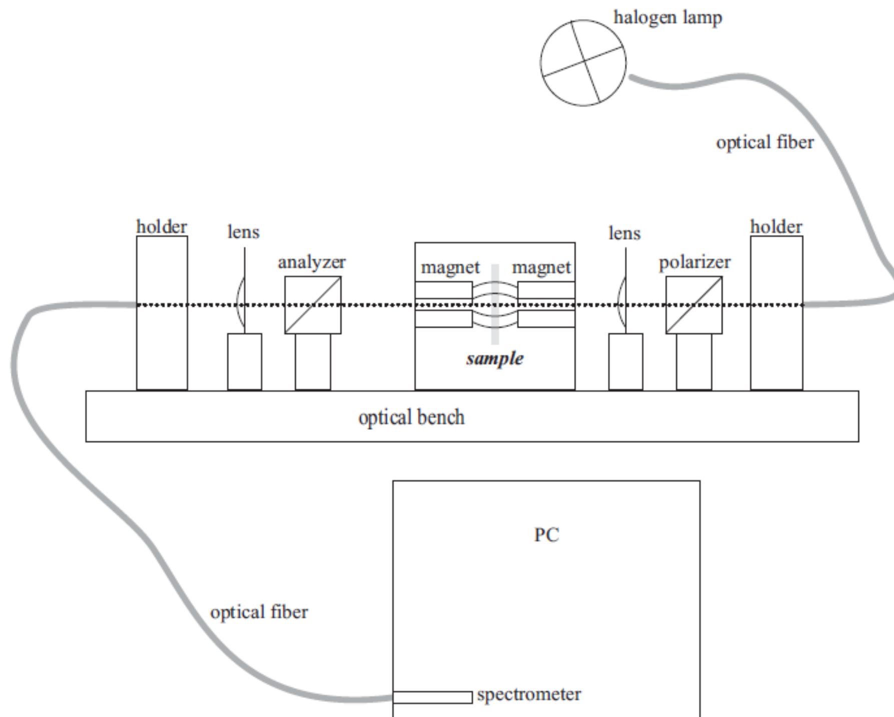

Fig. 3.8.1: Set-up to measure Faraday rotation and optical transmission[63].

Fig. 3.8.1 shows the set-up to measure Faraday rotation and optical transmission of the thin films in the wavelength range of 460-700 nm. In this device the light from a halogen lamp is passed through a collimating lens followed by a fixed polarizer and

then through the sample, which sits inside an electromagnet that generates a magnetic field of ±0.54 T. The collimated light beam then passes through a second polarizer, through the analyzer that is rotated with respect to the fixed polarizer, and then focused onto an optical fibre connected to a spectrometer that measures the signal intensity over a range of wavelengths [63]. The combination of halogen light source and spectrometer (Ocean Optics PC2000) allows the Faraday rotation to be determined as well as the transmittance as a function of wavelength. The optical transmission is a measure of the fraction of incident light (visible region: 400-700 nm) that passes through a sample. The spectrometer data is gathered through an USB device and is processed by a PC using software developed in Labview.

3.9 Atomic force microscopy

Atomic force microscopy (AFM) is a very high-resolution type of scanning probe microscopy, with demonstrated resolution on the order of fractions of a nanometer, more than 1000 times better than the optical diffraction limit. The AFM consists of a cantilever with a sharp tip (probe) at its end that is used to scan the specimen surface. When the tip is brought into proximity with a sample surface, forces between the tip and the sample lead to a deflection of the cantilever. This deflection is measured using a laser spot reflected from the top surface of the cantilever onto an array of photo diodes. The AFM can be operated in a number of modes, depending on the application. In general, possible imaging modes are divided into contact modes, non-contact modes or tapping (intermittent contact) modes, where the cantilever is vibrated. In contact mode, the force between the tip and the surface is kept constant during scanning by maintaining a constant deflection. In tapping mode, the cantilever is driven to oscillate

up and down at near its resonance frequency by a small piezoelectric element mounted in the AFM tip holder. We used a ‘Dimension 3000 Atomic Force Microscope’ from ‘Digital Instruments (now Bruker)’ as shown in Fig. 3.9.1.

Fig. 3.9.1: Atomic Force Microscope (Dimension 3000).

For our experiments, contact mode was not used to avoid the possibility of surface damage by the contact point. Silicon probes with a reflective coating of aluminum and with a tip radius of <10 nm were used for the AFM scanning. The measurements were performed at a resonant frequency of 300 KHz and the images were taken at a scan rate of 1 Hz.

3.10 Transmission electron microscopy

Transmission electron microscopy (TEM) is a technique whereby a beam of electrons is transmitted through an ultra-thin specimen. An image is formed from the interaction of the electrons transmitted through the specimen; the image is then magnified and focused onto an imaging device such as a CCD camera.

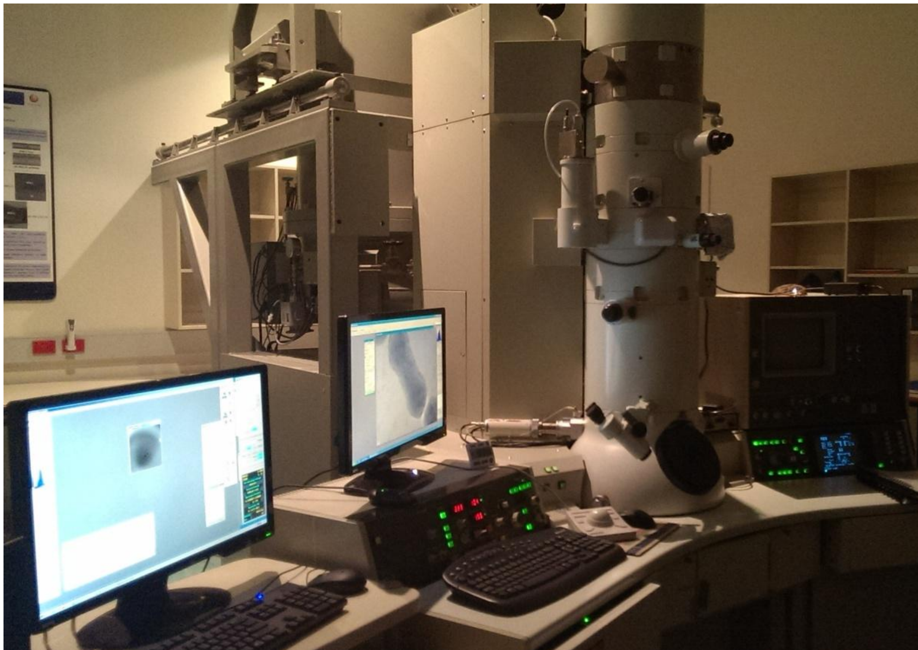

Fig. 3.10.1: Transmission electron microscope (JEOL 3000 F).

Fig. 3.10.1 shows the field emission transmission electron microscope (JEOL 3000 F) that was used in this study in the CMCA facility. It operates at a voltage of 100-300kV (usually operated at 300kV with an option to operate at 200kV) and takes cross-sectional images by using a 1 Mega pixel Gatan 694 MSC digital camera. The TEM samples were prepared using focused ion beam (FIB) methods at the University of New South Wales (UNSW).

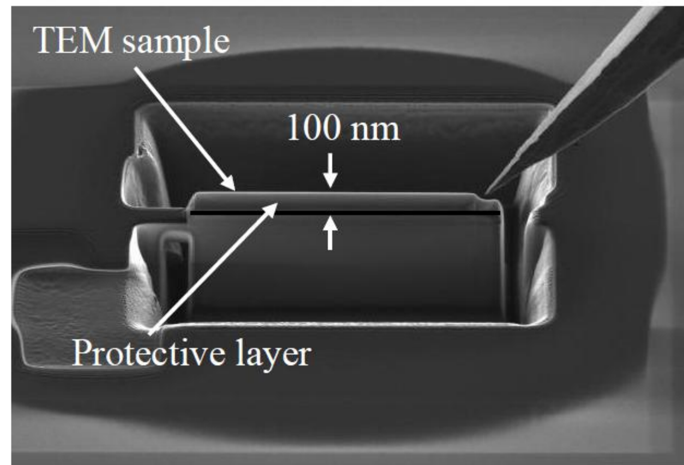

Fig. 3.10.2: TEM sample prepared via FIB method.

The TEM sample prepared via FIB method is shown in Fig. 3.10.2. During the preparation, the samples are coated with a gold layer in order to protect the surface of the samples from the ion beam. The samples are of order of the 100 nm thick to allow sufficient electron transmission through the samples. Thinner samples ensure good cross-sectional images and electron diffraction pattern. The diffraction pattern is recorded on the fluorescent screen and it provides information on the state (crystallized/amorphous) of the investigated material.

3.11 Electron probe micro analysis

Electron probe micro analysis (EPMA) is an analytical technique used to non-destructively determine the chemical composition of small volumes of solid materials. An electron microprobe operates using accelerated electrons focused onto a solid material. The incident electron beam has sufficient energy to liberate energy in the form of characteristic x-rays from the sample. X-rays are produced by inelastic collisions between incident electrons and the electrons in the inner shells of atoms in the sample. When an inner-shell electron is ejected from its orbit, leaving a vacancy, a higher-shell

electron falls into this vacancy and must shed some energy (in the form of a characteristic x-ray for that element) to do so. EPMA analysis is non-destructivesince the x-rays are generated by electron interactions and do not lead to volume loss of the sample, so it is possible to re-analyze the same material more than once. We used a Jeol 6400 SEM (a tungsten filament analytical scanning electron microscope) at CMCA to perform the analysis.

Fig. 3.11.1: Scanning electron microscope (Jeol 6400).

Fig. 3.11.1 shows the scanning electron microscope in the CMCA facility. It operates over a voltage range of 5-30kV. It is equipped with an Oxford Instruments Link Analytical Si (Li) EDS detector with Isis software to perform both qualitative and quantitative x-ray microanalysis. Before the analysis of our samples, we characterized the machine with standard samples from the CMCA facility. The garnet samples are coated with carbon to perform the EPMA.

3.12 X-ray photoelectron spectroscopy

X-ray photoelectron spectroscopy (XPS) is a semi-quantitative spectroscopic technique that can measure the elemental composition, empirical formula, chemical state and electronic state of elements that exist within a material. XPS spectra are obtained by irradiating a material with a beam of x-rays. When an x-ray photon hits and transfers this energy to a core-level electron, it is emitted from its initial state with a kinetic energy dependent on the incident x-ray and binding energy of the atomic orbital from which it originated. The kinetic energy and intensity of the emitted photoelectrons are analyzed to identify and determine the concentrations of the elements present. The XPS was performed by the Solid State & Elemental Analysis Unit at the University of New South Wales (UNSW). An Ar ion beam with an energy of 3keV was used to perform depth profiling. An ESCALAB 250Xi spectrometer (manufactured by Thermo scientific) was used for the quantitative characterization.

3.13 Summary

This chapter has presented the general background of the bismuth substituted iron garnet thin films used in this study, and the characterization methods required to investigate the plasma annealing process and the garnet films (both before and after annealing).

4

Plasma characterization

Radio frequency plasma treatments have been shown to reduce the thermal budget for the crystallization of TiO_2 and ITO films. Plasma gas pressure and rf power were found to be the key parameters in deciding the optimum crystallization conditions [22, 23]. Although crystallization was achieved at much lower temperatures in comparison to both RTA and furnance annealing for these materials, an accurate explanation of the dependence of crystallization on power and pressure in the plasma was not developed. In this chapter, we will examine the mechanisms involved in the oxygen plasma that can potentially affect the crystallization process. Traditionally, crystallization is strongly correlated to the processing temperature, so understanding the temperature of the sample achieved inside the plasma is critical to investigate the crystallization process. In addition, the plasma is potentially sensitive to the various atomic and ionic species within plasma. Hence, in order to characterize the crystallization conditions, we have to characterize the sample temperature and the various species within the plasma. The first section presents the characterization results of sample temperature, optical emission profile of O_2 plasma, and effects of backside conductor on both sample temperature and emission profiles. Discussion following in the last sections examine the relationship between the sample temperature and plasma species.

4.1 Sample temperature characterization

The crystallization of oxide films such as TiO_2 and ITO was achieved by Ohsaki *et al.* [22, 25, 26] at much lower temperatures (150 °C) in comparison to RTA and furnance treatments. They performed temperature measurements via a radiation thermometer (IT-540 N, Horiba Ltd) [25]. This is potentially not an accurate method of measuring the temperature as changes in the distance of the sample from the thermometer changes the spot size, which may affect the temperature measurements. Further, the issue of emissivity was not adequetly addressed in their work. This is an important parameter in the temperature measurement, since temperatures measured on low emissivity samples may be affected by the background plasma and other reflected heat sources, as described in Section 3.3. Furthermore, care needs to be taken that the view-port window into the plasma chamber is sufficiently transparent over the wavelength range being used by the thermometer.

As temperature is an integral part of every crystallization process, extreme care was taken in this thesis to thoroughly characterize the performance of the thermal imager, the view-port window and the test sample (see Section 3.3).

4.1.1 Test sample temperature variations

We used the thermal imager (as described in Chapter 3 in Section 3.3) to measure the temperature of fused quartz coated with a high emissivity coating (QC845) during exposure to plasma in the barrel asher. The temperature measurements were taken for rf

powers between 500-800 Watts and oxygen pressures between 2-5 Torr [2]. The thermal imager was set to an emissivity of 0.69 to match the measured emissivity of the QC 845 coating through the ZnSe window, hence the thermal images do not indicate the true temperature for surfaces not coated with this material, such as the sample holder. As shown in Fig. 4.1.1 the temperature on the QC845 coated fused quartz is non-uniformly distributed across the surface.

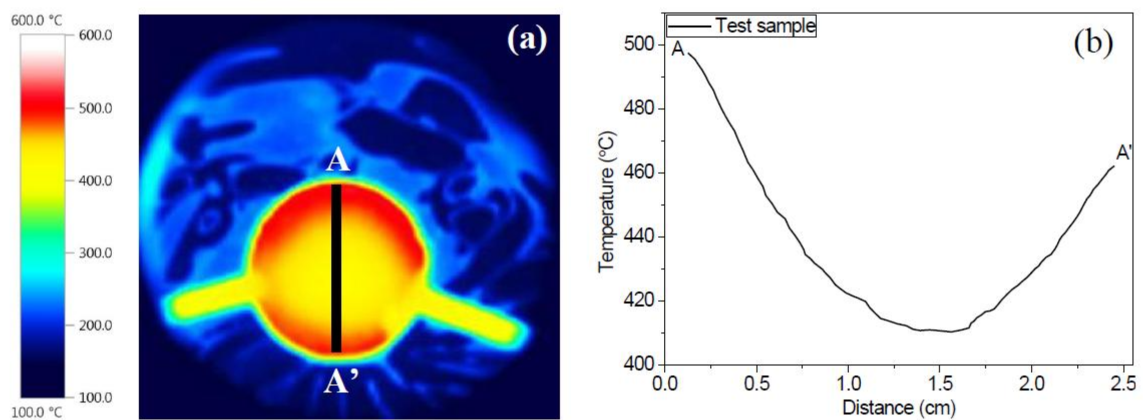

Fig. 4.1.1: (a) Thermal image and (b) top-to-bottom temperature line scan of a QC845 coated quartz sample in oxygen plasma in the barrel asher under rf power of 800 Watts and 3 Torr pressure.

Fig. 4.1.1 shows temperature variations of the coated quartz sample for a power of 800 Watts and pressure of 3 Torr. Fig. 4.1.1 (a) shows thermal image of the test sample, while Fig. 4.1.1 (b) shows top-to-bottom the temperature line scan from point A to A'. It can be seen from Fig. 4.1.1 (b) that the temperature of coated quartz sample is greater at the edges (A & A') of the sample as compared to the middle of the sample. The top of the sample (edge A) is also about 38 °C hotter than the bottom (edge A'). A similar trend in temperature variation was observed for other power and pressure conditions.

[2] Temperature measurements of test sample in nitrogen are presented in Appendix II.

To compare the temperature variations as a function of rf power and pressure, we took the peak sample temperature from the top edge of the sample and plotted it in Fig. 4.1.2.

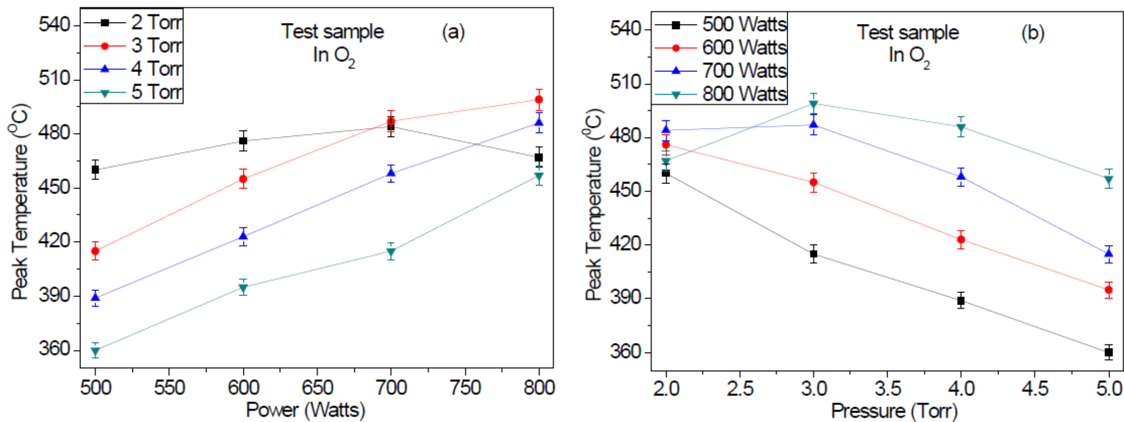

Fig. 4.1.2: Variation in the peak sample temperature of a QC845 coated quartz sample as a function of (a) rf power, and (b) chamber pressure. Error bars represent the relative standard deviation of 1.35 % for separate measurements.

Fig. 4.1.2 (a) shows the peak sample temperature as a function of power for different settings of pressure, while Fig. 4.1.2 (b) shows the same data replotted as a function of pressure for the different powers. It can be observed from the plots that although generally the temperature increases with increasing rf power and decreases with increasing pressure, there is no consistent correlation between temperature and either pressure or power. It is to be noted that the temperature of the QC845 coated quartz sample is in the range of 350-500 °C, which is much greater than the temperature reported by Ohsaki *et al.* [22] where the maximum temperature observed was 250 °C under similar experimental conditions.

4.1.2 Effects of conductor on thermal variations

It was shown by Ohsaki *et al.* [25] that placing a conductor behind and in thermal contact with the sample enhanced thin film crystallization. Therefore, a gold foil of thickness 0.15 mm was placed in thermal contact with the backside of the QC845 coated quartz sample to examine and gauge the effects of the conductor on the test sample temperature. The results are presented in Fig. 4.1.3.

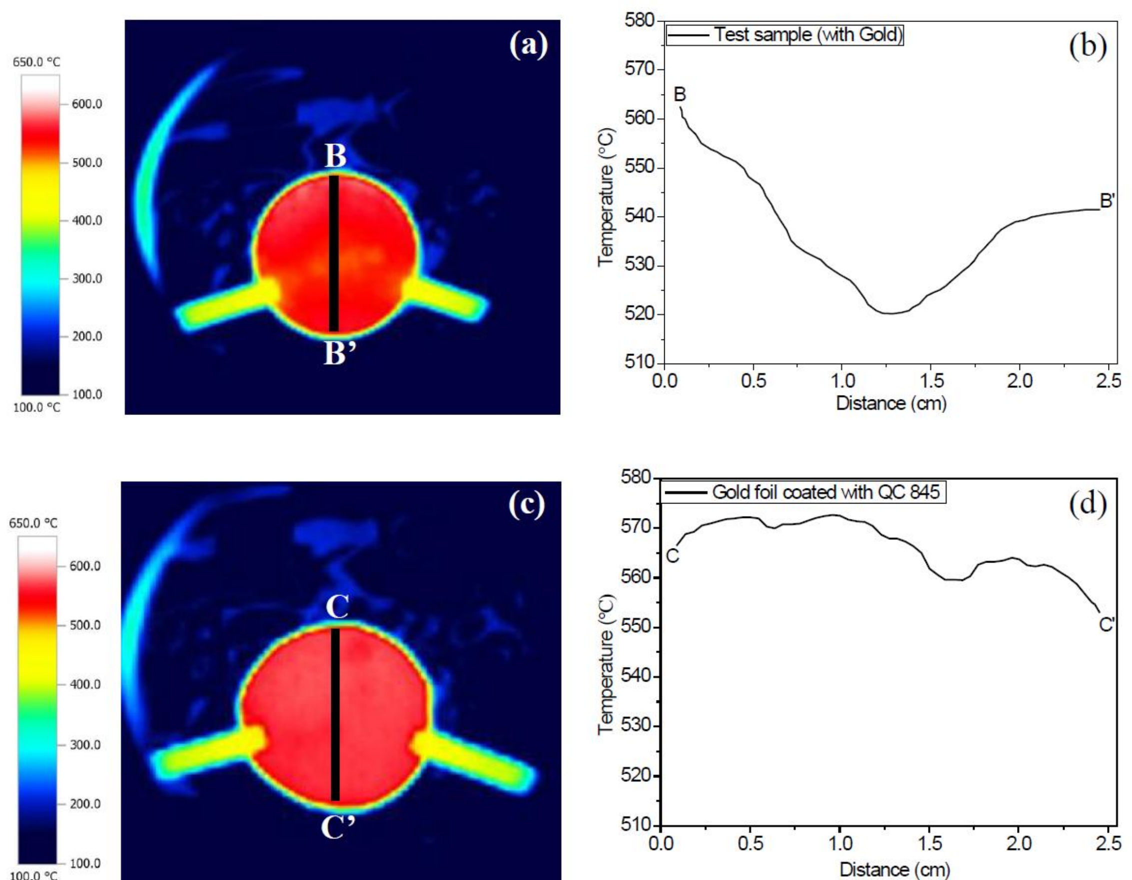

Fig. 4.1.3: (a) Thermal image QC845 coated quartz sample with Au foil and (c) thermal image of Au foil coated with QC 845. (b) & (d) top-to-bottom temperature line scan of QC845 coated quartz sample with Au foil and QC 845 coated gold foil, respectively.

Fig. 4.1.3 shows the thermal image and temperature variations of the QC845 coated quartz sample (with Au foil at backside) and a piece of gold foil of the same geometry

as the quartz sample where the gold was coated directly with QC845. These measurements were obtained for the chamber conditions of 800 Watts and 3 Torr. It can be observed from Fig. 4.1.3 (b) that the overall temperature of the test sample has increased as a result of placing a conductor behind and in thermal contact with the sample. Further, it can be seen from Fig. 4.1.3 (b) that the temperature difference between top and the bottom of the coated quartz sample with the gold foil behind it (B and B') has reduced by about 23 °C. This is significantly less than the difference between the temperature at top and bottom observed in Fig. 4.1.1 (b) for the same sample without the gold foil (38 °C). The QC845 coated gold foil shows an even smaller difference of about 15 °C between the top and bottom edge (Fig. 4.1.3 (d)). A similar behavior is seen in the temperature difference between the top edge and the middle of sample with the coated quartz sample having a difference of 90 °C, but this is reduced to about 43 °C and 15 °C for a coated quartz sample in thermal contact with gold and for the QC845 coated gold foil, respectively.

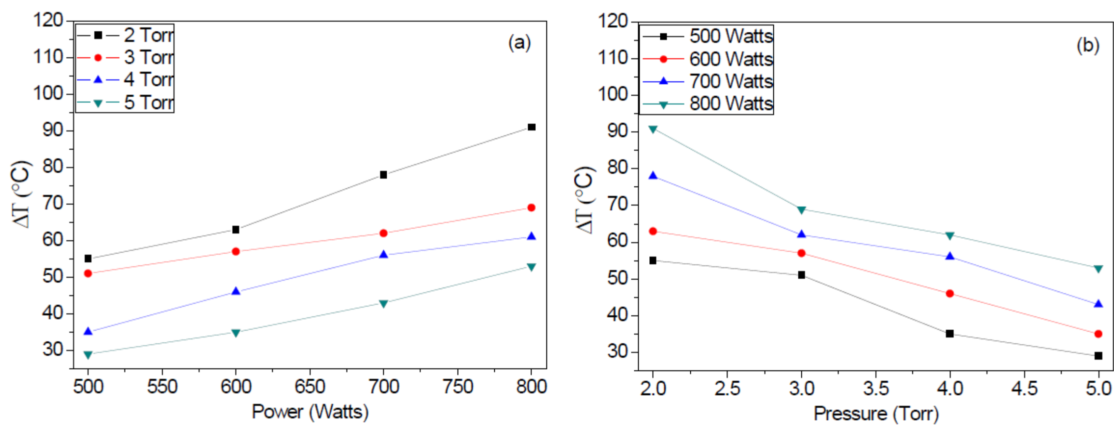

Fig. 4.1.4: Temperature difference (ΔT) of the QC845 coated quartz sample with and without Au foil placed behind it as a function of (a) rf power (b) pressure.

Fig. 4.1.4 (a) shows the ΔT as a function rf power for different pressures and Fig. 4.1.4 (b) re-plots ΔT as a function of pressure for different rf powers. Where, T_{Au} is the temperature of QC845 coated quartz sample with Au foil (°C)[3] and $T_{No\ Au}$ is the temperature of QC845 coated quartz sample without Au foil (°C). ΔT is the difference between the sample with and without a gold foil behind it.

$$\Delta T = T_{Au} - T_{No\ Au} \qquad \textbf{4.1.1}$$

ΔT is always positive indicating that the temperature of the test sample is always higher when a conductor is introduced in thermal contact with the backside of the sample. In addition, it can be seen that ΔT. monotonically increases with increasing power and monotonically decreases with increasing pressure for a fixed power.

4.1.3 Temperature dependence on conductor geometry

We have seen in the previous section that placing a gold behind the sample has increased the temperature of the sample when exposed to the plasma. It is believed that the temperature of the test sample is increasing as a result of thermal contact between the conductor and the test sample. In order to prove this hypothesis, we deposited a gold strip of 600 nm thickness and of 4 mm width across the backside of the sample (as shown in Fig. 4.1.5) and measured the temperature spatial distribution (see Fig. 4.1.6).

[3] Temperature of the QC845 coated quartz sample (with Au foil) is presented in Appendix II.

Fig. 4.1.5: Gold strip deposited across the middle of the QC845 coated quartz sample.

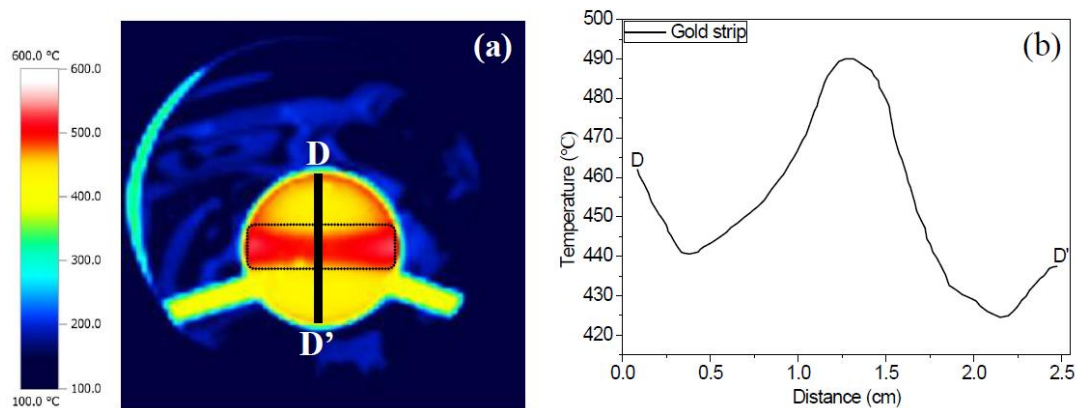

Fig. 4.1.6: (a) Thermal image and (b) top-to-bottom temperature line scan of deposited Au strip in an oxygen plasma under rf power of 800 Watts and 3 Torr.

Fig. 4.1.6 (a) shows the thermal image of the coated quartz sample with a gold strip that is 600 nm thick and 4 mm wide deposited on the backside of the sample. Fig. 4.1.6 (b) shows the top-to-bottom line scan of temperature variations of the sample from point D to point D'. It can be seen from Fig. 4.1.6 (b) that the temperature at the middle of sample is greater than the temperature at the edges of the sample.

Further, in order to investigate the relative effects of difference between distance from the electrodes (i.e. top or bottom of sample) and presence/absence of conductive film, we deposited 600 nm of Au on half of a QC845 coated quartz sample as shown in Fig. 4.1.7, and observed the temperature profile generated in the plasma (see Fig. 4.1.8).

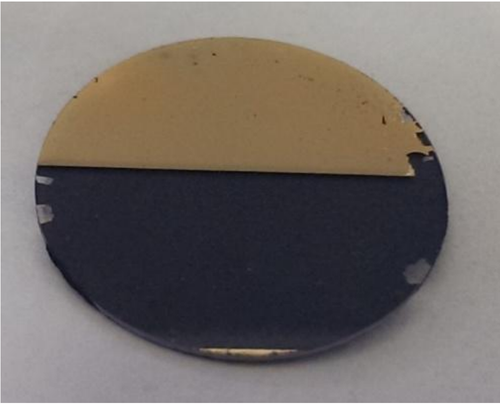

Fig. 4.1.7: Deposited gold on half the test sample.

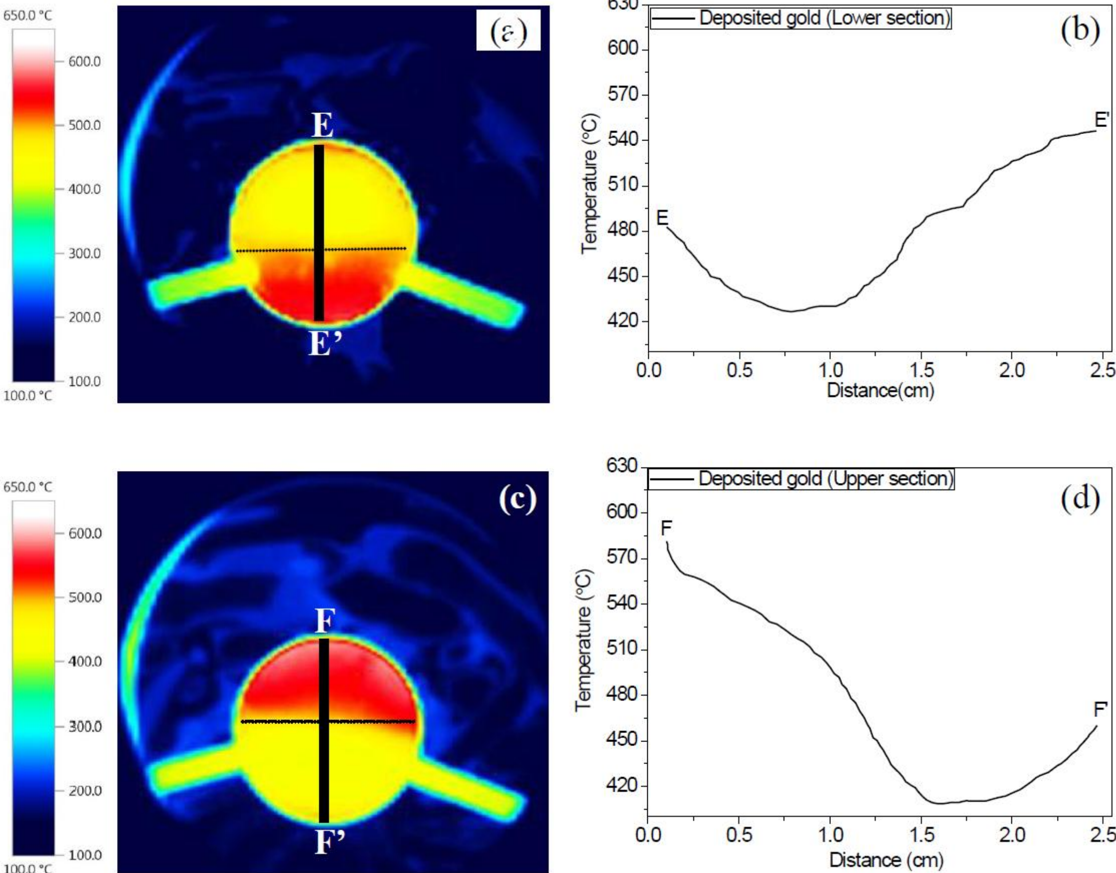

Fig. 4.1.8: (a) & (c) Thermal images and (b) & (d) top-to-bottom temperature line scans of half deposited test sample in an oxygen plasma chamber under rf power of 800 Watts and 3 Torr.

Fig. 4.1.8 (a) shows a thermal image for the sample with the deposited gold side positioned towards the bottom electrode and Fig. 4.1.8 (c) shows a thermal image with the gold side positioned towards the upper electrode. Fig. 4.1.8 (b) & (d) shows the top-

to-bottom temperature line scan across the sample for these two orientations of the conductor. It can be observed from Fig. 4.1.8 (b) that the maximum temperature (at E') is about 546 °C, while the maximum temperature in Fig. 4.1.8 (d) is about 581 °C (at F). This shows that temperature difference between points E' and F is approximately 35 °C.

Finally, we fabricated a fused quartz sample such that the top and bottom edge were equidistant from the upper and lower electrode (10.5 cm). In this case, a 600nm thickness of gold was deposited on both top and bottom sections of the sample, and the quartz was coated with *QC-845* on the front side. The sample is shown in Fig. 4.1.9, and thermal measurements are presented in Fig. 4.1.10.

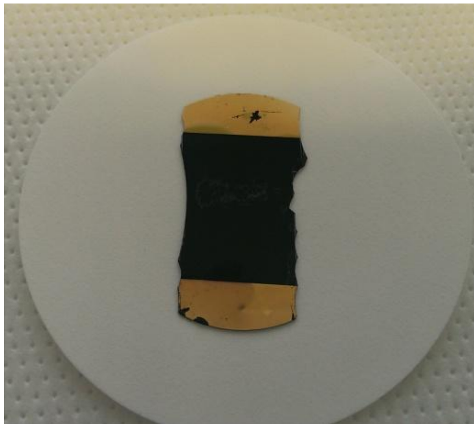

Fig. 4.1.9: Image of symmetrical sample.

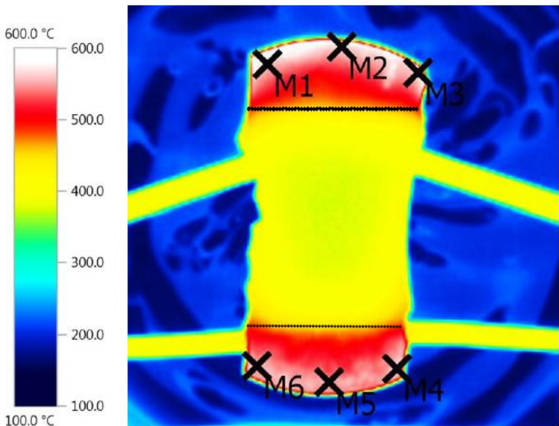

No.	Temp. [°C]
M1	582.1
M2	584.9
M3	583.7
M4	578.1
M5	576.7
M6	573.1

Fig. 4.1.10: Symmetrical sample at a pressure and power of 3 Torr and 800 Watts, respectively.

Fig. 4.1.10 shows the thermal image of the symmetrical sample at an rf power of 800 Watts and pressure of 3 Torr. It can be seen from Fig. 4.1.10 and its associated table that the temperatures at both the top and bottom edges are very close to each other. An average difference in the temperature of the top and bottom edge has been reduced to below 10 °C, in comparison to the temperature difference of about 38 °C in Fig. 4.1.1 (b), 23 °C in Fig. 4.1.3 (b), and 15 °C in Fig. 4.1.3 (d)

4.1.4 Temperature variations due to different conductors

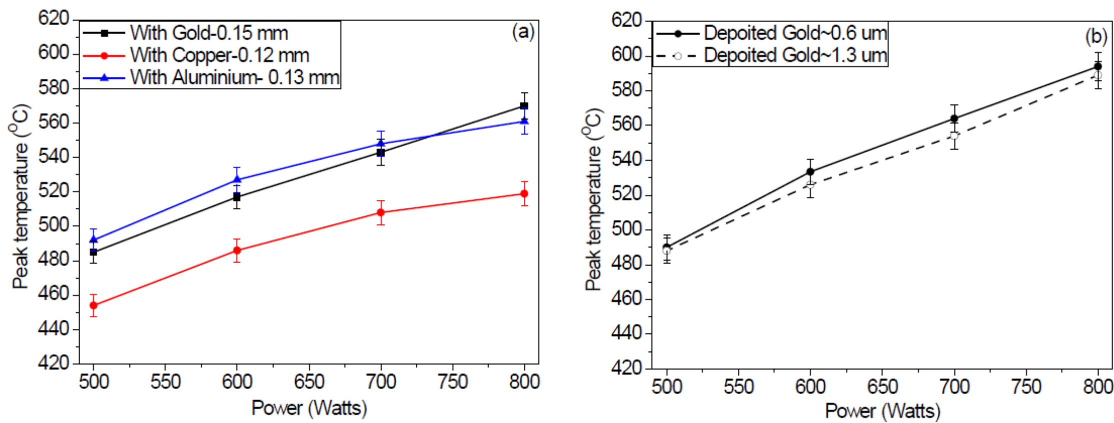

Fig. 4.1.11: Peak temperature of the test sample (a) with gold, copper and aluminum foil in thermal contact with the backside of the sample, and (b) with deposited gold of thickness of 0.6 and 1.3 µm. Error bars represent the relative standard deviation of 1.35 % for separate measurements.

Fig. 4.1.11 (a) shows the peak temperature of QC845 coated quartz samples with gold, aluminum, and copper foil in thermal contact with the backside of the sample, as a function of rf power for a chamber pressure of 3 Torr. Fig. 4.1.11 (b) shows the peak temperature of coated quartz samples (on which two different thicknesses of gold have been deposited on the backside) as a function of rf power for a chamber pressure of 3 Torr. It can be observed from Fig. 4.1.11 (a) that the temperature of coated quartz sample in thermal contact with gold and aluminum is similar to each other and is higher than the temperature of a coated quartz sample in thermal contact with copper. It can also be seen from Fig. 4.1.11 (b) that the temperature distributions for both backside-gold-deposited samples (0.6 µm and 1.3 µm thick) are similar within experimental error. It should be noted that the temperature of test samples with deposited gold is slightly higher than the temperature of the test sample in thermal contact with gold foil.

4.2 Optical emission characterization

The plasma annealing conditions for crystallization have been shown to vary with respect to the gas pressure and rf power [22]. In addition, plasma-treatment has been shown to crystallize materials at low temperatures. This suggests that the temperature is not the only factor that is affecting the crystallization process. Further, we have seen in Section 4 that the temperature does not correlate well with rf power and plasma gas pressure. Therefore, in order to investigate the effects of plasma species on heating mechanisms and crystallization conditions, we need to understand how the plasma composition and species vary with rf power and pressure conditions. To gain such an understanding, we have used optical emission spectroscopy[4] and Langmuir probes.

The optical emission of an oxygen plasma was characterized for powers of 500-800 Watts and pressures of 2-5 Torr, similar to the values used for the sample temperature characterization in Section 4. The optical emission spectrum in the 200-800nm wavelength range using oxygen gas yields a spectrum that appears to almost exclusively consist of singly ionised oxygen (O^+) and atomic oxygen (O) lines.

[4] Optical emission spectra in the range of 200-800nm for Nitrogen is presented in Appendix II.

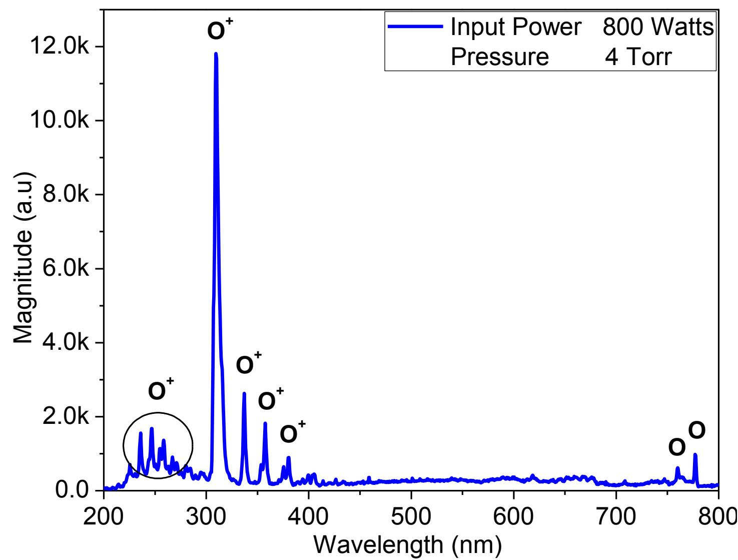

Fig. 4.2.1: Optical emission spectrum of oxygen plasma at a power of 800 Watts and pressure of 4 Torr.

Fig. 4.2.1 shows the optical emission spectrum of oxygen for an rf power of 800 Watts and a pressure of 4 Torr. The presence of O^+ is represented by emission lines at wavelengths of 235.5, 246, 254.5, 310, 337, 358, 380, 404 nm [41] and O at wavelengths of 760 nm and 777 nm [40]. Even though several O^+ and O emission lines are present in the spectrum, not all of them were found to be helpful in characterizing the plasma species with changing plasma conditions. Fig. 4.2.2 shows the emission spectra of O^+ lines in the range of 300-360 nm and O lines in the range of 740-800 nm with increase in rf power from 700 to 800 Watts and at a pressure of 4 Torr. It is evident from the figure that some emission lines do not vary significantly, as the power is changed from 700 to 800 Watts.

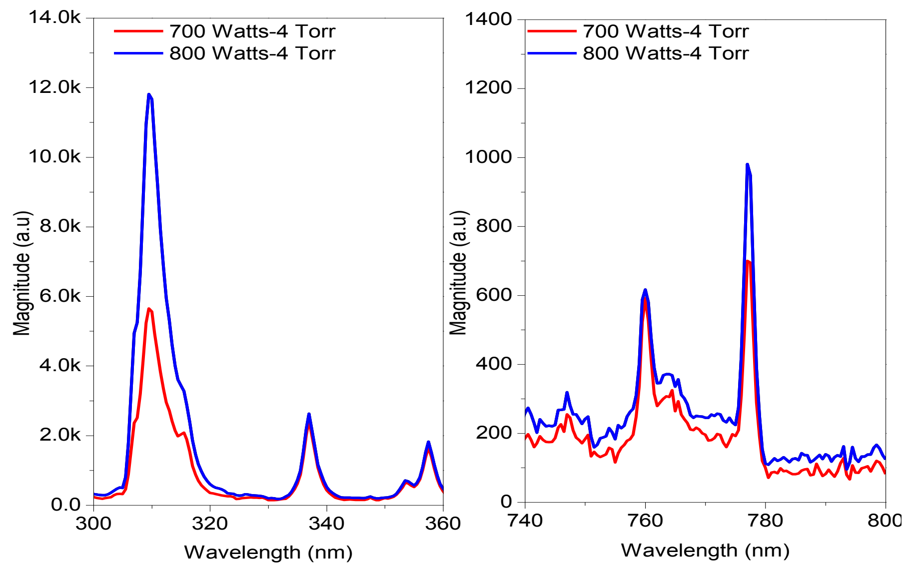

Fig. 4.2.2: Emission spectra of oxygen for rf powers of 700 and 800 Watts at a pressure 4 Torr.

It can be observed from Fig. 4.2.2 that with an increase in power, only the emissions of O^+ at 310 nm and of O at 777 nm vary significantly. We have seen this behavior for all other chamber conditions. Therefore, we have chosen the lines at 310 nm and 777 nm for the optical characterization of the plasma. The peak intensity values are taken as the magnitudes of O^+ and O emission lines.

4.2.1 Variations in atomic oxygen emission line

The variation of the magnitude of the atomic oxygen (O) emission line at 777 nm with changing rf power and pressure is presented in Fig. 4.2.3.

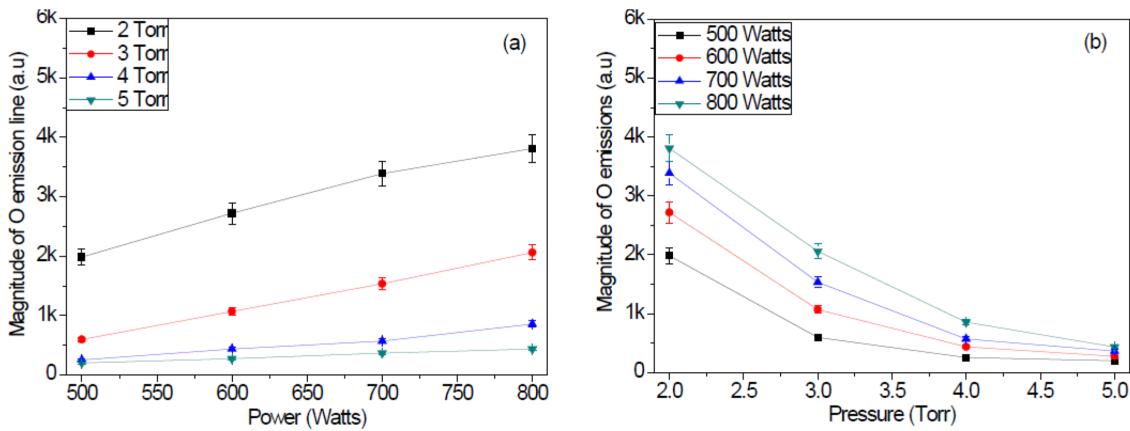

Fig. 4.2.3: Magnitude of atomic oxygen (O) emission line as a function of (a) rf power, and (b) pressure. Error bars represent the relative standard deviation of 5.3 % for separate measurements.

Fig. 4.2.3 (a) shows the magnitude of the 777 nm emission line of atomic oxygen as a function of rf power for various pressures, while Fig. 4.2.3 (b) re-plots the data as a function of pressure for various rf powers. The magnitude of the 777 nm atomic oxygen emission line is positively correlated with the rf power and is negatively correlated with pressure.

4.2.2 Variations in singly ionised atomic oxygen emission line

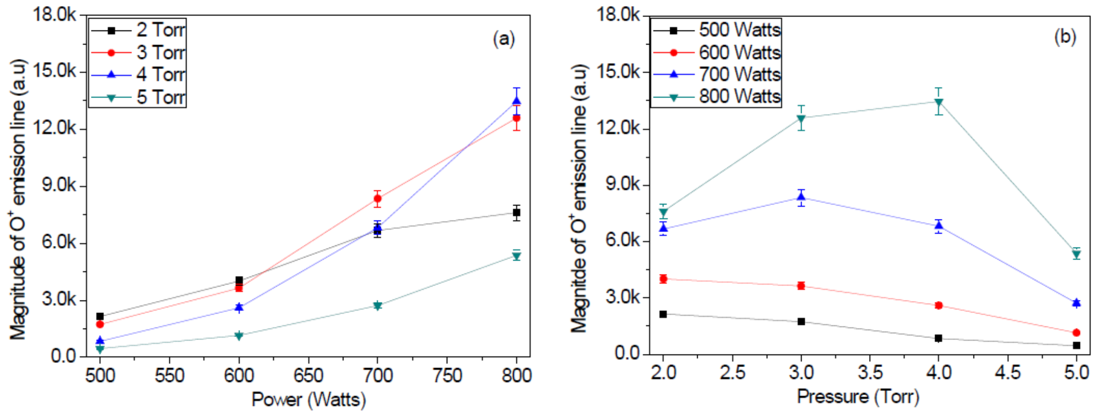

Fig. 4.2.4: Magnitude of singly ionised atomic oxygen (O^+) emission line with respect to (a) rf power, and (b) pressure. Error bars represent the relative standard deviation of 5.3 % for separate measurements.

Fig. 4.2.4 (a) shows the magnitude of the O^+ emission line at 310 nm as a function of rf power for various pressures of oxygen, while Fig. 4.2.4 (b) re-plots the data as a function of pressure for various powers. In general, it is observed that the magnitude of O^+ emission line tends to increase with rf power and decrease with increasing pressure. However, we see two exceptions to the above:

- In Fig. 4.2.4 (a) for a pressure of 2 Torr, the magnitude of O^+ emission line increases with increasing power until 700 Watts and subsequently starts to saturate.

- In Fig. 4.2.4 (b), the general negative correlation between the magnitude of the emission line and pressure was observed in the case of O for powers at and below 600 Watts. For 700 Watts, the magnitude of O emission line increases as the pressure increases from 2 to 3 Torr and then starts decreasing with further increase in pressure. This behavior is clearer when the rf power is increased to

800 Watts. In that case, the magnitude increases until 4 Torr and starts decreasing with further increase in pressure.

4.2.3 Langmuir probe measurements

The optical emission results show the presence of O^+ and O in the range of power and pressures investigated here. From Chapter 2 (See Table 2.2.1), it is clear that the generation of these species requires certain threshold energies. Therefore, we used a Langmuir probe, as described in Section 3.5 to estimate the electron energies. The voltages measured via Langmuir probe were negative under all conditions indicating that the electrons within the plasma surround the probe. The resulting electron temperature (eV) was derived from Equation 3.5.2 and the results are presented in Fig. 4.2.5.

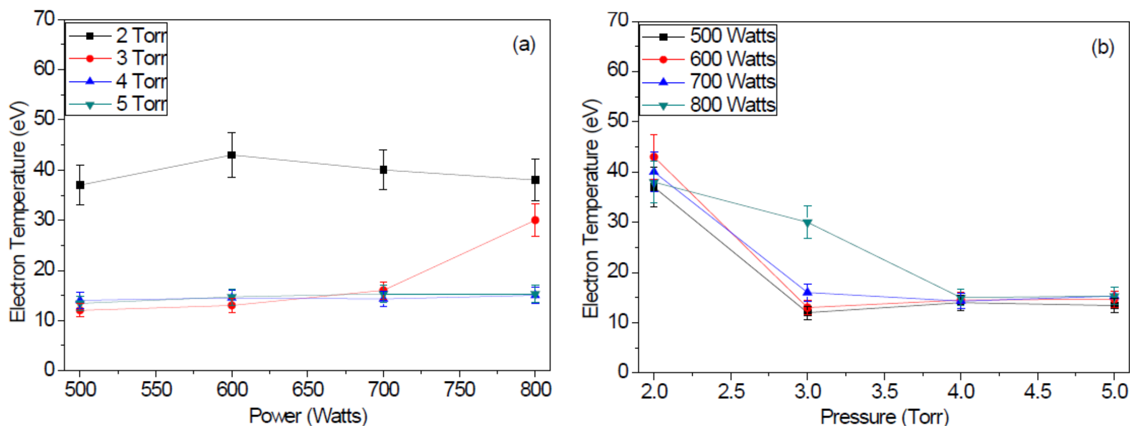

Fig. 4.2.5: Electron temperature as a function of (a) rf power, and (b) pressure.

Fig. 4.2.5 (a) shows the electron temperature as a function of rf power for various pressures. Fig. 4.2.5 (b) re-plots the data as a function of pressure for various powers. It can be seen from Fig. 4.2.5 (a) & (b) that the electron temperature at 4 and 5 Torr does not vary with increase in power. When the pressure is reduced to 3 Torr, the electron

temperature increases abruptly from about 15 to 30 eV as the power increases from 700 to 800 Watts. With an additional decrease in pressure to 2 Torr, the electron temperature increases to about 35 eV irrespective of rf power. It can be observed from Fig. 4.2.5 (a) that even at an rf power of 500 Watts (at 2 Torr), the electron temperature is greater than the electron temperature generated by 800 Watts at pressures of 3, 4 and 5 Torr.

4.2.4 Comparison of O^+ and O emissions (with and without gold)

A gold foil (electrical conductor) of 0.15 mm in thickness was placed behind and in thermal contact with the test sample (electrically insulating) to gauge the effects of gold on the emission lines. The sample (without gold) is the QC845 coated quartz sample alone.

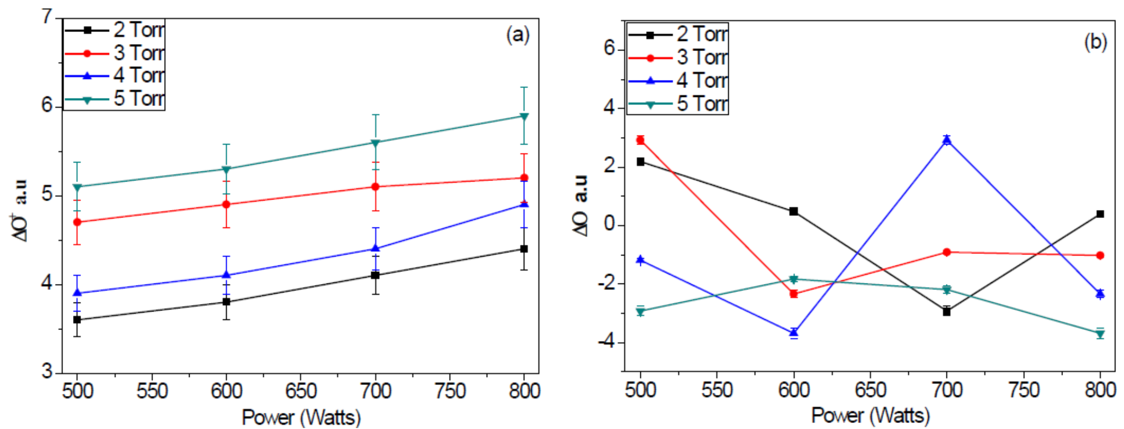

Fig. 4.2.6: Percentage difference in the magnitude of emission with and without Au foil with respect to rf power for (a) ΔO^+, and (b) ΔO, error bars represent the relative standard deviation of 5.3 % for separate measurements.

$$\Delta O^+ = \left(\frac{[O^+]No\ Au - [O^+]Au}{[O^+]No\ Au}\right)*100 \qquad \textbf{4.2.1}$$

$$\Delta O = \left(\frac{[O]No\ Au - [O]Au}{[O]No\ Au}\right)*100 \qquad \textbf{4.2.2}$$

where, $O^+_{No\ Au}$ = O^+ emission line magnitude without gold foil.

O^+_{Au} = O^+ emission line magnitude with gold foil.

$O_{No\ Au}$ = O emission line magnitude without gold foil.

O_{Au} = O emission line magnitude with gold foil.

The ΔO^+ (Fig. 4.2.6 (a)) and ΔO (Fig. 4.2.6 (b)) are shown as a function of rf power for the pressures of 2, 3, 4 and 5 Torr. Fig. 4.2.6 (a) shows that ΔO^+ is always positive meaning that the O^+ emission without Au is always greater than the magnitude of O^+ emissions with Au. It can be observed that ΔO^+ increases only slightly (for a particular pressure) with increasing power, and also increases slightly with pressure. The ΔO, on the other hand, varies randomly around an average of nearly zero indicating that the presence of gold does not significantly affect the magnitude of O emissions.

4.2.5 Sample temperature as a function of emission magnitudes of O^+ and O

In the earlier sections of this chapter, we had observed that the sample temperature and optical emission magnitude of O^+ do not correlate well with the rf power and pressure. We attempted to correlate the sample temperature with the magnitude of O^+ emission line but no clear relationship was observed. However, when the magnitude of the O emission line was considered along with O^+ emission line magnitude, we found a relationship as presented in Fig. 4.2.7.

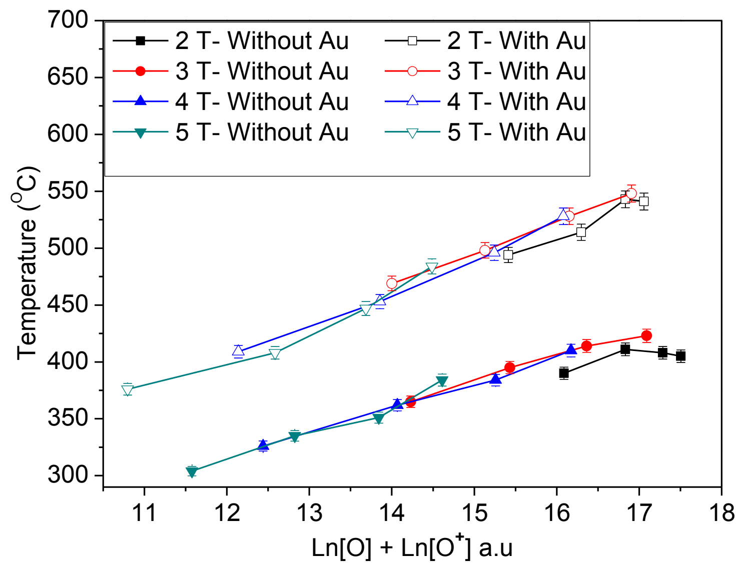

Fig. 4.2.7: Temperature as a function of emission magnitude of O and O^+.

It can be seen from Fig. 4.2.7 that the temperature of the QC845 coated quartz sample (with and without back-side Au) is a linear function of the summation of ln (emission magnitude of O) and ln (emission magnitude of O^+). It is to be noted that a similar linear behavior with nearly identical slope is obtained with the gold foil placed behind the sample but with the two lines offset from each other. For the same values of ln (O) and ln (O^+), the temperature of QC845 coated sample with back-side gold is greater than the temperature of the sample without back-side gold.

4.3 Ionization and diffusion as a function of rf power and pressure

Two processes are occurring simultaneously within the plasma: ionization and diffusion. Ionization in the oxygen plasma refers to the generation of singly ionised oxygen atoms (O^+) either from atomic oxygen or directly via an oxygen molecule. Diffusion, on the other hand, is defined as the flow of charges (ions or electrons) from the bulk plasma to the electrodes (See Chapter 2).

To understand the concept of ionization and diffusion in capacitively coupled plasmas, we must first discuss the influencing factors. The amount of ionization and diffusion is dependent upon the electron energy, the high-energy electron density, and the mean free path of both electrons and positive ions.

The electron energy is positively correlated to rf power and is negatively correlated to chamber pressure (see Section 2.6 in Chapter 2). This behavior is reflected in the trends observed in the magnitude of the O emission line in Fig. 4.2.3. However, the magnitude of the O^+ emission line shows different trends (See Fig. 4.2.4) compared to the trends observed for the magnitude of the atomic oxygen emission line (See Fig. 4.2.3). This behavior may be explained by the diffusion tendency of electrons and O^+ ions at low pressures, combined with the dependence of the density of highly energetic electrons on rf power.

Diffusion in a capacitively coupled plasma occurs primarily due to two factors: namely; mean free path and sheath-negative charge layer electrostatic potential. The barrel asher is a constant volume chamber and the pressure can only be increased by introducing more oxygen in the chamber. The mean free path is negatively correlated to pressure as an increase in pressure increases the number of particles in the chamber. This increase in particle density results in more collisions, which results in a reduction of the mean free path. The sheath-negative charge layer electrostatic potential attracts the positively charged ions toward the electrodes and away from the bulk (see Section 2.3 in Chapter 2). In this way, the positive ions diffuse to the electrodes, and the density of positive ions is reduced in the bulk.

When we increase the rf power while keeping the pressure constant, the electron energy increases. The degree of ionization is positively correlated to the energy of electrons in the chamber. Therefore, an increase in electron energy increases the probability of ionization. The energy of the electrons keeps increasing with increasing rf power until the electrons possess enough energy to overcome the electrostatic potential barrier. Once the electrons have enough energy, they start diffusing to the electrodes. This means that even though the electrons have more energy, the ionization reduces because of the diffusion of energetic electrons. This could be associated with decrease in the O^+ emission line magnitude with increasing rf power above 700 Watts at a pressure of 2 Torr (see Fig. 4.2.4 (a)). The sheath-negative charge electrostatic potential aids the diffusion process by attracting positive ions towards the electrode. This diffusion process is more predominant at low pressures, where the mean free path of positive ions is long and thus the ions have a higher tendency to diffuse to the electrodes. Therefore, the diffusion of both energetic electrons and O^+ ions is correlated with the decrease in O^+ emission line magnitude in the low pressure and high power regime, as shown in Fig. 4.2.4. The magnitude of O emission line shows a different and more expected behavior according to the electron energy distribution function for all pressure and power values, since atomic oxygen (O) is a neutral species and is unaffected by the electrostatic potential at the sheath-negative charge layer and the low energy electrons (which generate O) do not have enough energy to cross the electrostatic potential to diffuse to the electrodes.

The behavior at 700 and 800 Watts shown in Fig. 4.2.4 (b) may be explained by the tendency of rf power to generate ions. The electron density in the high-energy tail of the electron energy distribution function is proportional to the rf power (see Section 2.6 in Chapter 2). The electron distribution is fixed for a particular rf power. This means that for a particular rf power, there is a tendency to generate a certain number of high-energy electrons. As this density is fixed for a particular rf power, it may be said that the amount of ionization stimulated by these high-energy electrons will also be fixed. However, as the pressure is increased (keeping the power constant), the ionization rate falls as the density of energetic electrons, according to the electron energy distribution function, is negatively correlated to pressure (see Section 2.6 in Chapter 2). This is evident for low rf power of 500 and 600 Watts, as shown in Fig. 4.2.4 (b), where the O^+ emission line magnitude keeps decreasing with increasing in pressure. At 700 Watts, on the other hand, the O^+ emission magnitude increases from 2 to 3 Torr and subsequently starts decreasing with further increase in pressure. Similarly, when the rf power is increased to 800 Watts, the O^+ emission magnitude increases until 4 Torr before it starts decreasing with any further increase in pressure. Therefore, it appears that for a particular rf power a specified pressure is required to achieve maximum ionization.

Our experiments suggest that the O^+ emission line magnitude depends upon the energy of the electrons, high-energy electron density, and the diffusion of both electrons and positively charged ions. Therefore, in order to achieve maximum ionization, a balance between the electron energy, yhe high-energy electron density, and diffusion is required. Since this balance is achieved indirectly by rf power and pressure, they act as the control parameters.

4.4 Sample heating mechanisms

There are three plausible mechanisms for sample heating within a plasma: namely, (i) radiative heat transfer (via reactions involving O and O^+ ions), and bombardment (or particle heat transfer) via either (ii) O^+ ions or (iii) electrons.

1. Radiative heat transfer – The ionization and recombination reactions happen simultaneously within the plasma. Since some reactions involve the expulsion of energy in the form of heat, it is plausible that the sample may absorb heat due to radiative heat transfer via the photons emitted from the reactions.

2. O^+ bombardment - The O^+ ions may be responsible for the sample heating due to kinetic impact with the sample. Compared to electrons, the O^+ ions have larger mass and more momentum and therefore they can generate more energy transfer for the same velocity of impact. Hence, O^+ can impart more energy to the sample to increase its temperature. However, capacitively coupled plasmas are known as ‘non-thermal’ or ‘cold’ plasmas as the ion temperatures are much lower in comparison to electron temperatures. The ion temperatures are usually of the order of a few hundred Kelvin in the capacitively coupled plasmas. Ion temperatures of 500 K (277 °C) were measured for the capacitively coupled plasma at a power of 600 Watts in a pressure range of 10-60mTorr [64]. This temperature is lower than the sample temperatures measured in this thesis, which are in the range of 620-770 K (345-487 °C) (see Fig. 4.1.2).

3. Electron bombardment - It is plausible that the sample heating is also associated with the electrons within the plasma. In comparison to the O^+ ions, the electrons have a temperature, which is in the range of ~1.2 – 4.8 x 10^5 K for the investigated experimental conditions, which makes thermal heating by the electrons possible.

However, due to their lower mass, the electron density near the sample would need to be very high to achieve appreciable heating.

The sample temperature may be affected by any of the above mechanisms or due to some combination of these heating mechanisms. However, definitive determination of the heating mechanism is beyond the scope of this thesis and is a recommendation for future work.

4.5 Effects of conductor on optical emissions and sample temperature.

It has been reported that placing an electrical conductor in thermal contact with the sample increases the effectiveness of film crystallization [25]. Therefore, a gold foil was used to gauge the effects of placing a conductor in thermal contact with the back-side of the sample on optical emissions and temperature. Ohsaki *et al.* [25] used copper as the electrical conductor, however, we have chosen gold as it is less susceptible to oxidation in an oxygen plasma.

The magnitude of the O^+ emission lines are always greater for samples without the presence of a back-side conductor in comparison to sample with a conductor in place (ΔO^+ in Fig. 4.2.6 (a)). This may be due to the fact that the QC845 coated quartz sample is an insulator and hence charges up negatively within the plasma. The negative charges would attract positively charged ions (O^+) towards the sample, whereas for the same sample with a gold film attached, the negative charges are readily exchanged with the plasma due to the conductive nature of gold. The decrease in the negative charge density around the sample results in the reduction of the overall magnitude of O^+. This decrease in the O^+ magnitude around the sample in the presence of a conductor contradicts the

hypothesis provided by Ohsaki [25], who suggested that the electric field increases around the sample when a conductor is placed behind it. If the electric field did increase, one would expect more positive ions closer to the sample (with a back-side conductor) as the electric fields terminates on the conductor and attract more positive ions on the conductive surface. Our measurements indicate the presence of a lower concentration of O^+ around the sample when in contact with a back-side conductor, making the hypothesis of electric effects around the sample improbable. The ΔO does not show any trends with the applied rf power. This may be due to the fact that atomic oxygen carries no charge and is therefore unaffected by the charging and discharging of the sample.

The Au foil inside the plasma on its own heats to a greater extent in comparison to a quartz sample both with and without Au foil on the back-side. For a better understanding, the results from Fig. 4.1.3 and Fig. 4.1.1 are re-plotted in Fig. 4.5.1.

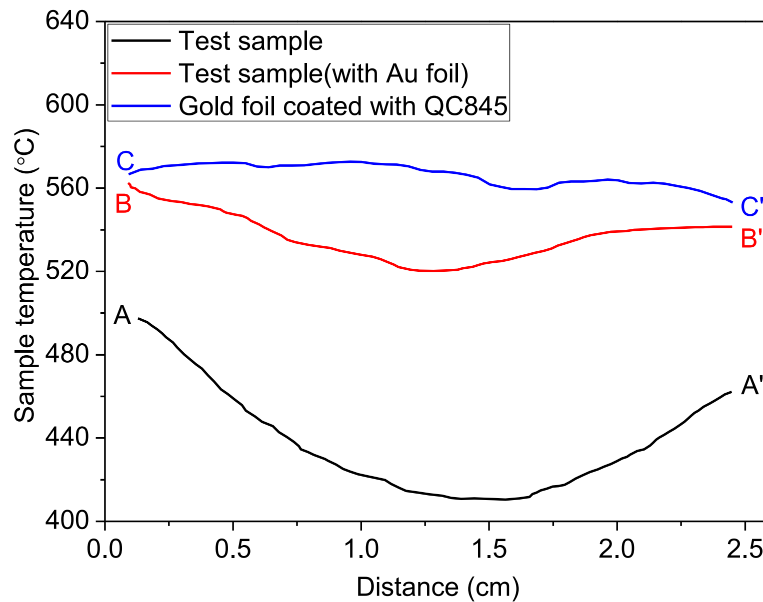

Fig. 4.5.1: Effect of conductor on temperature & thermal variations.

It can be observed from Fig. 4.5.1 that the temperature of the gold foil on its own (CC') is greater in comparison to the test sample (with Au foil at the backside-BB') and the test sample alone (AA'). Therefore, it appears that gold heats to a greater extent in the plasma and increases the temperature of the test sample through thermal contact. This can be confirmed by looking at Fig. 4.1.6, where the temperature in the middle of the sample was increased due to the presence of a back-side conductor. In addition, it can be observed from Fig. 4.1.11 (a & b) that the temperature of the test sample with deposited gold is slightly higher in conparison to the temperature of the test sample with gold foil at the sample backside. This is due to the fact that the thermal contact is much better for the deposited gold than for the foil.

It can also be noticed from Fig. 4.5.1 that the temperature uniformity has improved in the presence of a back-side conductor. This improvement in the temperature spatial uniformity could be expected as the gold is a good conductor of heat, whereas the quartz samples are poor conductors of heat.

4.5.1 Inductive heating and skin effects

The increase in temperature (with conductor) may be linked to inductive heating. The alternating current present in the plasma (13.56 MHz) may generate eddy currents in the conductor, which then lead to the heating of conductor. This induction heating is also known as Joule heating. The amount of heat released via Joule heating is proportional to the square of the current and the resistance of the conductor such that:

$$H = I^2 R \qquad \textbf{4.5.1}$$

where, H = heat released

I = current through the conductor

R = resistance of the conductor

Assuming that the current flowing through the conductor remains relatively constant under similar plasma conditions, if different materials are used then the heat generated by the respective material will be proportional to the resistance of the material. If we keep the area and the length of the conductor similar, the resistance becomes proportional to the resistivity of the material (heat generated will be proportional to the resistivity). To check the effects of resistivity on sample temperature, we have placed foils of copper, gold, and aluminum in thermal contact with the backside of the test sample (QC845 coated fused quartz). Our test sample temperature measurements (with and without backside gold) indicate that the sample temperature in our experiments lies in the range of 300-600 °C. Therefore, the resistivity is calculated for this temperature range and is presented in Table 4.5.1 for the respective metals.

Table 4.5.1: Resistivity and skin depth of copper, gold and aluminum in the temperature range of 300-600 °C and at a frequency of 13.56 MHz

Material	ρ (10^{-8} Ω-m)	μ (μo*μr)	δ (μm)
copper	3.5-5.5	1	25.6-32
gold	4.7-7.2	1	29.6-36.7
aluminum	5.9-9.2	1	33-41

It can be seen from Table 4.5.1 that the resistivity value of aluminum is greater than both gold and copper, and one would expect a sample in thermal contact with aluminum to reach higher temperature in comparison to samples in thermal contact with gold and copper (under similar chamber conditions). However, Fig. 4.1.11 (a) shows that the

temperature for the QC845 coated quartz sample in thermal contact with backside gold and aluminum foil is almost the same and is greater than the temperature of the sample in thermal contact with backside copper.

This behavior may be explained based on the skin effect in conductors. At high frequencies most of the electric current flows in the "skin" or outer layers of the conductor, between the outer surface and a thickness called the skin depth (δ).

$$\delta = \sqrt{\frac{2\rho}{\omega_{rf}\,\mu}} \qquad \textbf{4.5.2}$$

where, ρ = resistivity of the conductor.

ω_{rf} = angular frequency = $2\pi \times$ frequency (υ_{rf}).

μ = absolute magnetic permesability of the conductor.

μ = μ_o $(4\pi x10^{-7})*\mu_r$ (relative permeability).

Equation 4.5.2 shows that the skin depth is directly proportional to the square root of resistivity of the material, and is inversely proportional to the square root of the frequency (13.56 MHz for our experiments) and magnetic permeability of the material. The skin depths are calculated for aluminum, gold and copper (see Table 4.5.1). It can be seen from the table that the skin depth for aluminum and copper are in the range of 33-41 and 25-32 μm, respectively. The oxide layer that forms at a temperature of 600 °C for aluminum is 0.2 μm thick [65] and for copper, it is about 35 μm thick [66]. Lower temperature of test sample in thermal contact with copper in comparison to the test samples in thermal contact with gold and aluminum may be due to a thick oxide layer

developing on the copper in the oxygen plasma, which adversely affects the skin depth making our copper foil a relatively poorer conductor at these frequencies. Nevertheless, one would expect the temperature of the test sample in thermal contact with aluminum to be higher than the test sample in thermal contact with gold as aluminum has a higher resistivity than gold. This behavior is not observed (see Fig. 4.1.11(a)).

It is possible that the oxide layer on aluminum grows thicker than 0.2 μm in a plasma and influence skin depth. Hence, we have chosen gold for further experiments as it does not oxidize in plasma. We deposited a layer of gold of thickness 1.3 μm and 0.6 μm at the backside of two test samples. The temperature for both backside-gold-deposited samples in Fig. 4.1.11 (b) are similar within the experimental range. That is, decreasing the gold thickness does not significantly influence the temperature of the conductor. One would expect to observe in Fig. 4.1.11 (b) different temperatures for the two cases of different thicknesses of the gold layer. Since, such a change is not observed it is possible that inductive heating is not influencing the temperature of the conductor.

4.6 Reactions involved in the oxygen plasma

We have observed from optical emission data in Fig. 4.2.1 that O and O^+ are the dominant species that are correlated with observed optical emission spectra. The dissociation of oxygen molecules (O_2) to generate atomic oxygen (O) requires a threshold energy of 5 eV, while the generation of singly ionised atomic oxygen (O^+) requires a minimum energy of 11.6 eV (see Table 2.2.1 in Chapter 2). The Langmuir probe measurements presented in Fig. 4.2.5 show that the electron temperature lies in the range of 12-43 eV. An electron temperature in excess of 11 eV is required for all plasma conditions supporting the generation of both O^+ and O. The dissociation of the

oxygen molecules can be achieved at low energies and generally results in the generation of two types of oxygen atoms namely O (^{1}D) and O (^{3}P). The O (^{3}P) is the ground state oxygen atom and the O (^{1}D) is metastable atomic oxygen. The reactions involved in the generation of O (^{1}D), O (^{3}P) and O^+ are listed in Table 4.6.1.

Table 4.6.1: Reactions involved in the generation of O (^{1}D), O (^{3}P), and O^+.

No.	Reactions	ϵ_T (ev)
1.	$O_2(a^1\Delta_g)$ +.e → 2O (^{3}P) + e	5.02
2.	O_2 + e → 2O (^{3}P) + e	6.00
3.	O (^{3}P) + e → O (^{1}D) + e	2.00
4.	$O_2\,(a^1\Delta_g)$ + e → O (^{3}P) + O (^{1}D) + e	7.42
5.	O_2 + e → O (^{3}P) + O (^{1}D) + e	8.40
6.	O (^{1}D) + e → O^+ + 2e	11.60
7.	O (^{3}P) + e → O^+ + 2e	13.60
8.	O_2 + e → O^+ + O (^{3}P) + 2e	16.81

Considering the activation energies of the five reactions listed in Table 4.6.1, it can be seen that the threshold energy for the generation of O (^{3}P) is 5eV, and O (^{1}D) from metastable O_2 is 7.0 eV. Table 4.6.1 also lists the reactions generating O^+. It is clear from these reactions that the generation of O^+ from the O (^{1}D) [reaction 6] state requires a lower energy in comparison to the energy required for generation from ground state atomic oxygen O (^{3}P) [reaction 7] and O_2 [reaction 8]. Provided the singular O species have a sufficient lifetime, then they can undergo one transition to excited O and then a second transition to O^+ without requiring larger electron energies. It was shown by Lee *et al*. [67] that O (^{1}D) is lost predominantly through diffusion at lower pressures (<10 mTorr) and via ionization at higher pressures. In addition, it was also observed by Lee *et al.* [67] that the O (^{1}D) loss occurs via self ionization to O^+, and that O^+ are the

dominant species if the system has more O (^{1}D) as compared to O (^{3}P). This is because metastable atomic oxygen O (^{1}D), which is generated through the dissociation of oxygen molecules [reaction 4] and excitation of ground state oxygen atoms (O^3P) [reaction 3 [67]] , is being converted into O^+ [reaction 6]. In addition, O^+ is also generated via direct ionization through O_2 molecules and (O^3P) [reaction. 7]. In this case, the magnitude of O^+ generated is expected to be higher than the magnitude of atomic O within the plasma.

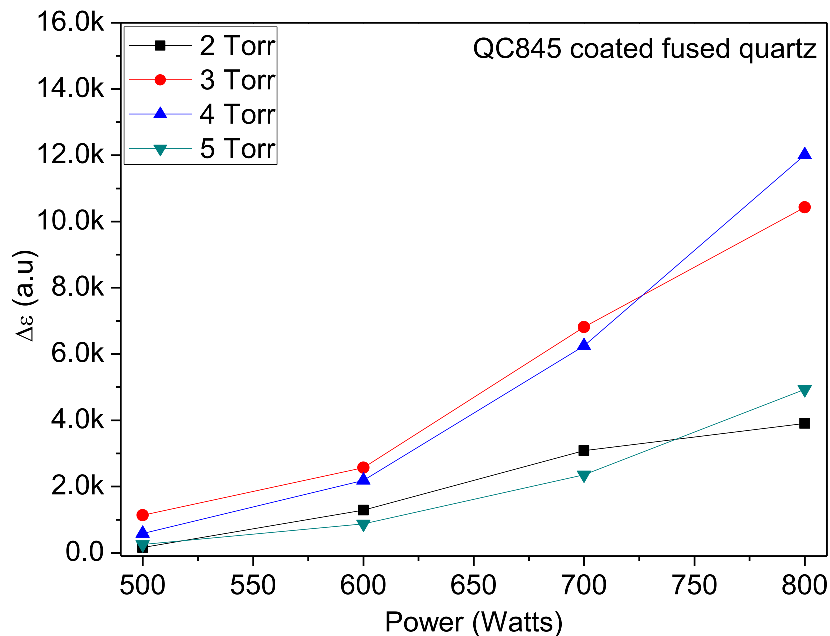

Fig. 4.6.1: Difference in the emission magnitude of O^+ and O as a function rf power.

Fig. 4.6.1 shows the Δε as a function of rf power for various pressures. Here Δε is the difference in magnitude of the emission lines of O^+ and O ($\Delta\varepsilon = [O^+] - [O]$) for the QC845 coated fused quartz sample without a backside conductor. It can be observed from the plot that Δε is positive under all conditions, and is increasing with an increase in rf power. This means that the O^+ emission magnitude is always greater than the magnitude of O emission within the range of our experimental conditions. The positive

value of Δε suggests that the plasma has more $O(^1D)$ than O (^3P) species under our experimental conditions. Therefore, the reactions involving the generation of $O(^1D)$ appear more probable than the reactions involving the generation of $O(^3P)$ only. The increase in Δε with increasing rf power may be attributed to an increase in the ionization, which is positively correlated to the rf power.

4.7 Sample temperature as a function of reaction quotient

We have noted previously that the sample temperature is a linear function of the summation of the logs of magnitudes of the emission lines of O^+ and O (see Fig. 4.2.7) The form of this relation is similar to the relationship between the Gibbs free energy and the reaction quotient (Q). The reaction quotient is a function of the activities or concentrations of the chemical species involved in a chemical reaction. Thus, for a reaction of the form

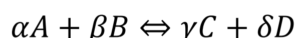

$$\alpha A + \beta B \Leftrightarrow \gamma C + \delta D$$

The reaction quotient is:

$$Q \quad = \quad \frac{[C]^{\gamma}[D]^{\delta}}{[A]^{\alpha}[B]^{\beta}} \qquad \textbf{4.7.1}$$

The Gibbs free energy is basically the amount of work that can be obtained from a given reaction for products and reactants at a given concentration without increasing the total volume of the system. Gibbs free energy (ΔG) in its general form is shown in Equation 4.7.2.

$$\Delta G = \Delta G^{\emptyset} + RT \ln Q \qquad \textbf{4.7.2}$$

where, $\Delta G^{\emptyset}$ = standard Gibbs energy.

R = gas constant.

T = temperature of the system.

If the concentration of reactants is relatively constant then the Gibbs free energy would simply be related to the sum of the logs of the concentration of the products. The behavior observed in Fig. 4.2.7, where the temperature of the QC845 coated quartz sample increases linearly with the sum of the logs of O and O^+ emission line magnitudes, can then be explained in terms of a direct relationship between the sample temperature and the Gibbs free energy released in the plasma. This suggests that the temperature of the sample is correlated to the energy released by reactions occurring within the plasma. Within the pressure and power range evaluated in this thesis, these reactions are dominated by the generation of O and O^+. It also suggests that the concentration of reactants does not change significantly as the pressure and power are varied.

4.8 Summary

We have shown that O^+ and O are the dominant species observable in the optical emission spectrum in the 200-800 nm wavelength and only the 310 nm (O^+) and 777 nm (O) emission lines were helpful in characterizing the plasma under the different conditions of interest. We have shown that the O^+ shows a different trend in comparison to atomic oxygen (O) under different power and pressure conditions. Electron energy, electron density, and diffusion were proposed as being the possible reasons for the different emission characteristics of the O^+ and O under varying experimental conditions. We also showed that the sample temperature was dependent on the summation of the logs of the magnitudes of both O and O^+ optical emission lines and hence may be related to the free energy of reaction of the O and O^+ ions in the plasma.

We discussed some of the reactions that may be involved in plasma generation within our experimental range, and showed that the O_2 and metastable oxygen molecule ($O_2(a^1\Delta_g)$) are involved in the generation of ground state atomic oxygen (O^3P) and metastable atomic oxygen (O^1D), which further were shown to be responsible for the generation of O^+.

The temperature of the sample without using a back-side conductor lies in the range of 350 °C-500 °C within the investigated conditions. The maximum temperature (for a sample without Au foil) of about 500 °C was observed at an rf power of 800 Watts and at a pressure of 3 Torr. The measured temperatures are much higher in comparison to the temperatures measured by Ohsaki *et al.* [22], which be found to never increase above 250 °C under the similar experimental conditions.

We have shown that placing a metallic electrical conductor in thermal contact behind the sample (i) increases the temperature; (ii) decreases the O^+ emission magnitude, (iii) improves the temperature uniformity as compared to samples without a backside conductor. The decrease in the O^+ magnitude around the sample in the presence of a conductor also contradicts the hypothesis proposed by Ohsaki [25], which suggested that the electric field increases around the sample when a conductor is placed behind it. Furthermore, the skin depth of the conductor does not seem to be a factor, providing the conductor does not significantly oxidize in the process.

5

Material characterization

The crystallization of amorphous TiO_2 and ITO thin films as reported by Ohsaki *et al.* [22, 26] was achieved at relatively low temperatures with plasma treatment, in comparison to rapid thermal annealing (RTA) and furnance treatments. It was shown that the activation process for the crystallization in plasma treatment is different from ordinary heat treatment [22-26]. This chapter will investigate the plasma crystallization process as a function of rf power and pressure, and compare the plasma treated garnet thin films with RTA and furnance treated films.

The chapter begins by presenting the results of characterization of plasma, RTA and furnance annealed $Bi_2Dy_1Fe_4Ga_1O_{12}$ (BiDyGa:IG) films under different process conditions. This section will present the effects of plasma exposure on the samples and the dependence of plasma annealing on rf power and pressure. Thin film characterization techniques such as XRD, AFM, TEM, EPMA and XPS were used to characterize the treated films. Subsequently, we discuss the results and compare plasma annealing with RTA and furnance annealing.

5.1 Characterization of $(BiDy)_3(FeGa)_5O_{12}$ films

The $(BiDy)_3(FeGa)_5O_{12}$ films were annealed via plasma-treatment under varying power and pressure conditions. In addition, some samples were annealed via RTA and furnance annealing for comparison purposes.

Table 5.1.1: Annealing of BiDyGa:IG samples via plasma, RTA and furnance.

No.	Sample	Process conditions				State	Faraday rotation (degree/μm)
Plasma annealed samples (all 15 minutes)							
		Power (Watts)		Pressure (Torr)	Temp. (°C)		
1.	α-500	500 W		2 T	515	Crystallized	3.1
2.	α-600	600 W		2 T	534	Crystallized	1.7
3.	α-700	700 W		2 T	564	Crystallized	3.5
4.	α-800	800 W		2 T	558	Crystallized	4.3
5.	β-500	500 W		3 T	485	Amorphous	0.0
6.	β-600	600 W		3 T	517	Crystallized	3.2
7.	β-700	700 W		3 T	543	Crystallized	3.1
8.	β-800	800 W		3 T	570	Crystallized	2.7
9.	β800NG	800 W		3 T	500	Amorphous	0.0
10.	γ-500	500 W		4 T	424	Amorphous	0.0
11.	γ-600	600 W		4 T	469	Amorphous	0.0
12.	γ-700	700 W		4 T	515	Crystallized	3.1
13.	γ-800	800 W		4 T	548	Crystallized	4.9
RTA annealed samples (both 15 minutes)							
		Ramp rate (°C/s)	Flow rate (sccm)	Ambient	Temp. (°C)		
14.	R-1	10	100	O_2	570	Amorphous	0.0
15.	R-2	30	100	O_2	640	Crystallized	2.2
Furnance annealed samples							
		Time (min.)		Ambient	Temp.(°C)		
16.	O-1	15		O_2	570	Amorphous	0.0
17.	O-2	90		O_2	570	Amorphous	0.0
18.	O-3	90		O_2	630	Crystallized	6.0

Table 5.1.1 provides a summary of the main results for the investigated samples. It lists the process conditions, the material state (crystalline/amorphous), and the achieved Faraday rotation for plasma, RTA and furnance annealed BiDyGa:IG films. Samples 1-13 were annealed in an oxygen plasma. Samples α, β, and γ were exposed to plasma pressures of 2, 3, and 4 Torr, respectively. The number following the α, β, γ in the sample identifier scheme refers to the rf power during plasma exposure of the sample. It is to be noted that all plasma-treated samples listed in Table 5.1.1 were annealed with gold foil in thermal contact with the garnet sample, except sample 13 (β-800-NG). Sample β-800-NG was treated in plasma without placing a gold foil behind the sample. All the plasma annealings were performed for 15 minutes in an oxygen plasma. Samples R-1 and R-2 were annealed for 15 minutes via rapid thermal annealing. Sample R-1 was annealed at a temperature of 570 °C and at a ramp rate of 10 °C/s using an oxygen flow rate of 100 sccm to mimic the temperature profile in the plasma, while sample R-2 was annealed at a temperature of 640 °C at a ramp rate of 30 °C/s using a flow rate of 100 sccm. Samples O-1, O-2 and O-3 were annealed in a conventional tube furnance. Samples O-1 and O-2 were annealed at a temperature of 570 °C for 15 minutes and 90 minutes, respectively. Sample O-3 was annealed at a temperature of 630 °C for 90 minutes. Both RTA and furnance annealing was undertaken in an oxygen environment. Some additional annealing results of BiDyGa: IG films treated via plasma, RTA and furnance are presented in Appendix II-A.

It is to be noted that the temperature listed in Table 5.1.1 for plasma annealing is taken from the temperature measurements of a QC845 coated quartz sample (with and without Au foil as appropriate). This is because the measurement of sample temperature via the thermal imager (which requires coating with QC845) is not generally compatible

with subsequent physical characterization of the garnet samples. However, the sample temperature of the garnet films was verified by coating a garnet sample with QC 845 and placing a gold foil in thermal contact with the backside and measuring the temperature with the thermal imager. A comparison of this measurement with those from Chapter 4 is shown in Fig. 5.1.1

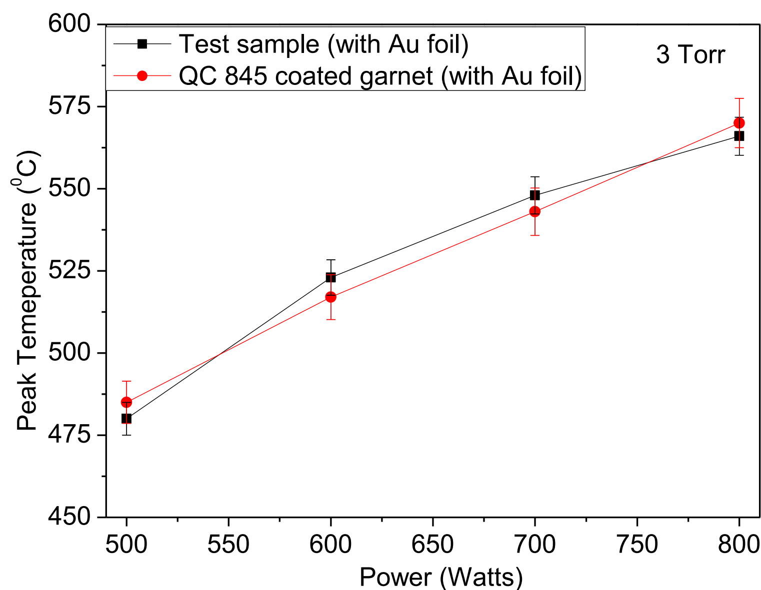

Fig. 5.1.1: Temperature of QC 845 coated quartz sample [Test sample] (with back-side Au foil) and QC 845 coated garnet (with backside Au foil) at a pressure of 3 Torr as a function of rf power. Error bars represent the relative standard deviation of 1.35 %.

From Fig. 5.1.1, it can be observed that the temperature of both the coated quartz and the coated garnet film are the same within the experimental error. This is unsurprising as the only difference between both samples was the thin garnet film that has been deposited on a quartz substrate the same size and thickness as the QC845 quartz sample.

5.1.1 Crystallinity (X-ray diffraction)

XRD was performed in order to check for the crystallinity of the annealed samples. The XRD results of annealed BiDyGa:IG samples are summarized in Table 5.1.1 and XRD patterns are presented in Fig. 5.1.2.

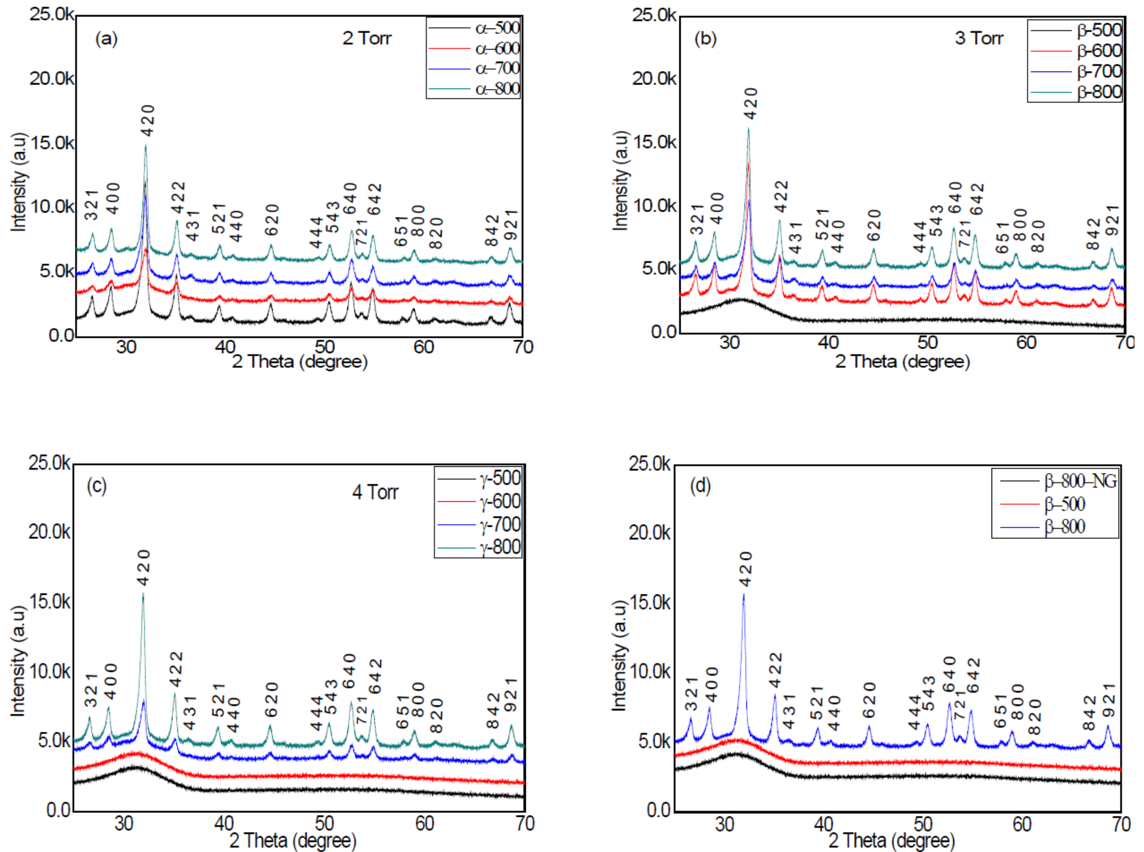

Fig. 5.1.2: XRD spectrum of BiDyGa:IG films for plasma-treatment at (a) 2 Torr, (b) 3 Torr, (c) at 4 Torr; and (d) for RTA and furnance treated BiDyGa:IG samples.

Fig. 5.1.2 (a), (b) and (c) shows the XRD spectra of plasma annealed films for plasma pressures of 2, 3 and 4 Torr, respectively. Fig. 5.1.2 (d) presents the XRD patterns for RTA and furnance annealed films. It can be observed from Fig. 5.1.2 (b & c) that samples β-500, γ-500, and γ-600 are still in amorphous state, whereas all other plasma-treated samples are crystallized and show characteristic peaks for garnet, including the large peak at 32° [68] [69]. A comparison of plasma-annealed samples in

Fig. 5.1.2 (b) shows that samples β-600, β-700 and β-800 are crystallized, whereas samples β-800-NG and β-500 do not show any signs of crystallization. From Fig. 5.1.2 (d), it can be observed that two furnance annealed samples O-1 and O-2, and one RTA annealed sample R-1 are still in amorphous state, even though they are annealed at temperatures similar to those occurring during the plasma annealing.

5.1.2 Faraday rotation and optical transmission

We know from our thermal measurements (see Fig. 4.1.2 in Chapter 4) that samples exposed to plasma show temperature spatial non-uniformities. In particular, the samples are hotter around the edge in comparison to the centre. Therefore, we examined the Faraday rotation and optical transmission at three different positions on plasma-annealed samples; in the centre (point C), near to the edge (point A), and in-between (point B). The results are presented in Fig. 5.1.3.

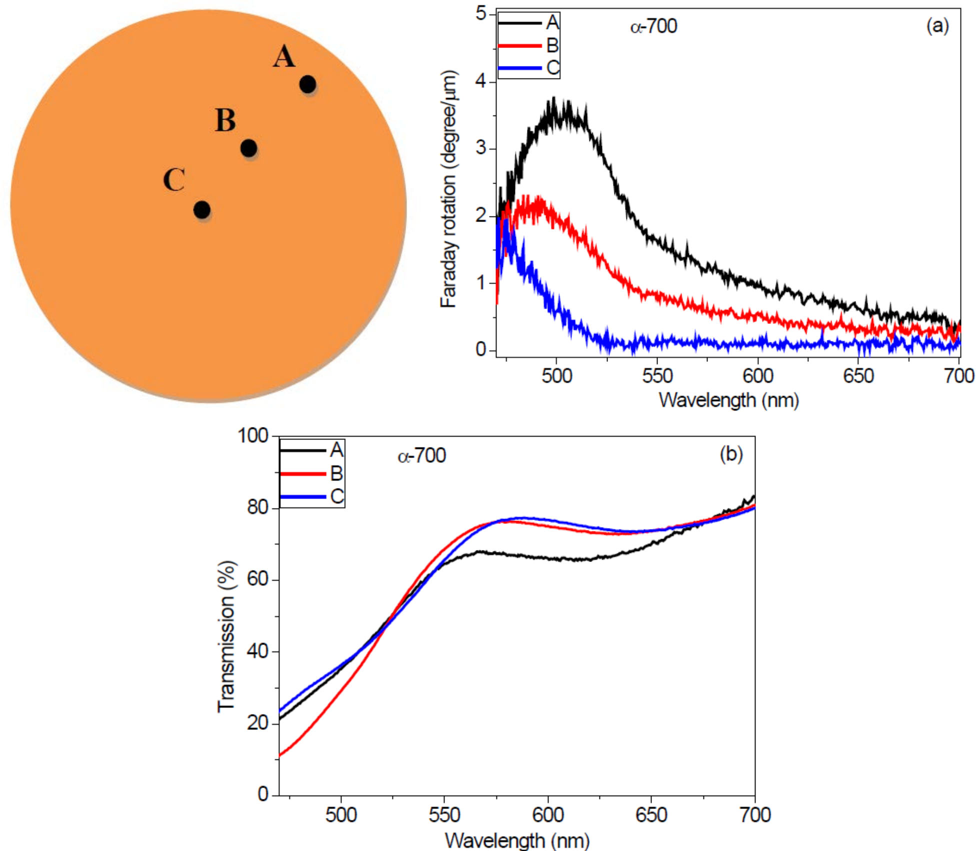

Fig. 5.1.3: (a) Faraday rotation and (b) optical transmission at a magnetic field of 0.54 T and, as a function of wavelength at different points on the sample α-700.

Fig. 5.1.3 shows the Faraday rotation and optical transmission variations from the three points shown in the figure for sample α-700. A peak in the Faraday rotation spectrum is observed at a wavelength of around 500 nm for the edge of the sample. This peak in Faraday rotation appears to shift towards shorter wavelengths for sampling positions moving towards the sample's centre. It can be seen from Fig. 5.1.3 (a) that the degree of Faraday rotation achieved for the plasma-annealed sample monotonically decreases from edge to the middle of the sample. Fig. 5.1.3 (b) shows that sample has lower transmission at point A (at the edge of the sample) in the wavelength region of 550-675 nm as compared to points B and C. This form of variation of Faraday rotation and optical transmission across the sample is consistent for all plasma-annealed

samples. It is to be noted that RTA and furnance annealed samples show uniform Faraday rotation and optical transmission across the sample. For the comparison of crystallization techniques, we will use Faraday rotation and the optical transmission values from the edge of the plasma-annealed sample.

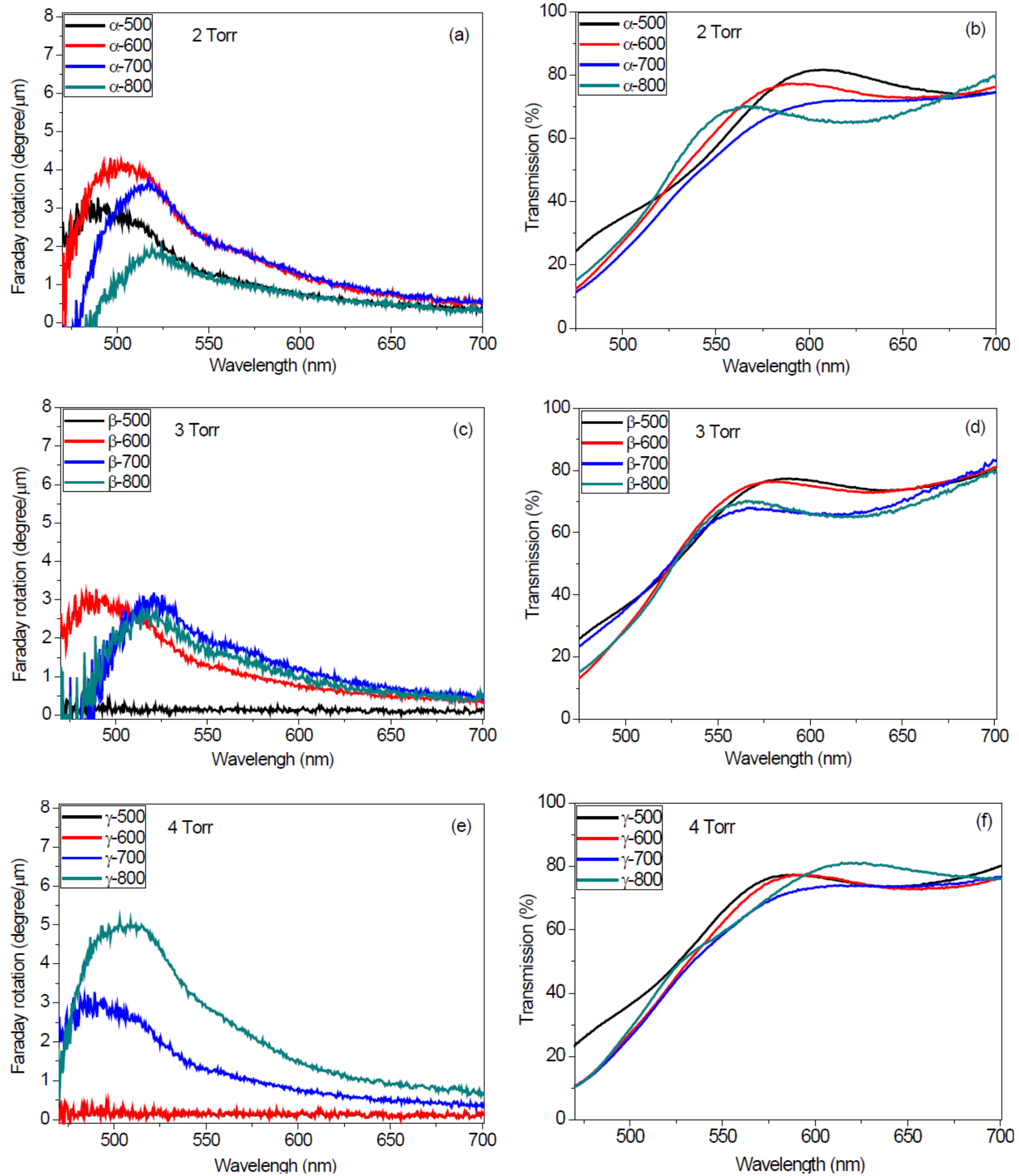

Fig. 5.1.4: Faraday rotation and optical transmission at a magnetic field of 0.54 T and, as a function of wavelength for samples exposed to plasma (a & b) 2 Torr, (c & d) 3 Torr, and (e & f) 4 Torr.

Fig. 5.1.4 shows the Faraday rotation and optical transmission as a function of wavelength for the samples exposed to plasma at 2 Torr, 3 Torr, and 4 Torr. It can be observed from Fig. 5.1.4 (b, d, & f) that the optical transmission does not generally vary substantially with the change in plasma conditions. Considering the Faraday rotation

plots, it can be observed that samples β-500, γ-500 and γ-600 do not show any Faraday rotation. All these samples do not show crystallization and are annealed at temperatures below 500 °C. A maximum Faraday rotation of about 4.9 degree/μm was observed for sample γ-800.

From our thermal measurements in Chapter 4 (see Fig. 4.1.1 & Fig. 4.1.2), we know that the sample temperature attained during plasma exposure is dependent upon the applied rf power and pressure. Therefore, it is possible that the degree of Faraday rotation also depends on the sample temperature achieved during plasma annealing. Hence, the maximum Faraday rotation values from Fig. 5.1.4 are plotted as a function of plasma annealing temperature; the results are presented in Fig. 5.1.5.

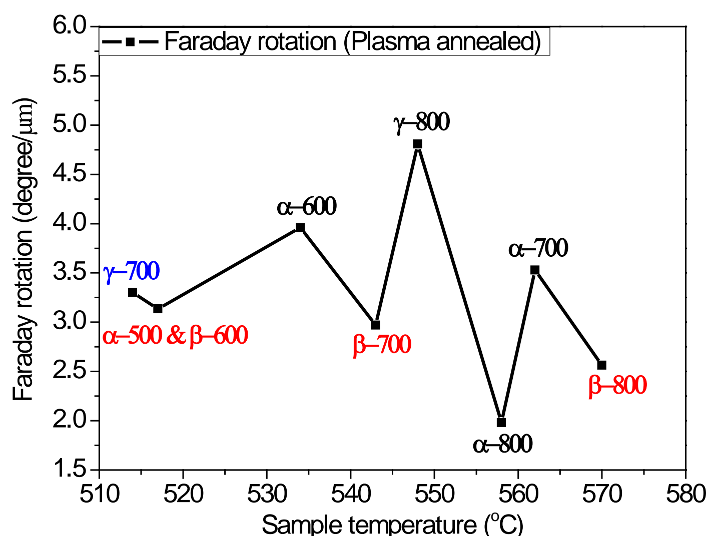

Fig. 5.1.5: Faraday rotation of plasma annealed samples as a function of temperature.

Fig. 5.1.5 shows the maximum Faraday rotation in the 475 nm to 700 nm wavelength range for plasma-annealed samples as a function of sample temperature. It can be seen from Fig. 5.1.5 that the degree of Faraday rotation for the plasma-annealed samples does not show any correlation with the increase in sample temperature.

The Faraday rotation and optical transmission results of plasma-annealed sample (γ-800) are compared with RTA (R-2) and furnance (O-3) annealed samples to compare the effectiveness of these techniques to generate garnet films with optimum magneto-optical properties. For the plasma-annealed sample, the Faraday rotation and transmission value were those taken from the edge of the sample. The results are presented in Fig. 5.1.6.

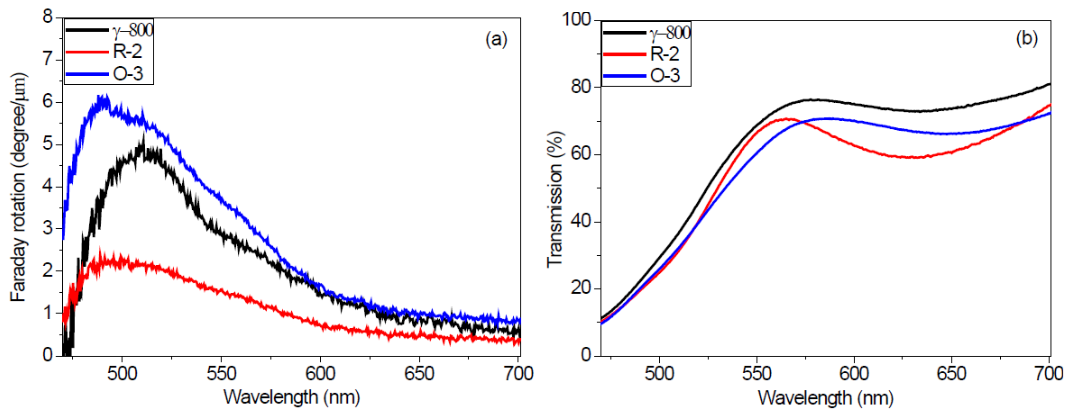

Fig. 5.1.6: (a) Faraday rotation and (b) optical transmission of plasma (γ-800), RTA (R-2), and furnance (O-3) annealed samplesat a magnetic field of 0.54 T.

Fig. 5.1.6 (a) shows Faraday rotation, while Fig. 5.1.6 (b) shows optical transmission as a function of wavelength for plasma, RTA and furnance annealed samples. From the Faraday rotation results in Fig. 5.1.6 (a), it can be seen that O-3 has produced the largest Faraday rotation value of about 6 ^{o}/μm at a wavelength of about 480 nm, whereas plasma annealed (γ-800) and RTA annealed (R-2) samples have achieved a Faraday rotation of about 4.9 and 2.2 degrees/μm at wavelengths of about 520 and 480 nm, respectively. The optical transmission plot in Fig. 5.1.6 (b) shows that sample γ-800 has similar characteristics but slightly better transmission as compared to O-3. The R-2, on the other hand, shows different transmission characteristics in comparison to both γ-800 and O-3.

5.1.3 Surface and Microstructure analysis

5.1.3.1 Atomic force microscopy

Atomic force microscopy was performed to compare the effects of plasma, RTA and furnance annealings on the surface of the garnet films. In a similar fashion to that in Section 5.1.2, the surface of the plasma-annealed samples is examined at three different positions from the centre to the edge of the sample. For comparison between plasma, furnance, and RTA annealing, we chose γ-800, R-2, O-3 samples; all of which have shown significant degree of crystallinity.

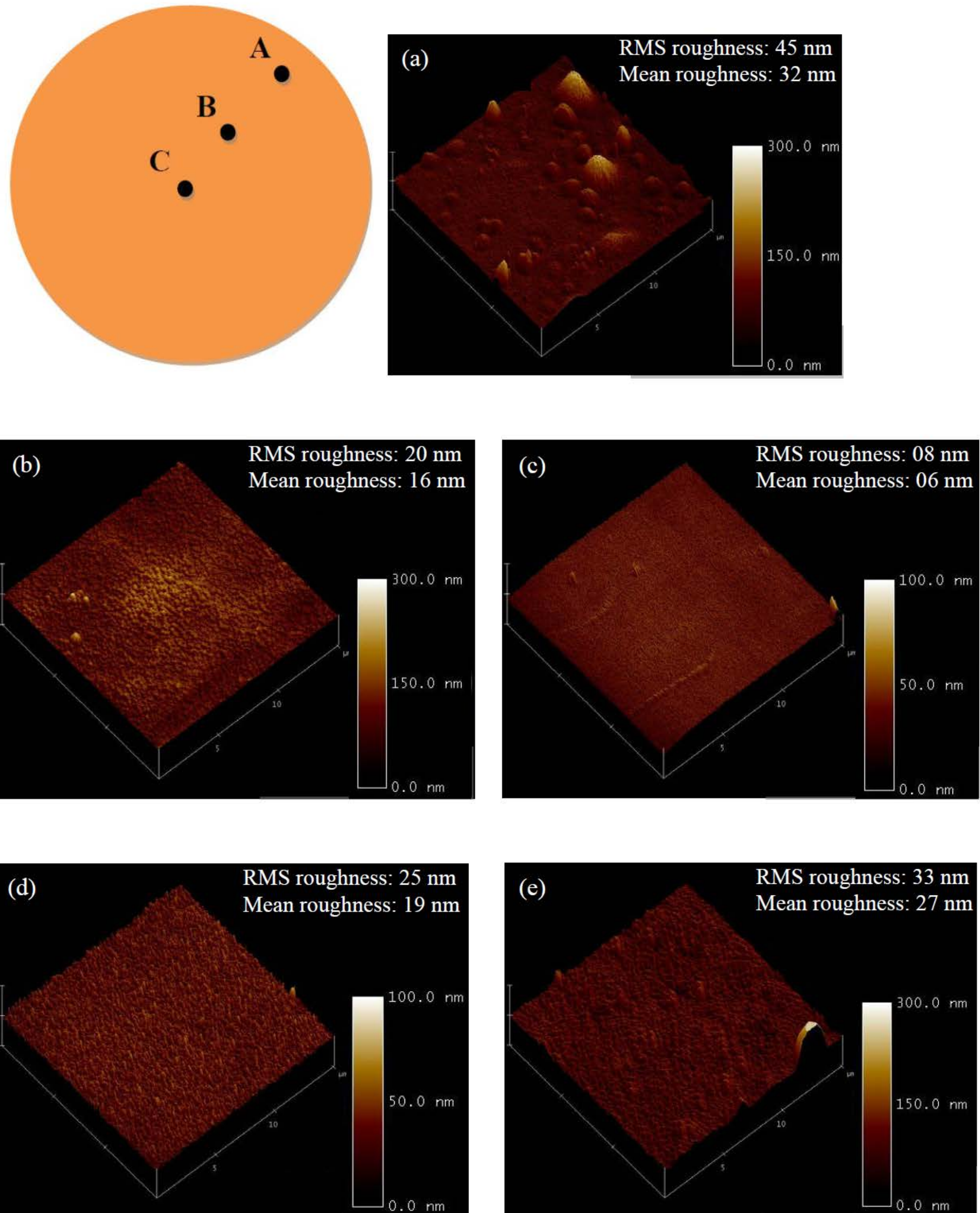

Fig. 5.1.7: AFM images of plasma-annealed sample at (a) point A, (b) point B, (c) point C, and (d) RTA annealed (e) furnance annealed sample.

Fig. 5.1.7 shows the AFM images of plasma (γ-800), RTA (R-2) and furnance (O-3) annealed samples for a scan size of 15x15 µm. Fig. 5.1.7 (a, b & c) shows the images from different sampling points of plasma annealed sample. Fig. 5.1.7 (d) shows the

AFM image of the RTA annealed sample. Fig. 5.1.7 (e) shows the image of the furnance annealed sample. In Fig. 5.1.7 (a), it can be observed that there are significant lumps on the surface of the sample whose origin is unclear. It is evident from Fig. 5.1.7 (a & c) that the surface roughness is maximum near the edge (RMS roughness: 45 nm) and minimum at the middle (RMS roughness: 8 nm) for the plasma annealed sample. In comparison to plasma annealed sample, RTA (RMS roughness: 25 nm) and oven annealed (RMS roughness: 33 nm) samples are smoother than the edge of the plasma annealed sample but rougher than the centre of the plasma annealed sample.

5.1.3.2 Transmission electron microscopy

Transmission electron microscopy was performed on plasma, RTA and furnance annealed samples. For comparison between plasma, furnance, and RTA annealing, we chose γ-800, R-2, O-3 samples; all of which have shown significant degree of crystallinity.

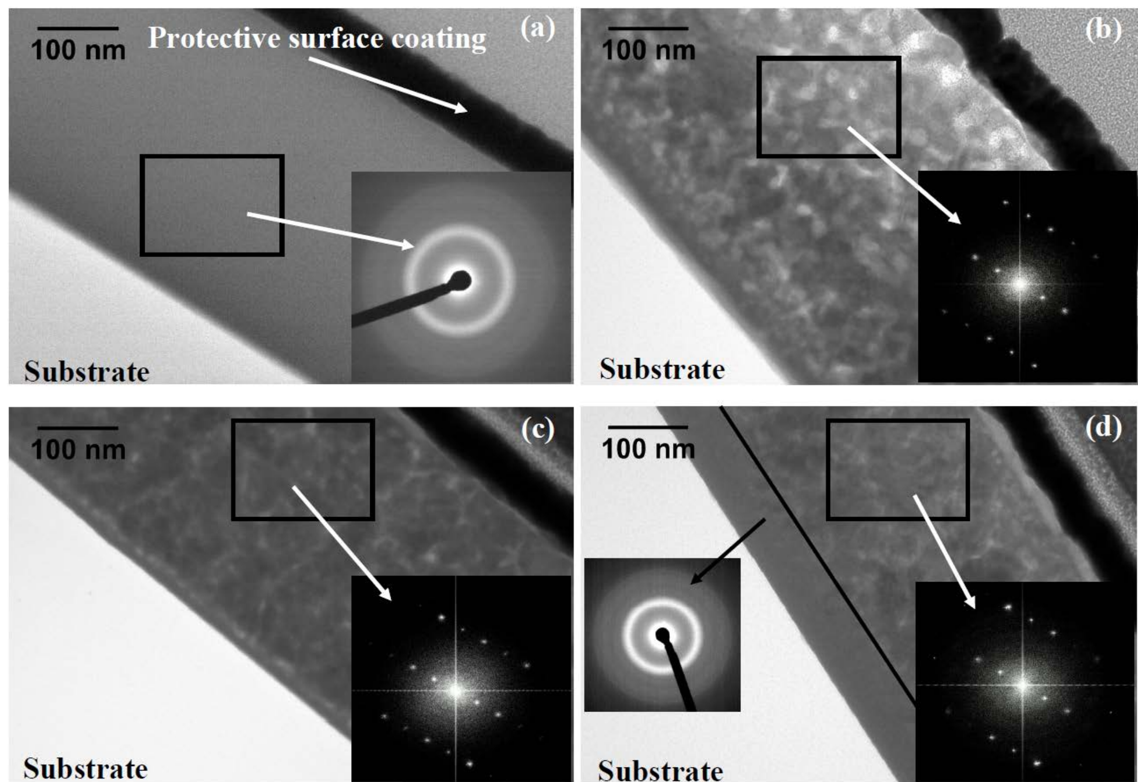

Fig. 5.1.8: TEM images of BiDyGa:IG sample (a) as-grown amorphous (b) plasma annealed {near the edge} (c) furnance annealed (d) RTA annealed thin films.

Fig. 5.1.8 (a) (b), (c), and (d) show TEM images of as-grown amorphous film and plasma, furnance and RTA annealed samples, respectively. The samples are coated with gold layer (black layer) to protect the sample from the ion beam during the sample preparation. Every image includes an inset showing the electron diffraction pattern of the samples. The diffraction pattern in Fig. 5.1.8 (a) confirms that the as-grown film is amorphous. The diffraction patterns in Fig. 5.1.8 (b, c & d) show that plasma, RTA and furnance annealed samples are crystallized. For the furnance annealed sample (see Fig. 5.1.8 (c)), the crystallization appears to be uniform throughout the film, whereas for RTA annealed film (see Fig. 5.1.8 (d)) sample the crystallization appears to proceed from the surface downwards and is not yet complete close to the substrate. From Fig. 5.1.8 (b), it can be observed that the plasma-annealed sample looks different as

compared to both RTA and furnance annealed films especially near to the surface of the plasma-annealed film.

The AFM image (Fig. 5.1.7 (a)) showed lumps in certain areas on the edge of the plasma annealed sample. The AFM only provides the surface information. Therefore, TEM was performed on plasma-annealed sample near to the edge of the plasma-annealed sample in order to examine the lumps in cross-section.

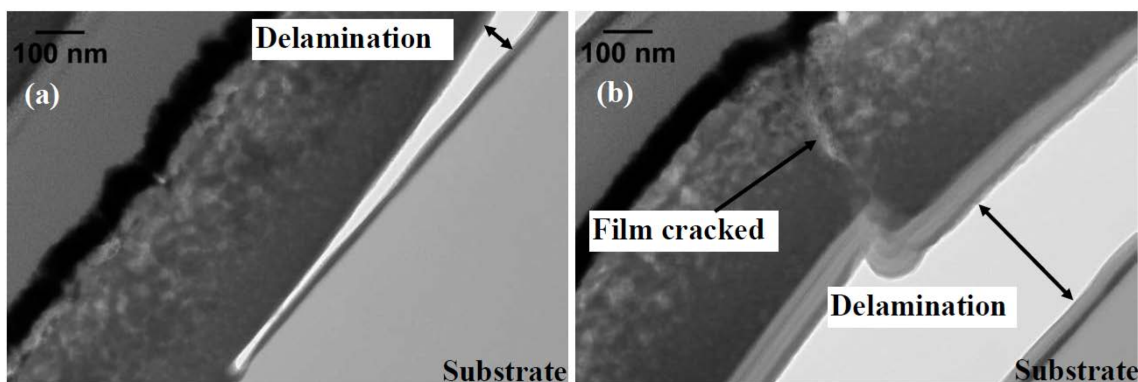

Fig. 5.1.9: TEM images of plasma annealed sample {near the sample edge} showing (a) delamination of film, and (b) delamination with film breakage.

Fig. 5.1.9 shows the TEM images of the lump area of plasma annealed film from near the edge of the sample. Fig. 5.1.9 (a) presents the cross-sectional image showing film delamination. Fig. 5.1.9 (b) shows an image obtained near the centre of the sample lump. It can be observed from Fig. 5.1.9 (b) that delamination of the films has caused the garnet films to crack. This kind of delamination was not observed in either RTA or oven annealed samples. It is to be noted that the delamination of the garnet films during plasma exposure is not directly related to the different thermal expansion coefficients of garnet films and substrate (fused quartz). If that was the case, the samples treated via RTA and furnance would show more delamination, as they were treated at higher temperatures in comparison to the plasma annealed sample.

5.1.4 Compositional analysis

5.1.4.1 Electron probe micro analysis

Electron probe micro analysis was performed on as-grown amorphous, plasma, RTA and furnance annealed samples to determine if there were significant changes in garnet composition during annealing. The plasma-annealed sample was checked at three different sampling points (points A, B, and C as indicated in Fig. 5.1.7). A summary of EPMA characterization for all samples in terms of mole fractions is presented in Table 5.1.2.

Table 5.1.2: Electron probe micro analysis of as-grown amorphous, plasma, RTA and furnance annealed samples.

No.	Sample	Composition (Mole Fraction)				
		Bi	Dy	Fe	Ga	O
1.	Amorphous	1.7	1.15	4.52	1.12	12
2.	Plasma annealed (A)	1.59	1.09	4.51	1.11	12
3.	Plasma annealed (B)	1.52	1.11	4.43	1.06	12
4.	Plasma annealed (C)	1.63	1.06	4.40	1.09	12
5.	RTA annealed	1.65	1.09	4.47	1.07	12
6.	Oven annealed	1.7	1.03	4.46	1.11	12

The experimental errors associated with EPMA lie in the range of 5-10%. The components of bismuth, dysprosium, gallium and iron are normalized with respect to the oxygen concentration. It can be observed from Table 5.1.2 that the composition of all the films is similar within experimental error.

5.1.4.2 X-ray photoelectron spectroscopy

The composition as determined from EPMA is based on full thickness of the deposited film corrected for substrate effects. In order to determine if changes in the

near surface composition may have occurred during annealing, we used x-ray photoelectron spectroscopy (XPS). The experimental error associated with XPS is about 10% for all the materials investigated. XPS was used to analyze the compositional changes of plasma-annealed sample (γ-800), RTA annealed sample (R-2), and furnance annealed sample (O-3) as a function of film thickness (surface depth).

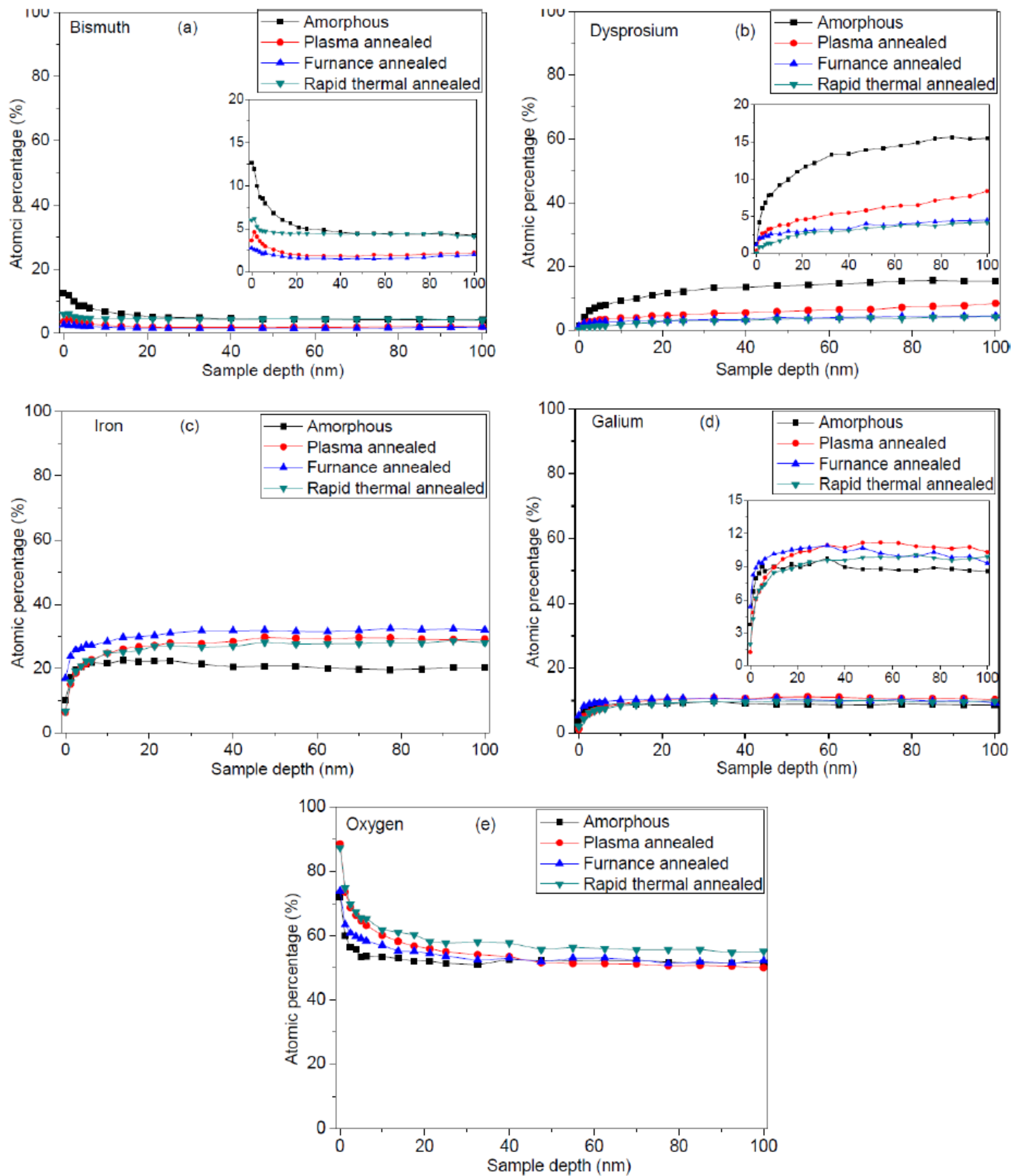

Fig. 5.1.10: Atomic percentage of (a) bismuth, (b) dysprosium, (c) iron, (d) gallium, (e) oxygen for as-grown amorphous, plasma, furnance and RTA annealed samples as a function of surface depth.

Fig. 5.1.10 shows the XPS compositional results of the as-grown amorphous, as well as for plasma, RTA and furnance crystallized samples as a function of depth from the surface of the films. Fig. 5.1.10 (a), (b), (c), (d), and (e) show the atomic percentage of bismuth, dysprosium, iron, gallium and oxygen, respectively. It can be seen from Fig.

5.1.10 (a) that bismuth's atomic percentage decreases as a function of depth for the first 20 nm and then becomes constant. In addition, the bismuth's atomic percentage is similar to each other (within experimental error). The dysprosium's atomic percentage, on the other hand, increases with sample depth throughout the film thickness and is significantly greater for amorphous sample in comparison to the other annealed films. Iron shows distinctive behavior in comparison to other materials as the atomic percentage of iron is slightly greater for plasma, RTA and furnance annealed samples as compared to iron's atomic percentage for the amorphous sample. The gallium and oxygen's atomic percentage shows no significant changes in atomic percentage before and after annealing.

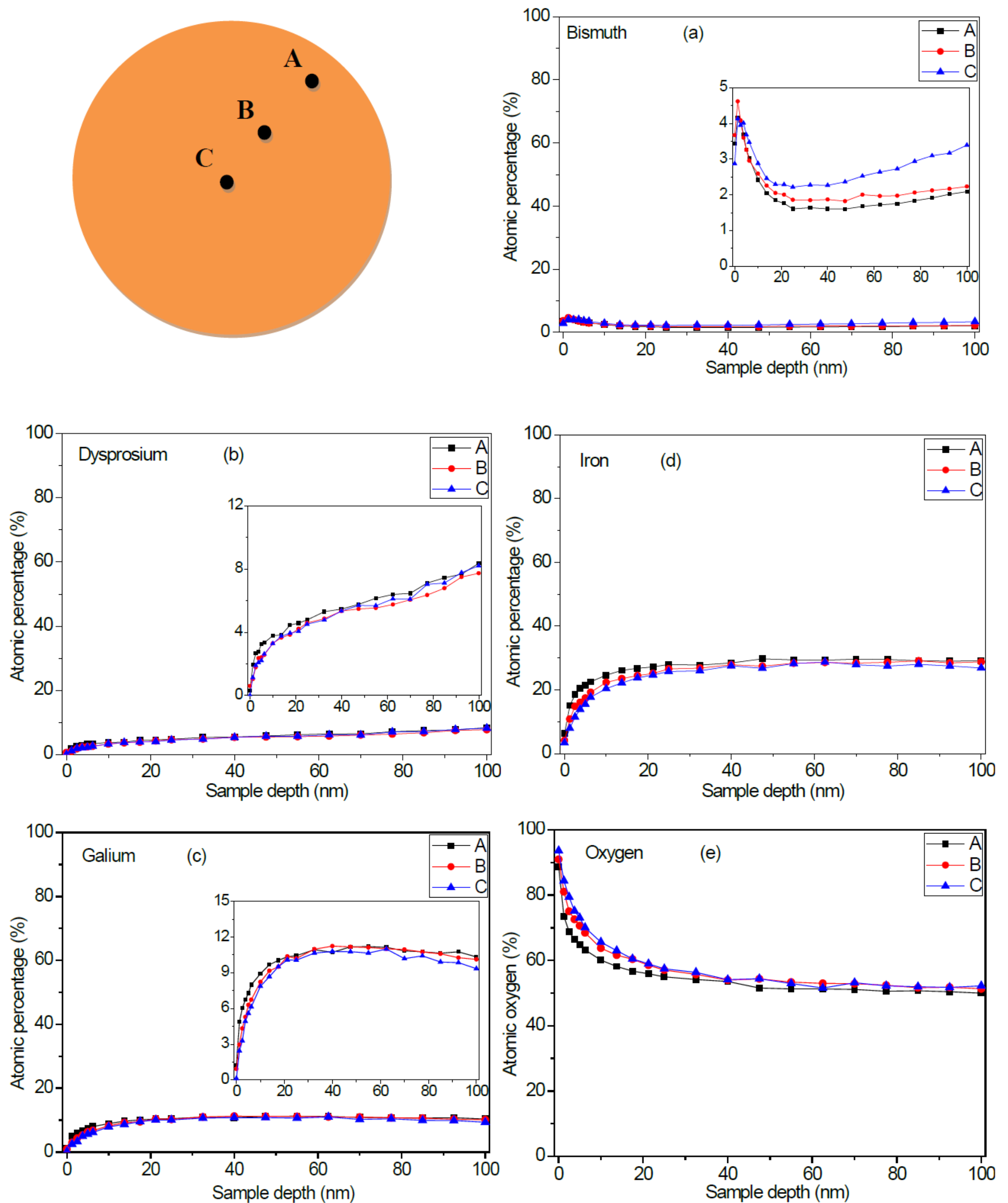

Fig. 5.1.11: Atomic percentage of (a) bismuth, (b) dysprosium, (c) iron, (d) gallium, and (e) oxygen for plasma annealed sample for three different positions on the sample.

Fig. 5.1.11 shows the atomic percentage of bismuth, dysprosium, iron, gallium and oxygen as a function of surface depth for three different positions on the plasma

annealed sample from the centre to the edge. Fig. 5.1.11 (a), (b), (c), (d), and (e) shows bismuth, dysprosium, iron, and oxygen atomic percentages, respectively. It can be seen from the plots that the atomic percentage of bismuth, dysprosium, iron, gallium and oxygen is similar at points A, B and C (within experimental error).

5.2 Discussion

5.2.1 Plasma Annealing

We annealed BiDyGa:IG samples at pressures of 2, 3 and 4 Torr with varying rf powers. It can be seen by considering the XRD patterns in Fig. 5.1.2 that the samples β-500, β-800-NG, γ-500, and γ-600 were not crystallized. It can be noticed from Table 5.1.1 that the sample temperature of all these samples did not exceed 500 °C during plasma exposure. The temperature of all other samples, which are crystallized, exceeded 515 °C. Therefore, from our results, it appears that temperature is the primary factor that controls the crystallization process. We showed that during plasma annealing the minimum temperature required to achieve crystallization of BiDyGa:IG films lies in the range of 500°C-515 °C.

In Fig. 4.1.2, we showed that the temperature varies as a function of rf power and pressure during plasma annealing. Hence, the temperature can be controlled by varying the power and pressure. However, the other factor that affected temperature was the presence or absence of conductive films placed behind the sample. Fig. 5.1.2 (b) shows the XRD results of BiDyGa:IG samples, both with and without gold foil in thermal contact with the back-side. The sample β-800 (with back-side gold foil) and β-800-NG (without back-side gold foil) were annealed under identical plasma power and pressure

conditions (800 Watts and 3 Torr). It can be seen that under identical plasma conditions, the sample β-800 has crystallized, while sample β-800-NG remained amorphous. The failure of β-800-NG to crystallize appears to be related to the low sample temperature, which remained below 515 °C. The additional heating associated with the backside gold foil increased the temperature of sample β-800 to above the minimum crystallization temperature within the plasma.

To check our reasoning, we annealed another sample with gold behind the sample (β-500)for pressure and rf power setting where the temperature did not exceed 515 °C. By considering the relevant XRD patterns in Fig. 5.1.2 (b), it can be seen that sample β-500 has not crystallized. This confirms that the crystallization of the BiDyGa:IG samples require a minimum level of thermal energy during the annealing process in the plasma.

5.2.2 Comparison of plasma annealing with other techniques

In order to compare the effectiveness of plasma annealing with other conventional techniques such as RTA and furnance annealing, we performed RTA and furnance annealing on BiDyGa:IG samples at a temperature of 570 °C. The XRD patterns in Fig. 5.1.2 (d) show that the films annealed at 570 °C with furnance and RTA are still amorphous. The plasma-annealed samples, on the other hand, show that the BiDyGa:IG films crystallize at temperatures between 515 and 570 °C. This shows that plasma has the tendency to crystallize the BiDyGa:IG films at lower temperatures in comparison to the temperatures required for RTA and furnance annealings. The minimum temperature at which we could crystallize the BiDyGa:IG films using conventional annealing was

630 °C for furnance and 640 °C for RTA (see Table 5.1.1&Fig. 5.1.2 (d)).

From these experiments, it appears that the crystallization via plasma-treatment is primarily thermal. However, the films do crystallize at relatively lower temperatures in comparison to RTA and furnance. It is possible that there is still some error in the sample temperature when measured in the plasma, which might result in the actual sample temperature in the plasma being higher than the measured value. However, significant effort was taken to calibrate the thermal imager and to ensure that no obvious sources of error were affecting the measured temperature. Given this we believe that the thermal imager gives an accurate temperature for samples in the plasma. Thus, the lower annealing temperature that we observed in the plasma suggest that there are some other processes occurring in plasma that act to catalyse the crystallization process.

5.2.3 Effects on magneto-optical properties

Faraday rotation measurements presented in Fig. 5.1.4 (b) and (e) show that the amorphous samples β-500, γ-500, and γ-600 did not exhibit any Faraday rotation. Samples showed varying degrees of Faraday rotation once the garnet phase for the BiDyGa:IG samples was reached. We have observed that the magnitude of Faraday rotation of plasma-annealed samples is significantly larger near the edges of the sample in comparison to the centre of the sample (see Fig. 5.1.3 (a)). This behavior is somewhat expected as the sample temperature was also shown to vary in a similar manner for the plasma-treated samples (see Fig. 4.1.2 in Chapter 4) and we would expect lower degrees of crystallization towards the centre of the sample. We have also observed a peak shift in Faraday rotation with position on the plasma annealed sample in Fig. 5.1.3 and are likely due to

difference in the plasma exposure on different sections of the sample. Shifts in peak position were also seen from changes in plasma conditions as shown in Fig. 5.1.6.

Given the variation with position on a single sample, which was thought to be related to temperature variations, we expected higher annealing temperatures to lead to higher Faraday rotation. Interestingly, as evident from Fig. 5.1.5, we do not see any correlation of Faraday rotation with sample temperature during plasma annealing. This issue is considered to be beyond the scope of this current thesis, and will be the subject of future proposed work.

The results presented in Fig. 5.1.6 (a) show that the furnance annealing produced the largest Faraday rotation of 6°/μm, as compared to both plasma and RTA annealed samples. An explanation for this is provided by the TEM images in Fig. 5.1.8 where the furnance-annealed sample was shown to be fully crystallized across the film thickness as compared to the plasma and RTA annealed samples, which appeared to show crystallization variations across the film thickness. Future efforts to optimize plasma annealing should attempt to ensure that the crystallization occurs across the full film thickness.

5.2.4 Effects on the surface

We noticed in the Section 5.1.2 that the plasma treated samples showed significant changes around the edges in comparison to the centre of the plasma treated samples. Therefore, AFM images were taken from different locations on the samples to investigate the surface morphological changes. It is clear from the AFM measurements

in Fig. 5.1.7 that plasma annealed samples are rougher near the edges in comparison to the centre of the samples. Fig. 5.1.7 (a) indicates the presence of surface lumps near the edges of the plasma annealed samples. The TEM images (Fig. 5.1.9) suggests that these lumps are associated with delamination of the film possibly due to rapid thermal stresses developed during the annealing process. The middle of the plasma-annealed sample is significantly smooth as compared to the edges without any evidence of hillock formation or delamination on the sample.

The RTA and oven annealed samples have produced relatively smoother surface as compared to the edges of the plasma annealed samples. However, the values of surface roughness values in the centre of the plasma-annealed samples are significantly lower when compared to RTA and furnance annealed samples.

5.2.5 Effects on composition

EPMA and XPS were performed to investigate if any compositional changes were caused by plasma, RTA and furnance annealing. Since, both temperature and Faraday rotation varies based on the position on the surface of plasma-annealed samples, different sections of these samples were also examined.

The EPMA results in Table 5.1.2 show no significant changes in material composition of all the annealed samples in comparison to as-deposited BiDyGa:IG sample. XPS results show a decrease in bismuth and dysprosium concentration, and increase in iron concentration after annealing via plasma, RTA and furnance. The plasma-annealed sample, however, showed no significant differences in the measured atomic percentages of all the elements when compared to RTA & furnance annealed

samples. Therefore, the lower crystallization temperature achieved by plasma does not appear to be related to any plasma-induced change in the composition of material.

5.3 Summary

There was a clear dividing line between samples that were crystallized during plasma annealing and those that remained amorphous. Samples exposed to the plasma with a sample temperature at or below 500 °C were amorphous, whereas samples annealed at temperatures of 515°C or above showed crystallization of the garnet phase. These results suggest that a significant fraction of the crystallization seen in the garnet samples was related to thermal effects. It was also shown that placing gold in thermal contact with the sample increases the effectiveness of crystallization due to an increase in the sample temperature.

The Faraday rotation of the plasma-annealed samples was found to vary across the sample, with maximum at the edges and minimum in the middle. TEM and AFM results confirmed that plasma annealed samples are significantly rougher on the edges compared to the centre, but that the majority of this was caused by delamination of the film near the edges. The centre section of the plasma annealed sample showed no delamination and surface is significantly smoother. EPMA and XPS results showed no significant variations in composition of the plasma-annealed sample in comparison to RTA and furnance annealed samples.

It was found that the plasma annealing is capable of crystallizing the BiDyGa:IG garnet films at a temperature of approximately 100 °C lower than conventional RTA and furnance annealing techniques. Thus, despite the fact that the majority of the annealing

occurring in the plasma appears to be related to thermal processes occurring within the chamber, which heat the sample, there are other process that catalyses crystallization of the garnet phase at relatively low temperatures. Plasma annealing therefore offers the potential to decrease the thermal budget required for the development of crystalline garnet phases in the production of magneto-optical components. However, issues related to optimization of Faraday rotation, uneven heating and film delamination need to be addressed in the plasma annealing process.

6

Conclusions and further work

The aim of this project was to reduce the thermal budget required for the crystallization of $Bi_2Dy_1Fe_4Ga_1O_{12}$ (BiDyGa:IG) thin films using plasma annealing. Lower thermal processing is required to make these materials compatible with the silicon industry, since the crystallization of a typical iron garnet material of composition BiDyGa:IG on a Si/SOI substrates requires an annealing temperature of 620 °C to 650 °C [19] [20] using more traditional annealing process. Integration requires processing temperatures below 577 °C, the eutectic point of aluminum and silicon, since temperatures above 577 °C would destroy the integrity of the chip if aluminum metallization is used. Hence, if iron garnet thin films are to be incorporated with standard CMOS technology, crystallization at lower temperatures (below 577 °C) is necessary.

To achieve this goal, plasma annealing, which has already been shown to crystallize oxide films such as TiO_2 and Indium-Titanium oxide (ITO) at temperatures much lower than conventional annealing [23, 24, 26], was investigated. The activation process for this low temperature crystallization was attributed to the rf electromagnetic fields in the plasma by Ohsaki *et al.* [22-26]. Ohsaki also theorized that the presence of a conductor in thermal contact with the backside of the sample increased the effectiveness of the

crystallization via an increase in the electric field strength around the sample [25].

In this thesis, the plasma parameter space and garnet films were characterized to develop an understanding of the fundamental processes occurring in the plasma that might potentially affect the crystallization process. Towards this end, the hypotheses presented by Ohsaki *et al*. were experimentally tested to determine their validity and and to confirm their experimental results. This chapter will summarize the results obtained from this project and will compare the results with previously published work. Finally, a list of further work that is required to make the plasma annealing process more effective will be presented.

6.1 Summary

Characterization of plasma parameter space

The purpose of Chapter 4 was to investigate the sample temperature and plasma species, and their variations with respect to process conditions of rf power and chamber pressure. In order to characterize the plasma, we used thermal imaging, optical emission spectroscopy and a Langmuir probe. This work demonstrated the presence of atomic oxygen and singly ionised atomic oxygen across the experimental range of conditions investigated. Electron energy, electron density, and diffusion were explained in conjunction with the variation in the emission characteristics of O^+ and O in the plasma. The temperatures measured for QC845 coated quartz at similar pressure and power conditions to Ohsaki *et al*.[22] in a similar chamber were significantly different. The temperatures measured by Ohsaki never increased above 250 °C even at rf powers of 1000 Watts. However, we measured the temperature of the samples to always be higher

than 350 °C even at an rf power of 500 Watts. We observed the maximum temperature of 570 °C at an rf power of 800 Watts. Ohsaki used a radiation thermometer that could measure a maximum temperature of 500 °C only. In addition, it is possible that he did not take into account of the emissivity of the samples, which would lead to the reduced temperature values. We, on the other hand, took great care to characterize the emissivity of the samples through the ZnSe window, and thus ensured that the temperature measurements of the samples were accurate.

The presence of a conductor behind and in contact with the sample was shown to increase the sample temperature, decrease the O^+ emission line magnitude, and improve the sample temperature spatial uniformity as compared to the samples without a back-side conductor. The decrease in the O^+ magnitude around the sample in the presence of a conductor does not support Ohsaki's hypothesis, which proposed that the electric field increases when a conductor is placed behind the sample. If the electric fields were increased, one would expect more positive ions in close proximity to the sample with a backside conductor (see Section 4.5). However, from our experiments in Chapter 4, we observed that the O^+ magnitude decreases around the sample with a backside conductor (see Fig. 4.2.6). Therefore, the effects of the electric field around the sample and on the crystallization process appear uncertain.

Characterization of $Bi_2Dy_1Fe_4Ga_1O_{12}$ thin films

In Chapter 5, the $Bi_2Dy_1Fe_4Ga_1O_{12}$ garnet thin films were annealed via plasma, RTA and furnance annealing. The plasma annealing was shown to crystallize the garnet samples at temperatures as low as 515 °C, compared to temperatures of 620 °C and 650 °C required to crystallize garnets of similar composition via rapid thermal annealing [19] and conventional furnance annealing [20], respectively. This work has shown that there is a clear dividing line between samples that crystallized during plasma exposure and those that remained amorphous. These results suggest that a significant fraction of the crystallization that is seen in the plasma-annealed garnet samples was related to thermal effects. It was also shown that placing gold behind the sample increases the effectiveness of crystallization due to an increase in the sample temperature inside the plasma. Despite the fact that the majority of the annealing occurring in the plasma appears to be thermal, plasma annealing has been shown to crystallize BiDyGa:IG garnet films at a temperature of approximately 100 °C lower than conventional RTA and furnance annealing techniques. This suggests the presence of additional processes during plasma annealing that enhances the crystallization of garnet phase at relatively low temperatures.

The plasma-annealed samples were found to be rougher around the edges of the sample compared to the centre. The increased roughness on the edges was attributed to the delamination of the garnet films. The EPMA and XPS results showed that no significant variations in composition of the garnet films occurred during the plasma annealing process.

6.2 Conclusions

Thin-film amorphous $Bi_2Dy_1Fe_4Ga_1O_{12}$ (BiDyGa:IG) films were successfully crystallized using plasma annealing at temperatures more than 100 °C below those required for film crystallization by conventional furnance annealing and rapid thermal annealing (RTA) techniques. This substantially reduces the thermal budget required for the crystallization of the garnet phase. The work conducted in this thesis has led to the conclusions that can be summarized by the following points:

- The optical emission spectra of the oxygen plasma in the 200-800nm wavelength range yields a spectrum that appears to almost exclusively consist of singly ionised oxygen (O^+) and atomic oxygen (O) lines.
- Langmuir probe results show that the electron temperatures lie in the range of 11 to 43 eV, which supports the generation of both O^+ and O across the experimental conditions investigated.
- The presence of a gold foil in thermal contact with the backside of the sample decreased the O^+ emission line magnitude, while the O emission line magnitude was not significantly affected. These results contradict the hypothesis of Ohsaki *et al.* [25] that electric field effects around the sample (with backside conductor) are responsible for the crystallization of the films.
- The use of thermal imaging showed that the temperature of the test sample (without backside gold) varied between 350-500 °C. This was significantly higher than the temperature reported by Ohsaki *et al.* [22], where the maximum observed temperature was 250 °C under similar experimental conditions.

- The presence of a gold foil in thermal contact with the backside of the sample increased the temperature of the test sample to a range of 390-570 °C, and improved the spatial uniformity of the temperature across the sample.

- The temperature attained by the quartz sample in the plasma was shown to be a linear function of the sum of the logs of the magnitudes of the emission lines of both O^+ and O i.e {ln (O) + ln(O^+), and hence may be related to the free energy of reaction of the O and O^+ ions in the plasma.

- The crystallization of the garnet films was achieved at a temperature as low as 515 °C in comparison to a crystallization temperature for furnance annealing of 630 °C and for RTA of 640 °C.

- The Faraday rotation of the plasma-annealed sample was shown to be non-uniform across the surface with a maximum at the edges of the sample and a minimum at the middle of the sample, which follows the temperature variation across the sample.

- Plasma annealed samples did not show any significant changes in the composition as compared to amorphous, RTA and furnance annealed samples.

- Plasma annealed samples showed increased surface roughness at the edges (RMS roughness: 43 nm rms) as compared to the surface roughness near the centre (RMS roughness: 8 nm rms). The increased surface roughness on the edges was attributed to the delamination of the garnet film from the substrates.

In conclusion, we have broadened the available knowledge on the plasma annealing method, and demonstrated that complex garnet films like $Bi_2Dy_1Fe_4Ga_1O_{12}$ can also be crystallized at relatively low temperatures by plasma treatment in comparison to RTA and furnance annealing. The results suggest that a significant fraction of the annealing effect of the plasma is related to thermal effects [22]. However this effect does not completely explain the process as crystallization, which occurs at temperatures below those required using other annealing techniques. The temperature reached during plasma annealing in Chapter 4 was found to be significantly higher than the temperature values for the similar process conditions reported by Ohsaki *et al.* [23, 24, 26].

Ohsaki suggested that the reason for the increase in the effectiveness of crystallization was attributed to the electric field intensity. They presented the hypothesis that the conductor acts like a dipole antenna, which increases the electric filed intensity around the sample [25]. However, from the observed increase in the overall sample temperature and decrease in the magnitude of positive ions (O^+) around the sample described in Chapter 4, the effects of electric fields on the crystallization process appears improbable.

6.3 Further work

Plasma annealing offers the potential to decrease the thermal budget related to the development of crystalline garnet phases in the production of electro-optical components. However, there are some significant hurdles that need to be overcome, the understanding of the annealing process is in its infancy. Future work that needs to be undertaken includes answering the following questions.

- What is the mechanism responsible for reducing the crystallization temperature? In this thesis, plasma annealing has here been shown to crystallize the garnet films at significantly lower temperatures in comparison to both RTA and furnance annealing. However, the mechanism for the reduction in crystallization temperature is not clear. The mechanism proposed by Ohsaki relating the electric fields to the crystallization process appears improbable. From our experiments, it appears that the crystallization process is primarily thermal in nature.

- What is the mechanism of sample heating? The sample temperature may be affected by O^+ ions, electrons or radiative heat transfer, or due to some combination of these heating mechanisms. From the results in Chapter 4, it appears that the sample temperature is affected via the reactions happening within the plasma. However, the effects of electrons and O^+ ions on the sample temperature are still not clear. Therefore, additional work should be undertaken to investigate the effects of the electrons and ions on the temperature of the samples. This could be done by finding the electron and ion temperature and their densities within the plasma.

- Controlling the variation in sample properties across the sample. Chapter 5 showed that the Faraday rotation and other properties on the plasma-annealed samples vary as a function of distance from the edge of the sample. Finding ways to produce spatially uniform annealing is critical to the general application of the technique. The changes around the edges of the sample could be related to increased electron or ion collisions. This could also be investigated

once the electron/ion densities and temperatures are known within the plasma under suitable experimental conditions.

- How to minimize delamination from the quartz substrate? During plasma annealing, an increase in the surface roughness near the edges of the samples was observed. Subsequent TEM imaging showed that this roughness was primarily related to delamination of the garnet film. More work needs to be undertaken in order to improve the quality of the plasma-treated films in terms of surface roughness and film delamination.

Appendix I

A. Presentations arising from this thesis:

- **R. Sharda**, R.D. Jeffery, M, Martyniuk, R.C. Woodward, J.M. Dell, L. Faraone, "Low temperature crystallization of bismuth substituted iron garnet films using plasma annealing". Presented at ISFM, 17—20 December 2012 at UWA, Perth. *(Won the best poster award.)*

- **R. Sharda**, R.D. Jeffery, M, Martyniuk, R.C. Woodward, J.M. Dell, L. Faraone, "Plasma annealing as an effective method for the crystallization of bismuth iron garnet films". Presented at COMMAD, 12—14 December 2012 at RMIT, Melbourne.

- **R. Sharda**, M. Martyniuk, R.D. Jeffery, R.C. Woodward, J.M. Dell and L. Faraone, "Effects of plasma annealing on rare earth substituted iron garnet film". Presented at APMC 10 / ICONN 2012 / ACMM 22, 6-9 February 2012 at Perth Convention and Exhibition Centre (PCC), Perth.

A. Sample temperature (with and without Au) in N_2

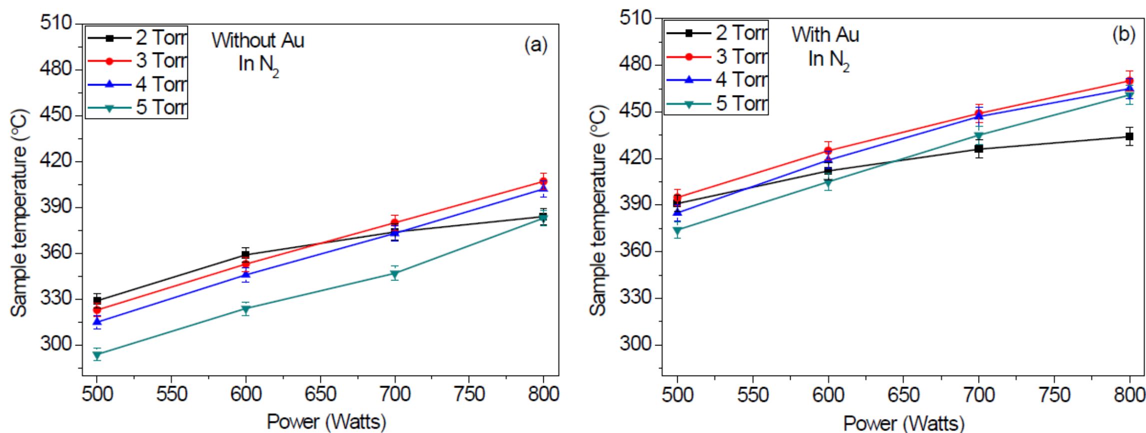

Fig. A: Temperature variations of QC845 coated quartz sample in N_2 as a function of rf power (a) Without Au foil (b) With Au foil, error bars representing the relative standard deviation of 1.35 % for separate measurements.

Fig. A presents the results of sample temperature in nitrogen plasma as a function of rf power. Fig. A (a) shows the temperature of QC845 coated quartz sample without Au in thermal contact with the sample. Fig. A (b) shows the temperature of QC845 coated quartz sample with Au in thermal contact with the sample. It can be seen from Fig A (a) that the sample temperature lies in range of about 280-410 °C, while Fig. A (b) shows the sample temperature in the range of 370-480°C. From a comparison of temperature in Fig. A (a) and Fig. A (b), it can be seen that the sample temperature has increased due to the introduction of backside gold foil. The reason to present these observations is to show that the sample temperature achieved in the N_2 plasma is significantly below the sample temperatures achieved in in oxygen plasma (see Fig. 4.1.1 & 4.1.2), and that the sample temperature in N_2 plasma does not increase above 515 °C even in the presence of gold foil behind the sample.

B: Sample temperature with Au foil at the backside (in O_2):

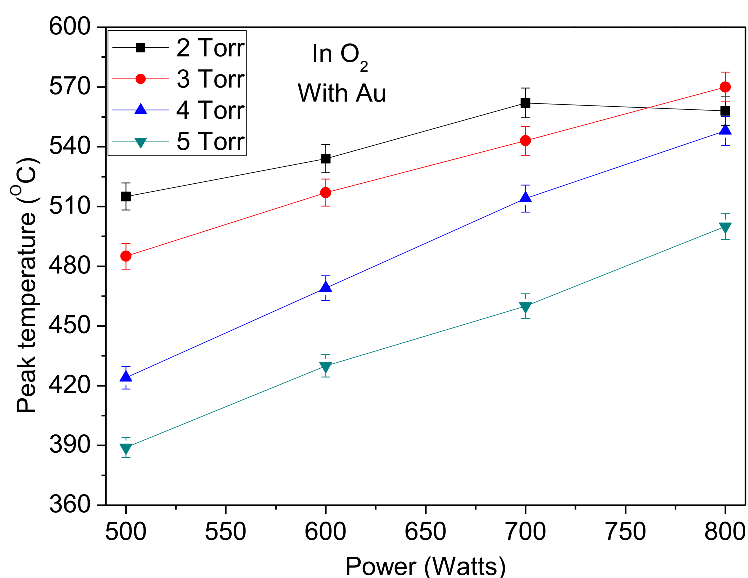

Fig. B: Temperature variations of QC845 coated quartz sample with Au foil test in O_2 as a function of rf power, error bar representing the relative standard deviation of 1.35% for separate measurements.

Fig. B shows the temperature of QC845 coated quartz sample with Au foil at the backside and in contact with the sample (in O_2). It can be seen from the plot that the temperature in the presence of a conductor has increased to the range of 390-570 °C in comparison to the temperatures of 350-500 °C for samples without Au foil behind it. (see Fig. 4.1.2). The difference in the temperature of the sample (with and without Au) is presented in Fig. 4.1.4.

C: Optical emission spectra of nitrogen plasma:

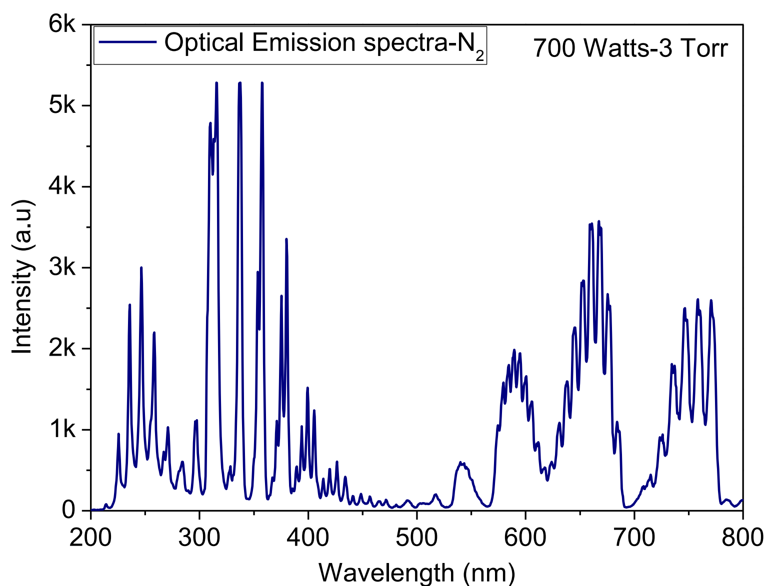

Fig. C: Optical emission spectra of nitrogen as a function of wavelength at power of 700 Watts and pressure of 3 Torr.

Fig. C shows the optical emission spectra for nitrogen plasma at an rf power of 700 Watts and pressure of 3 Torr. The spectrum of nitrogen is much more complex in comparison to the spectrum of oxygen (see Fig. 4.2.1). Because of the fact that the sample temperatures achieved in nitrogen plasma were not found to exceed 515 °C the optical emission spectrum of nitrogen was not studied in detail.

D: Plasma, RTA and furnance annealing results (In Oxygen):

Table D: BiDyGa:IG sample annealing with plasma, rapid thermal and furnance

No.	Sample	Process conditions				State	Faraday rotation (degree/μm)
Plasma annealed samples (all 15 minutes)							
		Power (Watts)	Pressure (Torr)	Temp. (°C)			
1.	α-650	500 W	2 T	515		Crystallized	3.1
2.	α-650-NG	600 W	2 T	534		Crystallized	1.7
3.	β-760	760 W	3.2 T	552		Crystallized	3.3
RTA annealed samples (both 15 minutes)							
		Ramp rate (cps.)	Flow rate (sccm)	Ambient	Temp. (°C)		
4.	R-3	30	200	O_2	570	Amorphous	0.0
5.	R-4	30	100	O_2	650	Crystallized	1.5
Furnance annealed samples (all 90 minutes)							
		Ambient	Temp.(°C)				
6.	O-4	O_2	620			Amorphous	0.0
7.	O-5	O_2	640			Amorphous	4.2
8.	O-6	O_2	670			Crystallized	6.0

Table D provides a summary of results for the additional investigated garnet samples. It shows the process conditions, the material state (crystalline/amorphous), and the achieved Faraday rotation for plasma, RTA and furnance annealed BiDyGa:IG films.

Bibliography

[1] F. J. Kahn, P. S. Pershan, and J. P. Remeika, "Ultraviolet Magneto-Optical Properties of Single-Crystal Orthoferrites, Garnets, and Other Ferric Oxide Compounds," *Physical Review,* vol. 186, pp. 891-918, 10/15/ 1969.

[2] K. Nakagawa, S. Kurashina, and A. Itoh, "Uniaxial anisotropy of double-layered garnet films and magneto-optical recording characteristics," *Journal of Applied Physics,* vol. 75, pp. 7096-7098, 1994.

[3] K. Shaoying, Y. Shizhuo, V. Adyam, Q. Li, and Z. Yong, "$Bi_3Fe_4Ga_1O_{12}$ Garnet Properties and Its Application to Ultrafast Switching in the Visible Spectrum," *Magnetics, IEEE Transactions on,* vol. 43, pp. 3656-3660, 2007.

[4] M. Ko and E. Garmire, "Current sensing using bismuth rare-earth iron garnet films," *Appl. Opt.,* vol. 34, pp. 1692-1696, 04/01 1995.

[5] N. Itoh, H. Minemoto, D. Ishiko, and S. Ishizuka, "Small optical magnetic-field sensor that uses rare-Earth iron garnet films based on the faraday effect," *Appl Opt,* vol. 38, pp. 2047-52, Apr 1 1999.

[6] S. Mito, J. Kim, K. H. Chung, K. Yamada, T. Kato, H. Takagi*, et al.*, "Magnetic property of polycrystalline magnetic garnet for voltage driven type magneto-optic spatial light phase modulator," *Journal of Applied Physics,* vol. 107, pp. 09A948-09A948-3, 2010.

[7] J.-H. Park, H. Takagi, J.-K. Cho, K. Nishimura, H. Uchida, and M. Inoue, "Magnetooptic spatial light modulator with one-step pattern growth on ion-milled substrates by liquid-phase epitaxy," *Magnetics, IEEE Transactions on,* vol. 40, pp. 3045-3047, 2004.

[8] S. Kahl, "Bismuth iron garnet films for magneto-optical photonic crystals," *Royal Institute of Technology,* 2004.

[9] J. Fujita, M. Levy, R. M. Osgood, L. Wilkens, and Do¨tsch, "H.Waveguide optical isolator based on Mach–Zehnder interferometer.," *Appl. Phys. Lett. 76,* pp. 2158–2160 2000.

[10] T. Shintaku, "Integrated optical isolator based on efficient nonreciprocal radiationmode conversion.," *Appl. Phys. Lett. 73,* pp. 1946–1948, 1998.

[11] C. A. Desmond-Colinge and U. Go¨sele, "Wafer-bonding and thinning technologies," *MRS Bull. 23,* pp. 30–34, 1998.

[12] B. Stadler, K. Vaccaro, P. Yip, J. Lorenzo, Y.-Q. Li, and M. Cherif, "Integration of magneto-optical garnet films by metal-organic chemical vapor deposition," *Magnetics, IEEE Transactions on,* vol. 38, pp. 1564-1567, 2002.

[13] L. J. C. Rivera, S. Pandit, S. Pieski, R. Cobian, M. Cherif, and B. J. Stadler, "Integrated isolators for opto-electro-mechanical systems and devices," in *Symposium on Integrated Optics*, 2001, pp. 29-42.

[14] B. J. Stadler and A. Gopinath, "Magneto-optical garnet films made by reactive sputtering," *Magnetics, IEEE Transactions on,* vol. 36, pp. 3957-3961, 2000.

[15] L. Cruz-Rivera, "Integrated Magneto-Optic Garnet Isolators via Reactive Sputtering," *Technical Paper Proceedings,* p. 23, 2001.

[16] B. Stadler, K. Vaccaro, P. Yip, J. Lorenzo, L. Yi-Qun, and M. Cherif, "Integration of magneto-optical garnet films by metal-organic chemical vapor deposition," *Magnetics, IEEE Transactions on,* vol. 38, pp. 1564-1567, 2002.

[17] S.-Y. Sung, X. Qi, and B. J. H. Stadler, "Integrating yttrium iron garnet onto nongarnet substrates with faster deposition rates and high reliability," *Applied Physics Letters,* vol. 87, pp. 121111-3, 09/19/ 2005.

[18] N. Izhaky, M. T. Morse, S. Koehl, O. Cohen, D. Rubin, A. Barkai*, et al.*, "Development of CMOS-compatible integrated silicon photonics devices," *Selected Topics in Quantum Electronics, IEEE Journal of,* vol. 12, pp. 1688-1698, 2006.

[19] M. Vasiliev, M. Nur-E-Alam, K. Alameh, P. Premchander, Y. T. Lee, V. A. Kotov*, et al.*, "Annealing behaviour and crystal structure of RF-sputtered Bi-substituted dysprosium iron-garnet films having excess co-sputtered Bi-oxide content," *Journal of Physics D: Applied Physics* vol. 44, 2011.

[20] T. Suzuki, "Magnetic and magneto-optic properties of rapid thermally crystallized garnet films (invited)," *Journal of Applied Physics,* vol. 69, pp. 4756-4760, 1991.

[21] L. Armelao, M. Pascolini, G. Bottaro, G. Bruno, M. Giangregorio, M. Losurdo*, et al.*, "Microstructural and Optical Properties Modifications Induced by Plasma and Annealing Treatments of Lanthanum Oxide Sol− Gel Thin Films," *The Journal of Physical Chemistry C,* vol. 113, pp. 2911-2918, 2009.

[22] H. Ohsaki, R. Andou, A. Kinbara, and T. Watanabe, "Crystallization of ITO and TiO2 by RF plasma treatment," *Vacuum,* vol. 87, pp. 145-149, 1// 2013.

[23] H. Ohsaki, Y. Shibayama, A. Nakajim, A. Kinbara, and T. Watanabe, "Plasma treatment for crystallization of amorphous thin films," *Thin Solid Films,* vol. 502, pp. 63-66, 4/28/ 2006.

[24] H. Ohsaki, Y. Shibayama, M. Suzuki, A. Kinbara, H. Yashiro, and T. Watanabe, "Room temperature crystallization by RF plasma," *Thin Solid Films,* vol. 516, pp. 4490-4494, 5/30/ 2008.

[25] H. Ohsaki, Y. Shibayama, N. Yoshida, T. Watanabe, and S. Kanemaru, "Room-temperature crystallization of amorphous films by RF plasma treatment," *Thin Solid Films,* vol. 517, pp. 3092-3095, 3/31/ 2009.

[26] H. Ohsaki, M. Suzuki, Y. Shibayama, A. Kinbara, and T. Watanabe, "Room temperature crystallization of indium tin oxide films on glass and polyethylene terephthalate substrates using rf plasma," *Journal of Vacuum Science & Technology A: Vacuum, Surfaces, and Films,* vol. 25, pp. 1052-1055, 2007.

[27] J. Ziegler, J. Biersack, and U. Littmark, "The stopping and range of ions in solids," *Pergamon Press, New York,* vol. 4, pp. 40-47, 1985.

[28] Y. Hu, X. Diao, C. Wang, W. Hao, and T. Wang, "Effects of heat treatment on properties of ITO films prepared by rf magnetron sputtering," *Vacuum,* vol. 75, pp. 183-188, 7/12/ 2004.

[29] J. Lee, D. Lim, K. Yang, and W. Choi, "Influence of different plasma treatments on electrical and optical properties on sputtered AZO and ITO films," *Journal of Crystal Growth,* vol. 326, pp. 50-57, 2011.

[30] K. Seomoon, J. Kim, S. Ju, P. Jang, and K.-H. Kim, "Inductively coupled plasma post-treatment of Al-doped ZnO thin films," *Current Applied Physics,* vol. 11, pp. S30-S32, 2011.

[31] E. K. Kim, Y. S. Park, and J. Lee, "Characteristics of ITO films with Oxygen Plasma Treatment for Thin Film Solar Cell Applications," *isfm conference,* 2012.

[32] R. D. Jeffery, "Method of Crystallising Thin Films," *International Patent Application PCT/Au2012/001053.,* 2012.

[33] J. Camacho, M. Santos, L. Díaz, L. Juan, and J. Poyato, "Spectroscopy study of air plasma induced by IR CO2 laser pulses," *Applied Physics A,* 2009.

[34] M. S. Barnes, J. C. Forster, and J. H. Keller, "Electron energy distribution function measurements in a planar inductive oxygen radio frequency glow discharge," *Applied Physics Letters,* vol. 62, pp. 2622-2624, 05/24/ 1993.

[35] J. W. Coburn and H. F. Winters, "Ion- and electron-assisted gas-surface chemistry---An important effect in plasma etching," *Journal of Applied Physics,* vol. 50, pp. 3189-3196, 05/00/ 1979.

[36] M. A. Lieberman and A.J. Lichtenberg, "Principle of Plasma Discharges and Materials Processing," *2nd editionWiley, New York.,* 2004.

[37] H.-C. Lee, M.-H. Lee, and C.-W. Chung, "Effects of rf-bias power on plasma parameters in a low gas pressure inductively coupled plasma," *Applied Physics Letters,* vol. 96, pp. 071501-3, 02/15/ 2010.

[38] G. Robersona, M. Robertoa, J. Verboncoeurb, and P. Verdonck, "Global Model Simulations of Low-Pressure Oxygen Discharges," *Brazilian Journal of Physics,* vol. 37, p. 8, 2007.

[39] M. Shibata, N. Nakano, and T. Makabe, "Effect of O2(a1Δg) on plasma structures in oxygen radio frequency discharges," *Journal of Applied Physics,* vol. 80, pp. 6142-6147, 12/01/ 1996.

[40] D. C. Seo and T. Hun, "Observation of the transition of operating regions in a low-pressure inductively coupled oxygen plasma by Langmuir probe measurement and optical emission spectroscopy," *J. Phys. D: Appl. Phys,* vol. 34, p. 5, 2001.

[41] J. J. Camacho, L. Díaz, M. Santos, D. Reyman, and J. M. L. Poyato, "Optical emission spectroscopy of oxygen plasma induced by IR CO2 pulsed laser," *J. Appl. Phys,* vol. 41, p. 11, 2008.

[42] J. H. Keller, "Inductive plasmas for plasma processing," *Plasma Sources Sci. Technol.,* vol. 5, 1996.

[43] S. Yun and G. R. Tynan, "Spatial profiles of neutral, ion, and etch uniformity in a large-area high-density plasma reactor," *Journal of Applied Physics,* vol. 89, pp. 911-914, 01/15/ 2001.

[44] I. Langmuir, "The Interaction of Electron and Positive Ion Space Charges in Cathode Sheaths," *Physical Review,* vol. 33, pp. 954-989, 06/01/ 1929.

[45] M. A. Lieberman, "Plasma Science, IEEE Transactions," *IEEE Trans. Plasma Sci,* vol. 17, p. 4, 1989.

[46] W. B. Pennebaker, "Influence of scattering and ionisation on RF impedence in glow discharge sheaths," *IBM J. Res. Develop. ,* vol. 23, p. 9, 1929.

[47] A. L. Ward, "Calculations of Cathode-Fall Characteristics," *Journal of Applied Physics,* vol. 33, pp. 2789-2794, 09/00/ 1962.

[48] T. J. Sommerer and M. J. Kushner, "Numerical investigation of the kinetics and chemistry of rf glow discharge plasmas sustained in He, N2, 02, e/N2/02, He/CF4/02, and SiH4/NH3 using a Monte Carlo-fluid hybrid model," *Journal of Applied Physics,* vol. 71, pp. 1654-1673, 02/15/ 1992.

[49] V. A. Godyak and A. S. Khanneh, "Ion Bombardment Secondaty Electron Maintenance of Steady RF Discharge," *Plasma Science, IEEE Transactions on,* vol. 14, pp. 112-123, 1986.

[50] W. N. G. Hitchon, "Plasma processes for semiconductor fabrication," *Cambridge University Press,* p. 20, 2005.

[51] V. A. Godyak, R. B. Piejak, and B. M. Alexandrovich, "Probe diagnostics of non-Maxwellian plasmas," *Journal of Applied Physics,* vol. 73, pp. 3657-3663, 04/15/ 1993.

[52] H.-C. Lee, J.-Y. Bang, and C.-W. Chung, "Effects of RF bias power on electron energy distribution function and plasma uniformity in inductively coupled argon plasma," *Thin Solid Films,* vol. 519, pp. 7009-7013, 8/1/ 2011.

[53] H. Singh and D. B. Graves, "Measurements of the electron energy distribution function in molecular gases in a shielded inductively coupled plasma," *Journal of Applied Physics,* vol. 88, pp. 3889-3898, 10/01/ 2000.

[54] M. A. Gilleo and S. Geller, "Magnetic and Crystallographic Properties of Substituted Yttrium-Iron Garnet, 3Y_{2}O_{3}·xM_{2}O_{3}·(5-x)Fe_{2}O_{3}," *Physical Review,* vol. 110, pp. 73-78, 04/01/ 1958.

[55] H. Dötsch, N. Bahlmann, O. Zhuromskyy, M. Hammer, L. Wilkens, R. Gerhardt*, et al.*, "Applications of magneto-optical waveguides in integrated optics: review," *J. Opt. Soc. Am. B,* vol. 22, pp. 240-253, 01/01 2005.

[56] A. M. Clogston, "Interaction of Magnetic Crystals with Radiation in the Range 10^4-10^5 cm^{-1}," *Journal of Applied Physics,* vol. 31, pp. S198-S205, 1960.

[57] P. Hansen, K. Witter, and W. Tolksdorf, "Magnetic and magneto-optic properties of bismuth- and aluminum-substituted iron garnet films," *Journal of Applied Physics,* vol. 55, pp. 1052-1061, 02/15/ 1984.

[58] M. Guillot, Y. Braik, H. Le Gall, M. Artinian, and J. M. Desvignes, "Faraday rotation of bismuth substituted dysprosium iron garnets," *Magnetics, IEEE Transactions on,* vol. 29, pp. 3396-3398, 1993.

[59] G. Scott and D. E. Lacklison, "Magnetooptic properties and applications of bismuth substituted iron garnets," *Magnetics, IEEE Transactions on,* vol. 12, pp. 292-311, 1976.

[60] P. Q. Limited, "Material information. Availaible from: <http://www.plasmaquest.co.uk/materials.php>," 31 July 2013.

[61] E. Leal-Quirós, "Basic plasma diagnostics: probes and analyzers," *JournalNewMexicoPresentations,* nd.

[62] F. F. Chen, "Langmuir Probe Diagnostics," *IEEE-ICOPS meeting,* 2003.

[63] S. Kahl, "Bismuth iron garnet films for magneto-optical photonic crystals," KTH, 2004.

[64] G. A. Hebner and A. M. Paterson, "Ion temperature and velocity in a 300 mm diameter capacitively coupled plasma reactor driven at 13, 60 and 162 MHz" *Plasma Sources Science and Technology,* vol. 19, 2010.

[65] W. W. Smeltzer, "Oxidation of Aluminum in the Temperature Range 400°–600°C," *Journal of The Electrochemical Society,* vol. 103, pp. 209-214, 1956.

[66] Y. Zhu, K. Mimura, and M. Isshiki, "Oxidation Mechanism of Copper at 623-1073 K," *Materials Transactions,* vol. 43, pp. 2173-2176, 2002.

[67] C. Lee, D. B. Graves, M. A. Lieberman, and D. W. Hess, "Global Model of Plasma Chemistry in a High Density Oxygen Discharge," *J. Electrochem. Soc,* vol. 141, p. 10, 1994.

[68] J. Rehsinger, *Journal of magnetism & magnetic materials,,* vol. 211, pp. 291-295, 2000.

[69] ICDD, "Calculated from LPF using POWD-12++," *ICDD databse: PDF Card - 04-006-3343,* 1994.